



Eidgenössische Technische Hochschule Zürich
Swiss Federal Institute of Technology Zurich



CRANFIELD UNIVERSITY

Alejandro Valverde López

**BENDING-TWIST SHAPE ADAPTATION BY
COMPLIANT CHIRAL SPAR DESIGN**

SCHOOL OF AEROSPACE, TRANSPORT AND MANUFACTURING

MSc THESIS

CRANFIELD UNIVERSITY

SCHOOL OF AEROSPACE, TRANSPORT AND MANUFACTURING

MSc THESIS

Academic Year 2016-17

Alejandro Valverde López

Bending-twist Shape Adaptation By Compliant Chiral Spar Design

Supervisor: Dr. Simon Prince (Cranfield University)

Prof. Dr. P. Ermanni (ETH Zürich)

August 2017

This thesis is submitted in partial (45%) fulfillment of the requirements for the degree of Master of Science in Aerospace Dynamics

©Cranfield University 2017. All rights reserved. No part of this publication may be reproduced without the written permission of the copyright owner.

Abstract

This thesis presents a novel purely passive mechanism of twist morphing for application on airframe structures, such as wings. During certain flight conditions such as gust encountering, the aircraft may experience critical loads that threaten the structural integrity. To counteract this situation, a rapid modification of the lift distribution to achieve a reduction in the aerodynamic loads is needed. The proposed method aims to control the bending-twist coupling of the wing-box and is based in a variable-stiffness adaptive spar implementation. Through modifications in the effective shear modulus in this adaptive spar, variations in the torsional stiffness of the wing-box are induced. The mechanism intentionally originated elastic instabilities in a structure of chiral elements to induce this sudden reductions in the adaptive spar stiffness. Therefore, snap-buckling instabilities are used to achieve the desired sectional twist of the wing-box. An analytical model of the wing-box is developed to provide information related to the changes in mechanical properties through modifications in shear modulus on the variable stiffness spar. A computational model of the whole assembly is built to provide insight of the buckling phenomena and the nonlinear response in twist of the structure. An extensive analysis of the influence of each of the main parameters in the buckling appearance and evolution, and in final twist response is presented. Numeric results show that snap-buckling instabilities indeed provide an effective way of changing the torsional stiffness of a wing-box and therefore affecting the twist and the lift distribution over the wing. Also, results show that parameters such as the wing-box thickness or the ligament eccentricity provide tailorability capabilities over the onset of triggering buckling at a prescribed level of external loading.

This project was realized within the Laboratory of Composite Materials and Adaptive Structures of the Eidgenössische Technische Hochschule Zürich (Swiss Federal Institute of Technology Zurich), under the supervision of Prof. Dr. P. Ermanni and the advisory of F. Runkel, K. Dominic and U. Fasel.

Acknowledgments

First of all, I would like to thanks Dr. Simon Prince from Cranfield University for offering himself to remotely supervise this thesis.

Secondly, I would like to thank to Prof. Dr. Paolo Ermanni for the opportunity offered to conduct my master thesis at the Laboratory of Composite Materials and Adaptive Structures at ETH Zürich.

Furthermore, I would like to thank my advisor at ETH Zürich, Falk Runkel, for his kindness and continuous help and support. His inestimable aid put my work into the right path so I could feel proud of it.

Special thanks to Theofanis Tsiantas who provided an immeasurable help throughout the whole project. His suggestions and support helped me to gain fundamental understanding of the structures mechanics.

Finally, I would like to give my eternal gratitude to my family, for their full and unconditional support throughout all this years of my education.

Contents

Abstract	i
Acknowledgments	iii
List of figures	ix
List of tables	x
List of symbols	xiv
1 Introduction	1
2 State-of-the-art	3
2.1 Morphing aircraft	3
2.2 Compliant chiral structure	9
2.3 Rationale for the thesis	14
3 Wing-box model	16
3.1 Concept	16
3.2 Analytical model	18
3.3 Computational model	21
3.3.1 Sub-parts and parametrization of the model	22
3.3.2 Computational model mesh characteristics	35
3.3.3 Load definition	36

3.3.4	Boundary condition	37
3.3.5	Post-processing operations	38
3.3.6	Connection between the wing-box skin and the chiral lattice	39
3.3.7	Parametric study method	44
4	Model analysis	46
4.1	Analytical model analysis	46
4.1.1	Bending and twisting coupling results and discussion	48
4.1.2	Parametric study results and discussion	50
4.2	Computational model analysis	50
4.2.1	Mesh	57
4.2.2	Nonlinear problem and automatic stabilization	58
4.2.3	Ribs	62
5	Simulations results	65
5.1	General response characterization	65
5.2	Parametric study on the computational model	69
5.2.1	Wing-box thickness	69
5.2.2	Number of unit cells in the chiral lattice	74
5.2.3	Chiral lattice parameters	77
6	Conclusion and Outlook	91
	Bibliography	93
A	Python code generated	96

List of Figures

1.1	Aircraft encountering a vertical gust	2
2.1	Wright Brothers 1899 kite	4
2.2	Shape morphing wing classification	4
2.3	The X-53 performing a 360° roll to prove AAW technology	5
2.4	Inner structure of the experimental wing build to test the concept of adaptive wing-box	7
2.5	Plate buckling on one of the webs of the wing-box beam	8
2.6	Chiral structure of rotatable nodes and bendable ligaments	9
2.7	Experimental Poisson's ratio ν as a function of axial compressive strain on a chiral honeycomb	10
2.8	Chiral cell elements showing different ligaments curvatures	11
2.9	Compression load test on a basic triangular chiral structure	12
2.10	Investigated configurations for the truss-core of chiral topology	12
2.11	Manufactured prototype of a truss-core airfoil with chiral topology	13
2.12	Chiral sail concept	13
3.1	Working principle for the adaptive beam	17
3.2	Set of chiral ligaments undergoing instabilities at the root of the wing-box	18
3.3	Schematic view of the beam closed section	18
3.4	General assembly configuration for the computational model	21

3.5	Default normals and thickness direction for continuum shell elements in Abaqus	21
3.6	Overview of the chiral lattice part	22
3.7	Division of the lattice structure in cell units	23
3.8	Internal parameters of the chiral lattice structure	24
3.9	Picture of the manufactured chiral lattice nodes	26
3.10	Kinematic coupling constraint	27
3.11	Overview of the elements that are involved in the coupling condition at the lattice nodes .	28
3.12	Overview of the tyre part	29
3.13	Internal parameters of the tyre part	30
3.14	Overview of the connection between tyre and lattice node	30
3.15	Overview of the wing-box in C-profile part	31
3.16	Internal parameters of the wing-box in C-profile part	32
3.17	Internal parameters of the two different ribs parts	34
3.18	Internal parameters of the two different ribs parts	35
3.19	Boundary condition for the model	37
3.20	Path of mesh elements on the solution model	38
3.21	Detail of the connection between the lattice nodes and the skin	39
3.22	Blocked translation and free rotation connection between the lattice nodes and the skin .	40
3.23	Free translation and rotation connection between the lattice nodes and the skin	40
3.24	Coupling condition between the lattice node and the wing-box skin through tyre	41
3.25	Local reference system at the lattice nodes	42
3.26	Coupling condition between the lattice node and the wing-box skin through a local reference system	43
3.27	Flow chart showing the execution of the parametric study code	45
4.1	Influence of the stiffness ratio on the wing-box tip twist and bend	48

4.2	Influence of the cross-sectional aspect ratio B/H on the torsional stiffness GI_t	51
4.3	Influence of the cross-sectional aspect ratio B/H on the dimensionless shear centre position y_{SC}/B	51
4.4	Influence of the cross-sectional aspect ratio B/H on the flexural stiffness EI_y	52
4.5	Influence of the wall thickness ratio t_2/t_1 on the torsional stiffness GI_t	52
4.6	Influence of the wall thickness ratio t_2/t_1 on the dimensionless shear centre position y_{SC}/B	53
4.7	Influence of the wall thickness ratio t_2/t_1 on the flexural stiffness EI_y	53
4.8	Influence of the cross-sectional aspect ratio B/H on the deflection compliance	54
4.9	Influence of the cross-sectional aspect ratio B/H on the torsional compliance	54
4.10	Influence of the thickness ratio t_2/t_1 on the deflection compliance	55
4.11	Influence of the thickness ratio t_2/t_1 on the torsional compliance	55
4.12	Influence of the slenderness ratio L/B on the deflection compliance	56
4.13	Influence of the slenderness ratio L/B on the torsional compliance	56
4.14	Distorted mesh elements in the model	57
4.15	Force-displacement curve for various values of constant artificial damping factor	59
4.16	External work and static dissipation for a damping factor equal to 2×10^{-5}	60
4.17	External work and static dissipation for a damping factor equal to 2×10^{-8}	60
4.18	External work and static dissipation for a damping factor equal to 2×10^{-9}	61
4.19	Vertical displacement v at the tip rib	62
4.20	Model response without the use of inner ribs nor automatic stabilization	63
4.21	Model response without the use of inner ribs with automatic stabilization	63
4.22	Model response incorporating inner ribs and without automatic stabilization	64
5.1	Baseline model response when the fraction of load applied equals to 63% of the prescribed load (700 N)	66
5.2	Baseline model response when the fraction of load applied equals to 80% of the prescribed load (700 N)	66

5.3	External work and static dissipation for a simulation of the baseline configuration	67
5.4	Force-displacement curve for the baseline configuration	68
5.5	Baseline model response when the fraction of load applied equals to 82% of the pre-scribed load (700 N)	68
5.6	Force-displacement curve for various values of the wing-box thickness	70
5.7	Detail of the force-displacement curve for various values of the wing-box thickness . . .	71
5.8	Color contour representation of the total angular displacement of the mesh elements on the deformed structure for $t_{\text{box}} = 1.2 \text{ mm}$	72
5.9	Color contour representation of the total angular displacement of the mesh elements on the deformed structure for $t_{\text{box}} = 0.8 \text{ mm}$	72
5.10	Force that induces the structure to collapse as a function of the wing-box thickness . . .	73
5.11	Force-displacement curve for various values of the number of unit cells in the transversal direction	75
5.12	Force-displacement curve for various values of the number of unit cells in the spanwise direction	76
5.13	Model response when the fraction of load applied equals to 96% of the prescribed load (700 N) and $N = 10$	76
5.14	Force-displacement curve for various values of the dimensionless chiral ligament eccentricity	78
5.15	Model response when the fraction of load applied equals to 100% of the prescribed load (700 N) and $\varepsilon_{\text{chiral}} = 0.1$	78
5.16	Force that induces the structure to collapse as a function of the chiral ligament eccentricity	79
5.17	Model response when the fraction of load applied equals to 72% of the prescribed load (700 N) and $\varepsilon_{\text{chiral}} = 0.0$	79
5.18	Model response when the fraction of load applied equals to 68% of the prescribed load (700 N) and $\varepsilon_{\text{chiral}} = 0.001$	80
5.19	Force-displacement curve for various values of the dimensionless chiral node depth . . .	82
5.20	Model response when the fraction of load applied equals to 86% of the prescribed load (700 N) and $B_{\text{chiral}} = 30 \text{ mm}$	82

5.21 Model response when the fraction of load applied equals to 62% of the prescribed load (700 N) and $B_{\text{chiral}} = 10 \text{ mm}$	83
5.22 Force that induces the structure to collapse as a function of the chiral node depth	83
5.23 Force-displacement curve for various values of the chiral node radius	85
5.24 Model response when the fraction of load applied equals to 100% of the prescribed load (700 N) and $r_{\text{chiral}} = 12.5 \text{ mm}$	85
5.25 Model response when the fraction of load applied equals to 100% of the prescribed load (700 N) and $r_{\text{chiral}} = 17.5 \text{ mm}$	86
5.26 Force that induces the structure to collapse as a function of the chiral node depth	86
5.27 Force-displacement curve for various values of the chiral ligament half length	87
5.28 Force that induces the structure to collapse as a function of the chiral ligament half length	88
5.29 Force-displacement curve for various values of the chiral structure thickness	89
5.30 Force that induces the structure to collapse as a function of the chiral structure thickness	90

List of Tables

3.1	Parameters used for the lattice model	25
3.2	Parameters used for the wing-box in C-profile model	31
3.3	Parameters used for the ribs model	33
4.1	Nominal value of the parameters used for the analytical model	47
5.1	Results from parametric study on the wing-box thickness	70
5.2	Results from parametric study on the number of unit cells in the transversal direction	74
5.3	Results from parametric study on the number of unit cells in the spanwise direction	75
5.4	Results from parametric study on chiral ligament eccentricity	77
5.5	Results from parametric study on chiral node depth	81
5.6	Results from parametric study on chiral node radius	84
5.7	Results from parametric study on chiral ligament half length	87
5.8	Results from parametric study on chiral structure thickness	89

ACTIVE FLEXIBLE WING

List of symbols

$\varepsilon_{\text{chiral}}$	Dimensionless ligament eccentricity	
\hat{x}	Dimensionless coordinate in the spanwise direction (x/L)	
\hat{y}	Dimensionless coordinate in the transversal direction in the computational model ($y_{\text{comp}}/H_{\text{box}}$)	
\hat{z}	Dimensionless coordinate in the chordwise direction in the computational model ($z_{\text{comp}}/W_{\text{box}}$)	
A	Cross sectional area for the analytical model	[mm ²]
A_{rib}	Rib frame width	[mm]
B	Width of the cross section for the analytical model	[mm]
B_{chiral}	Chiral node depth	[mm]
c	Artificial damping factor	
$d_{\text{chiral-rib}}$	Gap between lattice and inner ribs	[mm]
$E, E_1, E_2, E_{\text{chiral}}, E_{\text{box}}, E_{\text{rib}}$	Young's modulus	[N/mm ²]
e_{chiral}	Ligament eccentricity	[mm]
$G, G_1, G_2, G_{\text{chiral}}, G_{\text{box}}, G_{\text{rib}}$	Shear modulus	[N/mm ²]
H	Height of the cross section for the analytical model	[mm]
$H_{\text{box}}, H_{\text{rib}}$	Height for the wing-box and the ribs	[mm]
I_t	Torsional constant	[mm ⁴]
L	Length of the beam for the analytical model	[mm]
L_{box}	Length of the wing-box in the spanwise direction	[mm]
L_{chiral}	Chiral ligament half length	[mm]

M	Number of unit cells in transversal direction	
N	Number of unit cells in spanwise direction	
q_0	Constant shear flow	[N/mm]
q_C	Close section shear flow	[N/mm]
q_{\parallel}	Open section shear flow	[N/mm]
Q_z	Force in direction of z	[N]
r	Radial position in the local cylindrical reference system	[mm]
R_{chiral}	Ligament eccentricity radius	[mm]
r_{chiral}	Chiral node radius	[mm]
S_c	Course mesh size	
S_f	Fine mesh size	
S_{E_y}	First moment of area	[N mm]
$t, t_1, t_2, t_{\text{chiral}}, t_{\text{box}}, t_{\text{rib}}$	Wall thickness	[mm]
u	Displacement along the x direction	[mm]
v	Displacement along the y direction	[mm]
w, w_0	Displacements in direction of z	[mm ²]
$W_{\text{box}}, W_{\text{rib,close}}, W_{\text{rib,open}}$	Width for the wing-box and the ribs	[mm]
x	Coordinate in the spanwise direction	[mm]
$y_{\text{ana}}, z_{\text{comp}}$	Coordinate in the chordwise direction for the analytical and computations reference systems	[mm]
z	Perpendicular position in the local cylindrical reference system	[mm]
$z_{\text{ana}}, y_{\text{comp}}$	Coordinate in the transversal direction for the analytical and computations reference systems	[mm]
$\nu, \nu_{\text{chiral}}, \nu_{\text{box}}, \nu_{\text{rib}}$	Poisson's ratio	
$\phi, \phi_{\text{tip}}, \tilde{\phi}_{\text{tip}}$	Twist angle	[deg]
Φ_y	Flexural stiffness	[N mm ²]

θ	Angular position in the local cylindrical reference system	[rad]
$\vartheta w, w_0$	Specific twist angle	[deg/mm]

Abbreviations

AAW	Active Aeroelastic Wing
ABS	Acrylonitrile butadiene styrene
AFW	Active Flexible Wing
CAE	Complete Abaqus Environment
CFRP	Carbon Fibre Reinforced Plastic
CMAS	Composite Materials and Adaptive Structures Lab
ETH	Eidgenössische Technische Hochschule Zürich
FEM	Finite element method
NASA	National Aeronautics and Space Agency
SMA	Shape Memory Alloy
VSS	Variable Stiffness Spar

Chapter 1

Introduction

The interest in morphing of the aerodynamic surfaces has accompanied aerospace history since the beginning. Since the first heavier-than-air flight in 1903, when the Wright Brothers designed and built a powered heavier-than-air aircraft that achieved the first controlled and sustained flight. Their design incorporated a mechanism that provided lateral control by manually changing the twist of the wing. Since then, the necessity of enhanced performance and higher airspeed brought the requirement of stiffer wing structures to avoid aeroelastic instabilities. This caused that the idea of a flexible wing with morphing capabilities was left behind.

On conventional aircraft, the need to modify the airflow around the airfoil at different flight conditions is achieved through discrete hinged mechanics such as flaps and ailerons. These mechanisms perform well in a limited range around the design point while outside this range, they have a negative influence in the aerodynamics. The necessary discontinuities that these elements produce on the surface, advance the boundary layer transition point from laminar to turbulent regime. Being able to modify the airflow without discontinuities on the surface would come along with notable reductions in parasite drag and therefore in fuel consumption.

One of the applications of aircraft morphing is the counteracting of the excessive aerodynamic load originated after gust encountering. This is a flight condition under which the aircraft experience critical loads that mark the design point for the airframe due to its structural integrity threat. In this event, the aircraft is flying in turbulent air and a component of the velocity of air normal to the flight path changes the effective angle of incidence of the aerodynamic surfaces increasing its aerodynamic load. In Figure 1.1, the case of an aircraft encountering a vertical gust is shown. Several mechanisms which usually add structural mass have been developed to withstand this rare scenarios. The requirements of such solutions require of a rapid modification of the lift distribution that mitigates the impact of such events. In modern transonic aircraft, after a gust encountering, the ailerons of both wings are deflected in such a way that they reduce the local airfoil camber, reducing as well the lift generated at the wing tip.

Furthermore, the use of wing morphing attempt to modify wing geometrical parameters of relevance such as the twist and provide gust load alleviation, has been always something of interest for

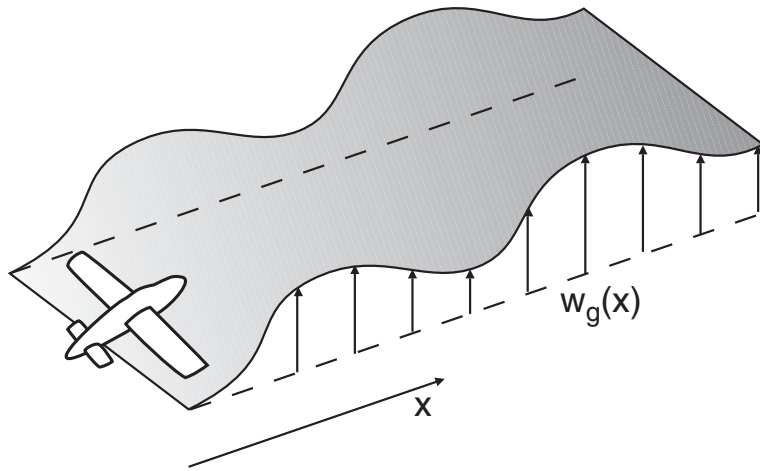


Figure 1.1: Aircraft encountering a vertical gust. [1]

researches. These type of solutions show compliance with the response requirement exposed in previous paragraph, in addition of having advantages such as the weight reduction and/or the no alteration of the aerodynamic surfaces continuity with hinges, providing reduced operation costs and aerodynamic performance enhancement, respectively.

The present work is a proposal of a novel wing morphing technology that enables the rapid alteration of the wing twist. This alteration would reduce the angle of attack and therefore would limit the aerodynamic load on the wing . The presented concept consists on the alteration of the torsional stiffness of the wing-box of the wing by the inclusion of a variable-stiffness spar. The modification of the effective shear modulus in this element provokes the wing-box center shifting. This event is fully passively activated and its based on the appearance of elastic controlled instabilities in the structure of the variable-stiffness spar.

The objectives for the work presented in this thesis include on first place the evaluation of the buckling mechanism as a valid trigger for the variable-stiffness spar adaptation and consequent variation of the wing-box twist. Secondly, the elastic instability or buckling that arises in the spar is aimed to be characterized by qualitative means. Finally, the possibility of tailoring the deformation response by varying the structure parameters is intended to be evaluated.

This thesis is organized as follows: succeeding this introduction, the state-of-the-art of the technologies related to the one proposed in this work are presented. Then, the wing-box model that has developed to investigated the suggested concept is explained in the third chapter, following a characterization of its mechanical properties in the subsequent chapter. The fifth chapter shows the results obtained from the simulations performed on the computational model of the wing-box. The conclusion and outlook complete this thesis.

Chapter 2

State-of-the-art

This chapter presents a review of the current technologies related to the topic of this work will be done. Different morphing wing technologies will be introduced. Secondly, a particular focus on the state-of-the-art of technology exploit in the current project will be presented.

2.1 Morphing aircraft

Their concept of aircraft did not provide importance to built-in stability but absolute control of the aircraft by the pilot. For this reason, they deliberatively designed their first aircraft with anhedral wing that make it dynamically unstable to perturbations in sideslip but more maneuverable in the lateral direction. In order to achieve roll control, they decided to incorporate a mechanism that would allow the wings to twist by pulling from cables, as it can be seen in Figure 2.1. This was the first ever use of morphing of an aerodynamic surface for aircraft control.

New interest has raised in the recent years in aircraft morphing, mainly due to the appearance of new smart materials that allow more efficient mechanical design that do not necessarily incur in weight increments [3]. Another reason that is pushing forward new aircraft morphing technologies is that missions today are in need of higher aircraft versatility to decrease operational costs in the commercial aviation field and aim to smaller and more distributed targets in the military field. For example, Airbus has recently patented a design of a downwardly foldable wing tip device applicable for a large passenger aircraft [4].

A general classification of different wing morphing concepts can be seen in Figure 2.2: planform modification through variation of sweep angle, span or chord; out-of-plane alteration involving twist, dihedral angle and spanwise bending, and airfoil adjustment achieved by modifications of the airfoil chamber and/or thickness. Under this classification, the morphing technology that is the focus of the work presented in this thesis is located under the out-of-plane branch and twist modification.

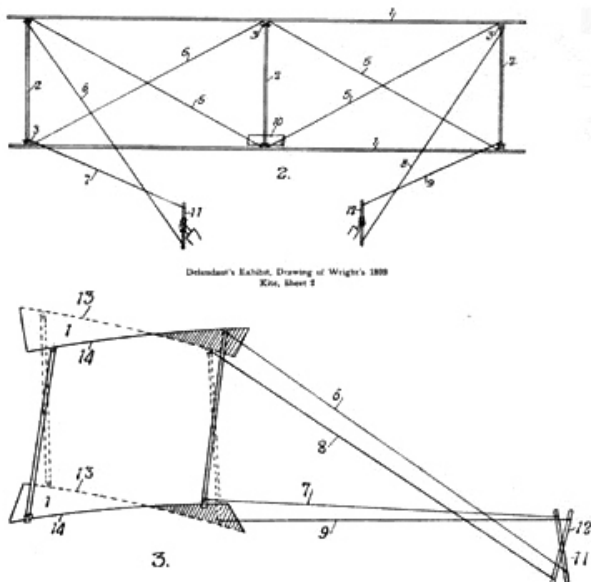


Figure 2.1: Wright Brothers 1899 kite: front and side views, with control sticks. Wing-warping is shown in lower view. [2]

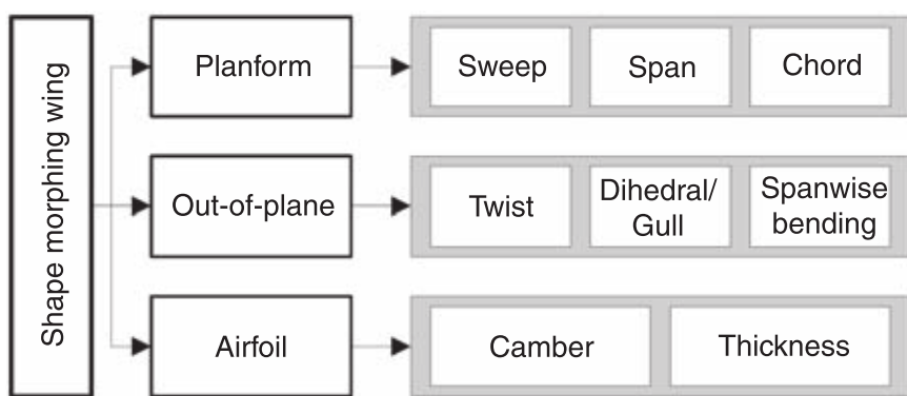


Figure 2.2: Shape morphing wing classification. [5]

In the field of wing morphing through active aeroelastic concepts, the pioneer program of the Active Flexible Wing (AFW) was developed by Rockwell International in the 1980s [6]. Under this program, a design of an aircraft where the wing aeroelastic twist was used to produce the required roll moments for control was generated. This enabled the aircraft to operate at dynamic pressures beyond those where conventional ailerons suffer from the appearance of reversal aeroelastic instabilities. Later, NASA continued with the AFW concept within their Active Aeroelastic Wing (AAW) project which used a modified F-18 fighter named X-53 to perform flight test and assess the viability of the proposed concept. A picture showing this aircraft can be seen in Figure 2.3. The X-53 had its wings modified to reduce the torsional stiffness and had additional actuators added to operate the outboard leading-edge flaps separately from the inboard leading-edge surfaces [7]. Rolling moment was obtained by aeroelastic twist of the wing using trailing-edge control surfaces and leading-edge flaps.



Figure 2.3: The X-53 performing a 360° roll to prove AAW technology. [7]

Following that initial attempts , many additional research literature can be found for other approaches. Many of those, consisted in modifying the wing properties by active means, i.e.: incorporating actuators that introduce energy into the system. Among the vast available literature in this field, it is worth mentioning the advances made in [8] by the development of a variable stiffness spar (VSS) concept to control the torsional stiffness as a function of the Mach number and the altitude. Also, in the investigation presented by [9], the adaptive torsional stiffness for a vertical tail was achieved by a variable attachment point position. The work presented by [10] showed how roll control of a small aircraft could be achieved by actively twisting its flexible wing. The technology of the shape memory alloys (SMA) has been also exploit in the field of active wing twist morphing, as seen in [11] and [12].

However, wing twist morphing designs may also benefit from geometrically flexible structures if the aeroelastic energy from the airstream can be used to activate the shape changing mechanics. Such an approach may lead to passive morphings strategies that are always preferred since no additional energy

is necessary to be introduced into the system and the usual weight penalties of morphing may be avoided if no additional actuators are needed.

In [13], a passively triggered system to reduce the lift increment that follows a gust encounter using multi-stable elements embedded into the airfoil is presented. Other examples of wing twist morphing by passive means are those presented in [14], [15] and [16]. In particular, the technology proposed in these works exploits the capabilities of the chiral structures that feature a negative Poisson's ratio for in-plane strains. A network of these chiral structure is embedded in the rib of the airfoil constituting the deformable part. These chiral structures will be extensively discussed in the next section.

Also in the field of passive approaches to achieve wing twist morphing, W. Raither proposed in [17] a novel concept of adaptive aeroelastic tailoring by means of the wing-box torsional stiffness modification. In order to achieve this, the shear stiffness G_t of one of the webs that conform the wing-box beam is modified. This induces the section's shear centre shifting, which provides an additional torsional deformation for a constant load. This concept is later explained in Section 3.1 as the same working principle is used for the technology presented in this work.

Implementation of the proposed principle requires a material with controllable in-plane shear modulus. A possible solution is proposed in [18] and consisted in the use of electro-bonded laminates that vary its bending stiffness by means of electrostatic forces applied different at points of the structure. Another approach is presented in [19], and exploits the time-variable lamination in laminate composite shells provided by the temperature dependence of the elastic modulus of polymers in proximity of their glass transition. Therefore, the proposed concept consists on a semi-passive approach since some energy needs to be spent for the activation of the adaptive interfaces. In [20] the demonstrator shown in Figure 2.4 was built to show the viability of this last approach.

Finally, in [21] the variation of in-plane shear modulus is proposed that can be achieved by inducing elastic instabilities on one of the webs of the wing-box. The component is manufactured with a particular material anisotropy utilizing unidirectional CFRP. The appearance of plate buckling at the root on the specially designed web, as shown in Figure 2.5, induces the shear centre location shifting and the torsional stiffness of the structure, thus leading to a purely passive bending-twist coupling. In [22], the mechanical response was investigated using FE simulations and experimental testing on a manufactured demonstrator of the concept.



Figure 2.4: Inner structure of the experimental wing build to test the concept of adaptive wing-box. [20]

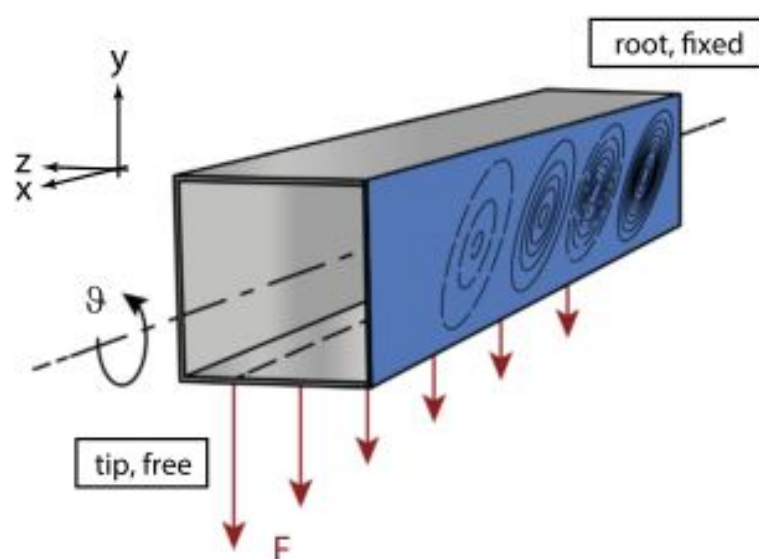


Figure 2.5: Plate buckling on one of the webs of the wing-box beam. The drawing shows a qualitative view of the buckling field. [21]

2.2 Compliant chiral structure

As mentioned in the introduction, it is the interest of this work to use structures that have recently been of interest due to its capabilities as materials with negative Poisson's ratio. Such materials expand laterally when stretched and contract laterally when compressed. In [23], R. Lakes proposed that negative Poisson's ratios can result from a hexagonal microstructure of rotatable nodes and bendable ligaments such as the one shown in Figure 2.6. Such structures are known as non-centrosymmetric, hemitropic, or chiral; they are distinguishable from their mirror image; that is, they cannot be superposed onto them and they are not isotropic.

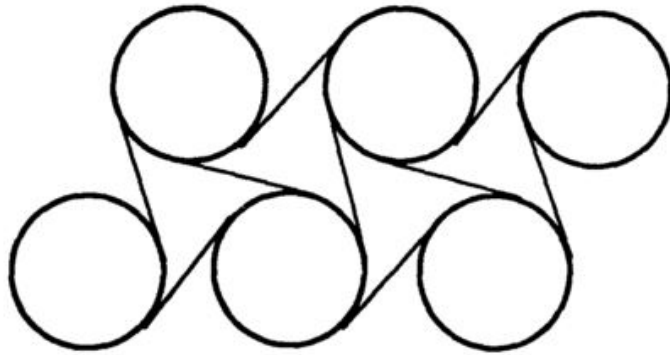


Figure 2.6: Chiral (noncentrosymmetric) hexagonal microstructure of rotatable nodes and bendable ligaments. Poisson's ratio is negative. [23]

In [24], experimental results showed that the a honeycomb chiral structure exhibited a Poisson's ratio of -1 for deformations in-plane. Indeed, this behavior was maintained over a significant range of strain, as shown in Figure 2.7, and therefore verifying that Poisson's ratio is independent upon the strain, in agreement with theory.

In [25] the properties of a chiral honeycomb are investigated, a manufacturing process using composite materials is proposed and the increase in the performance of using such materials is shown. Also, the experiments carried out allowed to characterize the possible failure modes of this structures and the nonlinear response when large displacements occur.

Until that moment, most of the work was concentrated in studying the in-plane behavior of the chiral structures. Then, in [26] the flatwise compression behavior of the chiral structures is investigated through FE modeling and simply analytical relations. This is the first consideration of buckling in a chiral structure in some way, in this case it was the out-of-plane buckling behavior based on the similar works presented in [27] and [28] for honeycomb structures. This research was extended by experimental studies in [29] and an anelastic characterization of the buckling phenomena is presented in [30]. The buckling response of chiral honeycombs under a general macroscopic in-plane stress state was more recently investigated from a theoretical point of view in [31].

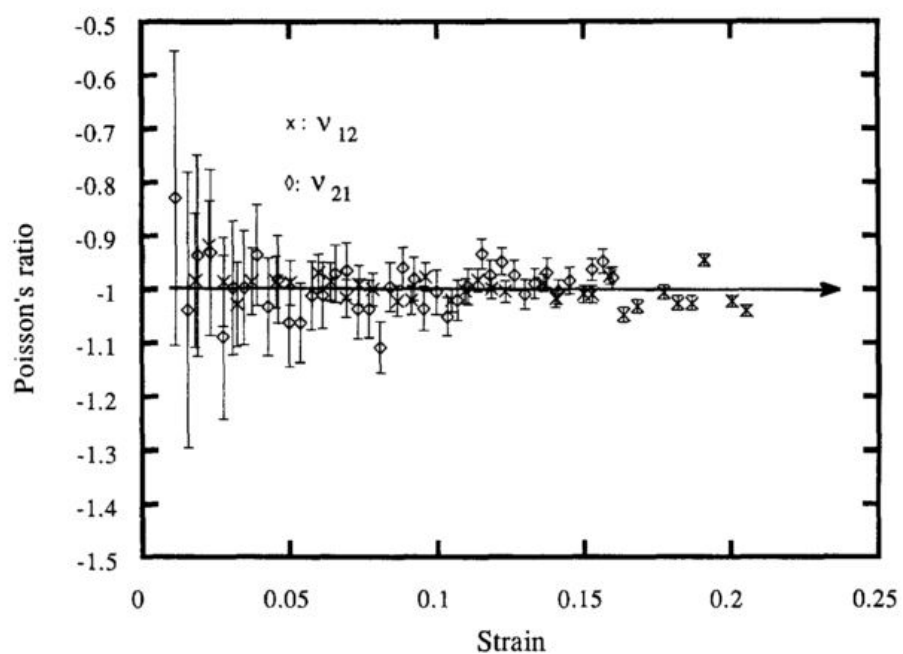


Figure 2.7: Experimental Poisson's ratio v as a function of axial compressive strain on a chiral honeycomb. The error bars represent inaccuracies due to the measurement resolution. [24]

Within the research undertaken at the Laboratory for Composite Materials and Adaptive Structures (CMAS) of the ETH Zürich in the field of variable stiffness structures, a novel chiral topology has recently been proposed. The chiral unit cell is modified by introducing transverse curvature into the ligaments, as shown in Figure 2.8(b). Such design increases the bending stiffness of the ligament and thus of the entire periodic structure. Each ligament posses double eccentricity which changes orientation at the centerline of it, in compliance with a equivalent connection with the cylinders located at the extremes. In [32] preliminary investigations of such structures were experimentally conducted on a conceptual level for a basic triangular chiral structure, as shown in Figure 2.9.

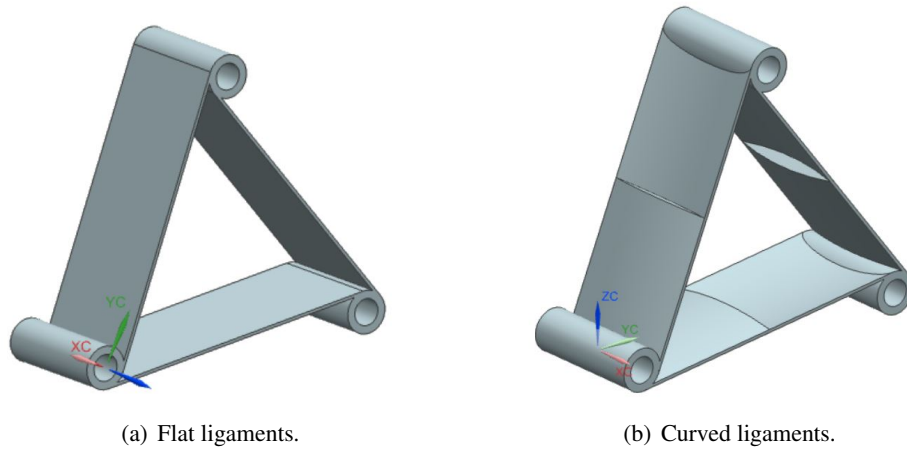


Figure 2.8: Chiral cell elements showing different ligaments curvatures. [32]

This new design of the ligaments will provide additional tailorability over the buckling phenomena occurring on the lattice ligaments. This configuration is the one chosen for the chiral structure that is used in the concept presented in this work.

Different approaches have been followed to exploit the particular characteristics of chiral structures under in-plane strain, on aerodynamic elements such as airfoils. In [14] a truss-core configuration such as the one shown in Figure 2.10(a) with chiral topology was utilized to design an airfoil for automotive competitions. The concept exploits the elastic deformation of the chiral lattice to modify the airfoil mean chamber line and thus modifying the pressure distribution as required for the current desired performance of the car. In [15], a similar configuration was investigated by weakly coupled structural and CFD models, and the local and global deformations were characterized by consideration of the macroscopic chiral configuration. A prototype of the proposed design, as shown in Figure 2.11, was manufactured and tested in [16]. Results showed a remarkable tailoring of the chamber morphing performance by means of a limited number of parameters which define the core geometry. The dynamic properties of such chiral truss-core assemblies were investigated in [33].

Recently, A. Airolidi developed the “chiral sail” concept in [34] which exploits the chiral topology of a chiral network embedded into the airfoil rib. The pressure difference between the upper and lower parts of the airfoil promotes the chamber variation as shown in Figure 2.12 and amplifying the lift when the

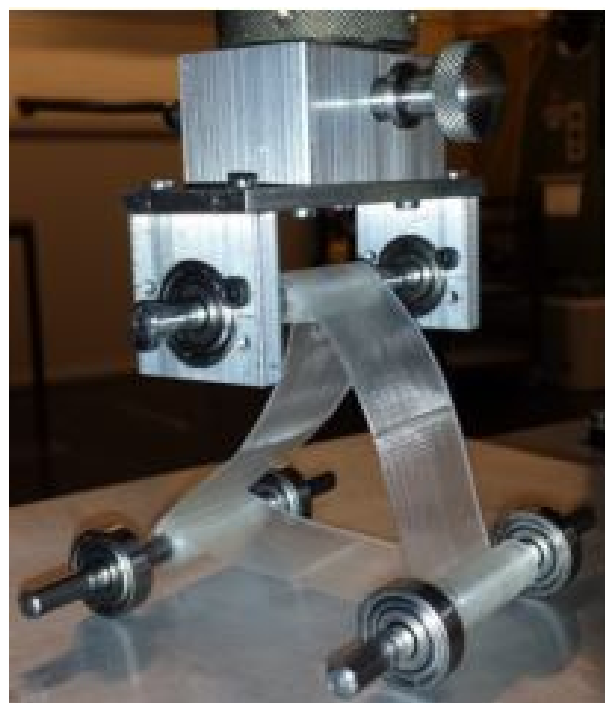


Figure 2.9: Compression load test on a basic triangular chiral structure. [32]

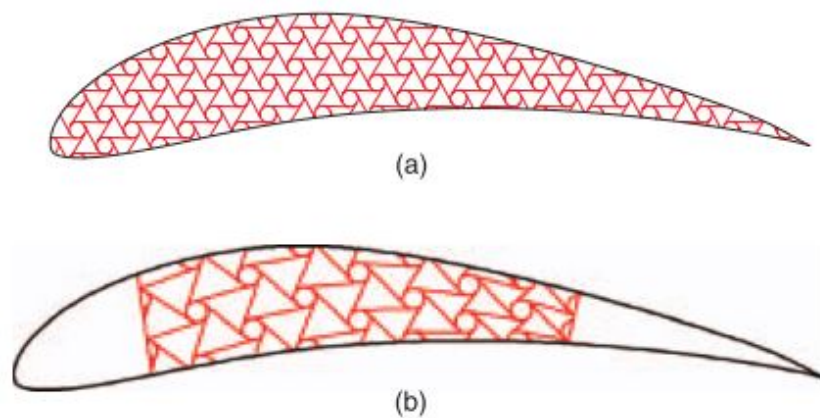


Figure 2.10: Investigated configurations for the truss-core of chiral topology. [15]

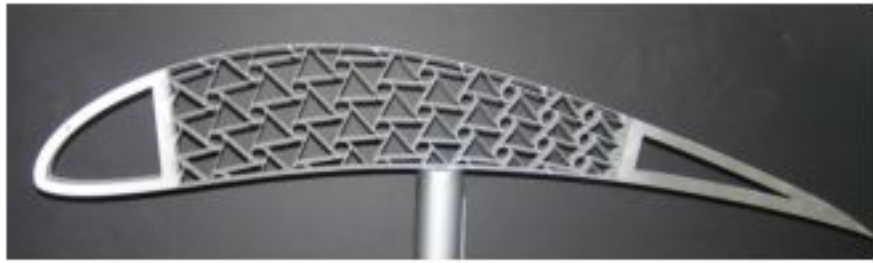


Figure 2.11: Manufactured prototype of a truss-core airfoil with chiral topology. They were manufactured in aluminum, using water-jet cutting techniques. [16]

angle of attack increases. This concept was implemented and validated by testing a demonstrator in [35]. The experimental side of this work showed the difficulties of manufacturing such complex structures.

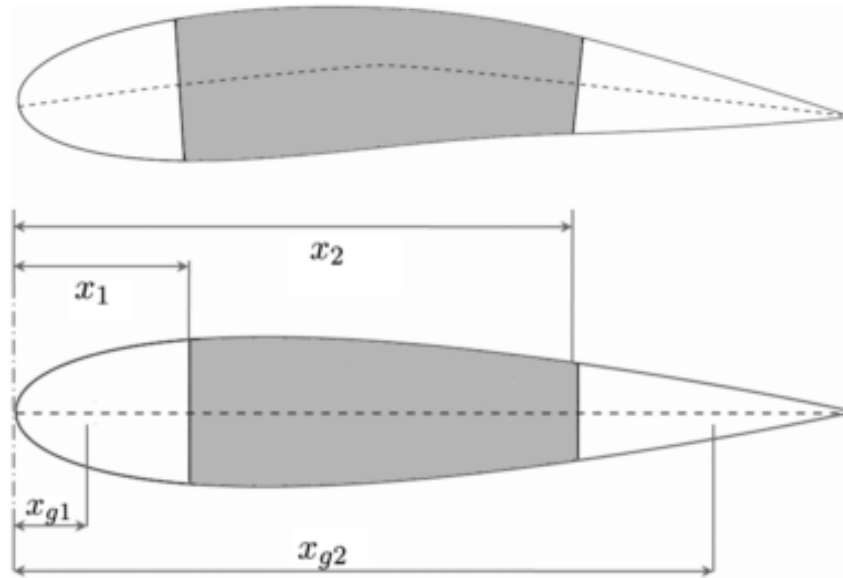


Figure 2.12: Chiral sail concept. The rib of the airfoil is constituted of a network of chiral unit cells. [34]

2.3 Rationale for the thesis

This thesis is part of the current research that it is been carried out at CMAS in seek of wing twist morphing achieved through variable stiffness wing-box structures that acquire this property undergoing elastic instabilities.

As shown in the topic review presented in [36] and [37], the use of buckling-induced technologies is a promising technique to achieve the desired behavior in recent developments of smart structures. Traditionally, elastic instabilities were avoided in the structural designs due to the significant loss of load-carrying capacity and the large deformations occurring as a consequence of such an event. However, in the scope of the so called motion-related applications of buckling-induced technologies, the capability of small perturbations to generate sudden snapping behavior in elastic elements enables the structure to dynamically change its configuration, being this beneficial for applications such the one considered in the present work. Also, the possibility of minimizing the actuation force required during shape recovery due to the elastic state of the structure becomes interesting.

In parallel, when it comes to the bending-twist shape adaptation by compliant structural designs, some of the solutions already introduced in this chapter are able to modify the wing-box torsional stiffness for a pre-defined shape variation or are optimized for a given actuation lay-out, whereas the adoption of a structural concept such as a chiral lattice offers a wide range of possibilities in terms of tailoring. In particular, the chiral structures that posses curved ligaments are the design option for the concept proposed in this work. This novel characteristic is expected to provide additional control over the buckling appearance and evolution. This design of chiral structure was already manufactured and tested in another project completed at CMAS [38].

Thereby, for the approach presented in this work, the working principle introduced by [17] is combined with the buckling capabilities of the chiral structures exposed in Section 2.2 to conform the proposed principle.

In the scope of this thesis, a full model of the whole wing-box with the compliant variable-stiffness spar is studied. It is the intention to look at the buckling characteristics of the lattice of chiral structures that conforms the spar and the response in twist of the whole assembly. It is expected to see buckling occurring on several ligaments at the same time at of those located close to the root of the wing-box. Also, it is envisioned that the buckling phenomena activates a sudden change in the twist of the wing-box. Also, the modification of internal parameters of the chiral structure is expected to show promising tailorability capabilities on the force-displacement curve.

It is expected that the proposed technology will be suitable for environments where a rapid shape adaptation is required. Such applications may include to increase the critical speed for load alleviation purposes.

In order to achieve verification of the previous premises, a numerical and analytical model model will be built of the whole wing-box assembly. The evolution of the buckling phenomena for in the structure will be characterized and the effect of the different design parameters on the structure pre-buckling and

post-buckling response will be assessed. The aim is to provided a suitable computational environment to achieve in-deep understanding of the proposed working principle and assist the manufacture of a future demonstrator.

Chapter 3

Wing-box model

A model of the whole wing-box including the variable-stiffness spar is developed to study the buckling characteristics of the chiral lattice, the response in twist of wing-box and the tailorability possibilities of that response. In the present chapter the model is presented, which in fact consists in two models one analytical and another one computational.

On first place, the working principle that lays under the proposed technology is presented. Next, the two different models developed to provide fully understanding of the structure response are presented. Firstly, a simple analytical model of a beam with a web featuring variable stiffness properties is presented. This is used to provide fast insight of the role of each of the design parameters on the final mechanical properties of the beam. Important relevance is given to the section's shear centre y_{SC} shifting. This variable determines the magnitude of the resulting torsional moment that acts on the beam as a result of a load applied on the beam's transversal plane, and that induces the beam twist.

Secondly, the computational model is introduced. The different constituting elements are explained together with the boundary conditions, loads and mesh that are used in the simulations

Finally, the program used to carry out automatic parametric studies is presented, together with its methodology.

3.1 Concept

As it was already introduced in last chapter, the proposed technology to achieve twist morphing through a variable torsional stiffness wing-box is based on the working principle presented in [17] and exploits the buckling characteristics of a lattice of chiral ligaments as a way of varying the effective shear modulus G_{eff} the adaptive spar of the wing-box.

The basic working principle consisted on employing profile beams in which the shear centre is shifted

as a result of the variable-stiffness capability of one of the webs. An schematic view of the working principle is shown in Figure 3.1 where an adaptive beam is displayed. In Figure 3.1(a), the four webs that constitute the rectangular profile of the beam have the same shear stiffness $G_2 t_2 = G_1 t_1$. The double symmetry characteristic of such a configuration indicates that the shear centre is located at the point where the two symmetry axes intersect. For this case, under a load applied on the shear centre, the beam experiences bending deformation with null twist. On the other hand, when considering the situation shown in Figure 3.1(b) where $G_1 t_1 > G_2 t_2$, the reduced shear stiffness of the adaptive web produces that shear centre moves along the y direction and towards positive values of y . In this case, if the load is maintained in the same application point as before, the beam experiences bending deformation and negative twist. Correspondingly, for the case shown in Figure 3.1(b) where $G_2 t_2 > G_1 t_1$, the shifting of the shear centre is towards negative values of y and the beam experiences a positive twisting under the prescribed load.

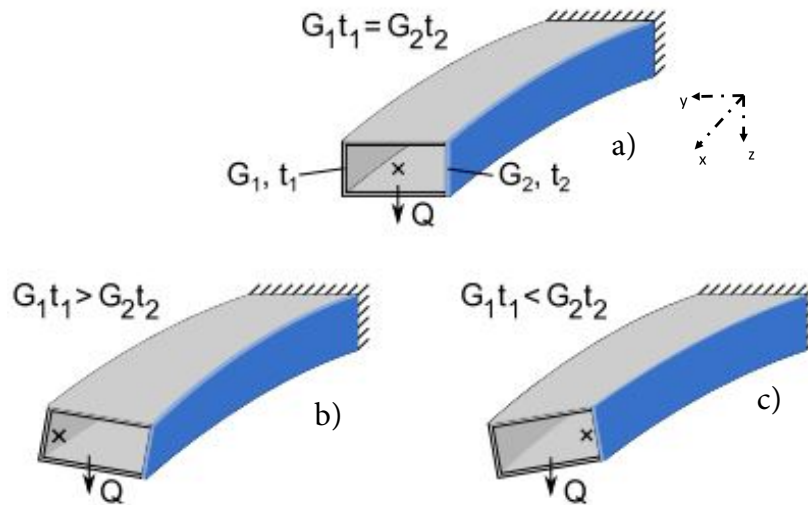


Figure 3.1: Working principle for the adaptive beam. [20]

The bending-twist coupling of the beam can therefore be controlled by the variable-stiffness web. The properties of the web can be modified by either adjusting the shear modulus G_2 or the thickness t_2 of the web.

In the technology presented in this work, the adaptive web is constituted of a lattice of chiral structures. On these elements, elastic buckling is intentionally induced and the resulting consequence is the reduction of the overall shear modulus G_2 effectively introducing an effective shear modulus $G_{2,\text{eff}} < G_1$. An example of the chiral structure undergoing buckling instabilities on some of the ligaments located at the wing-box root can be seen in Figure 3.2.

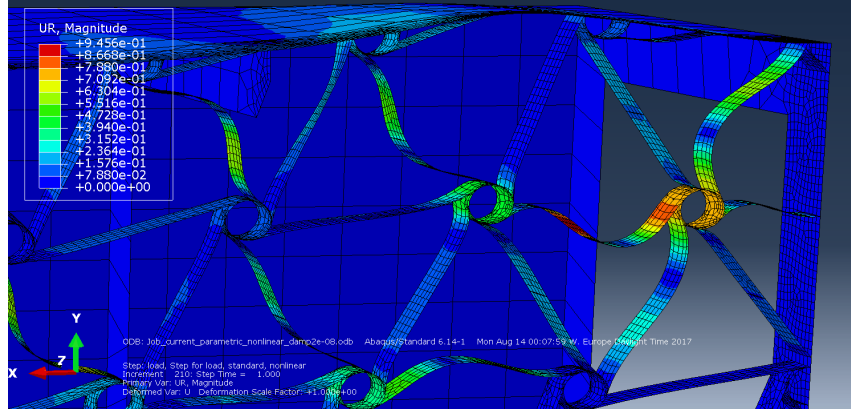


Figure 3.2: Set of chiral ligaments undergoing instabilities at the root of the wing-box.

3.2 Analytical model

The analytical model of the wing-box is presented in the present section. An schematic view of the section of the beam can be seen in Figure 3.3. The main dimensions for the section are given by the height H and the width B . Such a structure if characterized by having three elements with identical thickness t_1 , shear modulus G_1 and Young's modulus E_1 . For the element on the right, the adaptive web, the same parameters are t_2 , G_2 and E_2 , respectively.

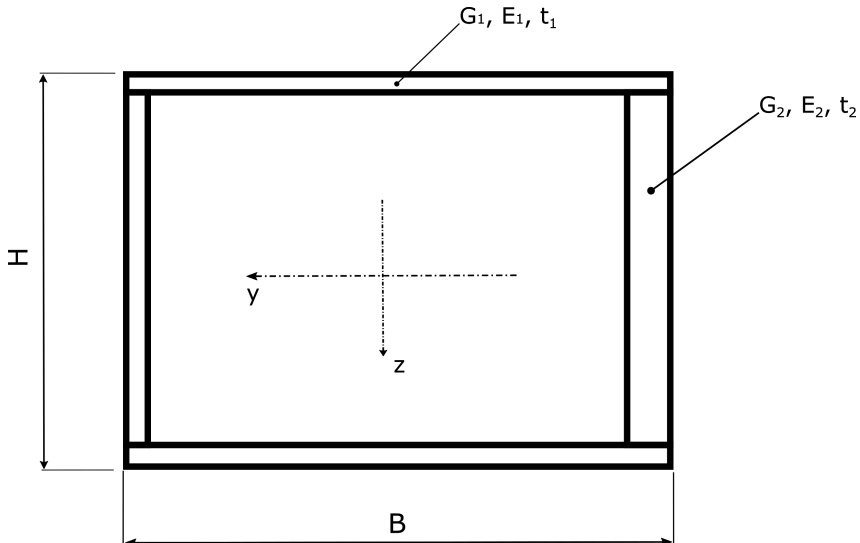


Figure 3.3: Schematic view of the beam closed section. The dimensions are given by the width B and the height H . For the upper, lower and left elements, the wall thickness, shear modulus and the Young's modulus are given by t_1 , G_1 and E_1 , respectively. For the right element, the same parameters are given by t_2 , G_2 and E_2 .

As explained in Section 3.1, the shear stiffness Gt of the adaptive web can be modified by varying either thickness t or shear modulus G . For the remaining, it is assumed that $t_1 = t_2 = t$ and therefore the thickness t will not be considered as a modifiable parameter on the adaptive web.

Now the bending-twisting coupling of the structure is investigated using well-known equation to describe the elastic behavior of thin-wall beam elements. Based on the analytical approach to the problem of a beam bending-twisting coupling followed in [17], it is known that warping can be neglected for a configuration like the one presented in this section.

The bending displacement of the structure is therefore given by Equation 3.1 which is a solution of the well-known Bernoulli-Euler equation for a beam:

$$w_b = \frac{QL^3}{6\Phi_y} \left(-\frac{x^3}{L^3} + \frac{3x^2}{L^2} \right), \quad (3.1)$$

where w_b is the displacement along the z direction and Φ_y is the flexural stiffness given by Equation 3.2:

$$\Phi_y = \int \int E(y, z) z^2 dy dz. \quad (3.2)$$

On the other hand, the twist of a beam with closed section can be obtained from the St. Venant expression for the specific twist ϑ , which is shown in Equation 3.3:

$$\vartheta = \frac{d\phi}{dx} = \frac{M_t}{4A_0^2} \oint \frac{ds}{Gt}, \quad (3.3)$$

where A_0 represent the area enclosed by the profile's wall midline, ϕ is the twist of the beam and M_t is the torsional moment applied. Additionally, the torsional stiffness for the closed section under study is given by the Equation 3.4:

$$GI_t = \frac{4A_0^2}{\oint \frac{ds}{G(s)t(s)}}. \quad (3.4)$$

In order to calculate the specific twist ϑ , it is necessary to evaluate the shear centre position y_{SC} for a given configuration. In order to achieve this, evaluation of the shear flow distribution in the section also needs to be undertaken. To calculate the shear flow $q(s)$, the profile can be considered to be cut at one point, resulting on an opened section. The shear flow $q_{||}(s)$ for this case can be calculated using Equation 3.5. The corresponding shear flow for a closed section can be obtained using the Equation 3.6:

$$q_{||}(s) = -\frac{Q_z}{\Phi_y} S_{E_y}(s), \quad (3.5)$$

$$q_C(s) = q_{||}(s) + q_0, \quad (3.6)$$

where Q_z is the force applied in the z direction and S_{E_y} is the so called static moment or first moment of area, which is calculated through the integral shown in Equation 3.7. Also, the variable q_0 represents the shear flow at the boundary that results from the torsion of the beam and can be calculated using the Equation 3.8:

$$S_{E_y}(s) = \int_0^s E(s)t(s)z(s)ds, \quad (3.7)$$

$$q_0 = \frac{Q_z}{\Phi_y} \frac{\oint_s \frac{S_{E_y}(s)}{G(s)t(s)} ds}{\oint_s \frac{1}{G(s)t(s)} ds}. \quad (3.8)$$

Now, the shear centre position in the beam transversal section will be calculated for the case of open section. Given that beam mechanical properties and geometrical dimensions are symmetric around y axis, the shear centre position in the z axis will be $z_{SC} = 0$. On the other hand, the shear centre position in the y axis will be given by the Equation 3.9:

$$y_{SC,open} = \frac{1}{Q_z} \oint_s q_C(s)r(s)ds, \quad (3.9)$$

where r represents the perpendicular distance to the coordinate origin.

Now, it is necessary that equilibrium exists between the torsional moment due to the shift of the shear centre (caused during the opening of the profile) and the moment due to the torsional shear flow of the closed profile. This condition can be mathematically expressed through Equation 3.10:

$$\begin{aligned} M_t &= Q_z(y_{SC,open} - y_{SC,closed}) \\ &= 2A_0q_0. \end{aligned} \quad (3.10)$$

The above equality enables on one hand the calculation of the closed section shear centre position $y_{SC,closed}$ using Equation 3.11:

$$y_{SC,closed} = y_{SC,open} - \frac{2q_0A_0}{Q_z}, \quad (3.11)$$

and the the calculation of the torsional moment M_t acting on the beam on the other hand using Equation 3.12:

$$M_t = Q_z(y_{load} - y_{SC,closed}), \quad (3.12)$$

that considers the position y_{load} where the load is applied.

Finally, once the torsional moment M_t acting on the beam is known, it is possible to calculate the beam twist $\phi(x)$ using Equation 3.3 and considering that $\phi(x) = \vartheta x$.

3.3 Computational model

The computational model of the wing box is built using Abaqus CAE commercial software. It consists on three main elements: the wing-box with C-profile, the lattice constituted of the chiral elements, a closed rib at the tip of the box and a closed rib at the root of the box. A general overview of the assembly of the different parts can be seen in Figure 3.4.

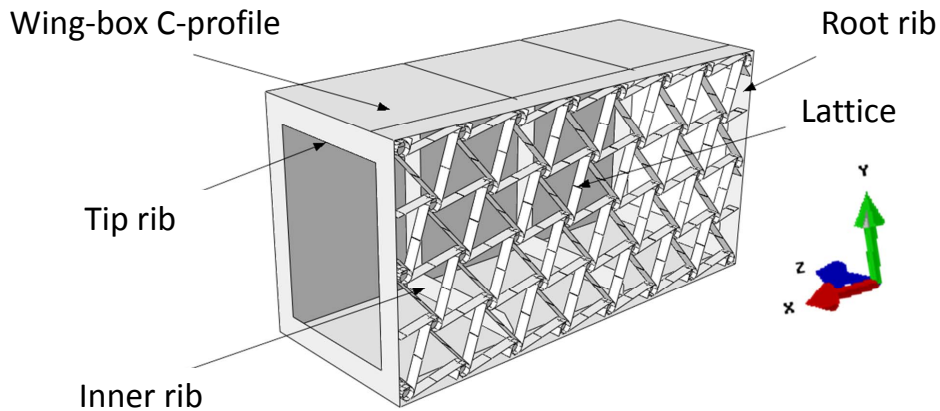


Figure 3.4: General assembly configuration for the computational model. The different parts for the general configuration include the wing-box profile, the lattice and the pair of ribs located at the tip and the root of the wing-box.

The discretization of the structural element was done using continuum shell elements as the basic constituting part. An sketch of a continuum shell element as defined in Abaqus can be seen in Figure 3.5.

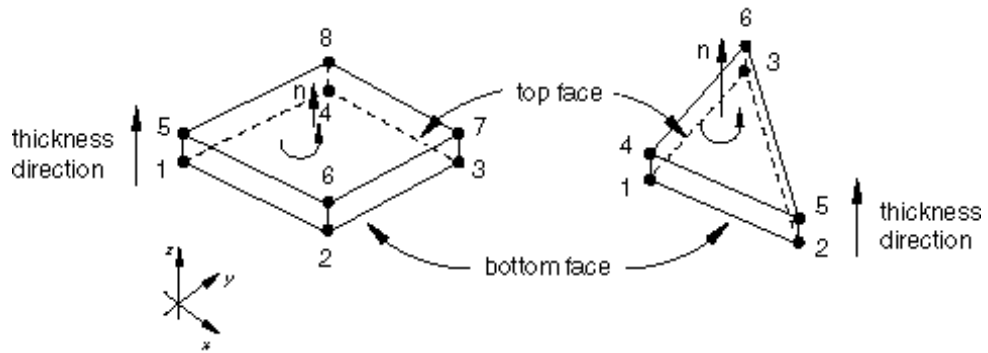


Figure 3.5: Default normals and thickness direction for continuum shell elements in Abaqus. [39]

3.3.1 Sub-parts and parametrization of the model

Lattice of chiral elements

The model of the lattice structure is constituted of a network of rigid nodes interconnected by ligaments. At each node, there are six ligaments attached in a uniform distribution that leaves an angular separation of 60° between consecutive attachment points. This network constitutes a lattice of chiral elements. An overview of this part can be seen in Figure 3.6. The lattice structure is divided in an integer number of unit cells in the longitudinal (spanwise) and transversal directions. These parameters are identified with the variables N and M for the longitudinal and transversal directions, respectively. In Figure 3.7, an sketch of the internal division for $N = 8$ and $M = 3$ is shown. It displays a set of horizontal rectangles that represent each of the transversal M divisions while the set of vertical rectangles correspond to each of the N longitudinal divisions.

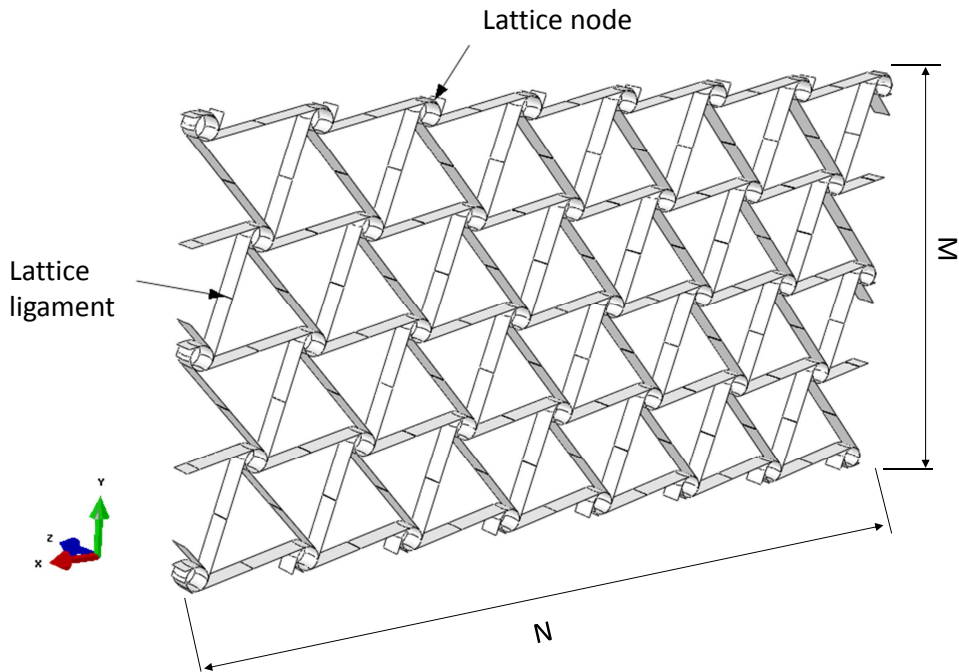


Figure 3.6: Overview of the chiral lattice part. The parameters N and M represent the number of unit cells in the longitudinal (spanwise) and transversal directions, respectively.

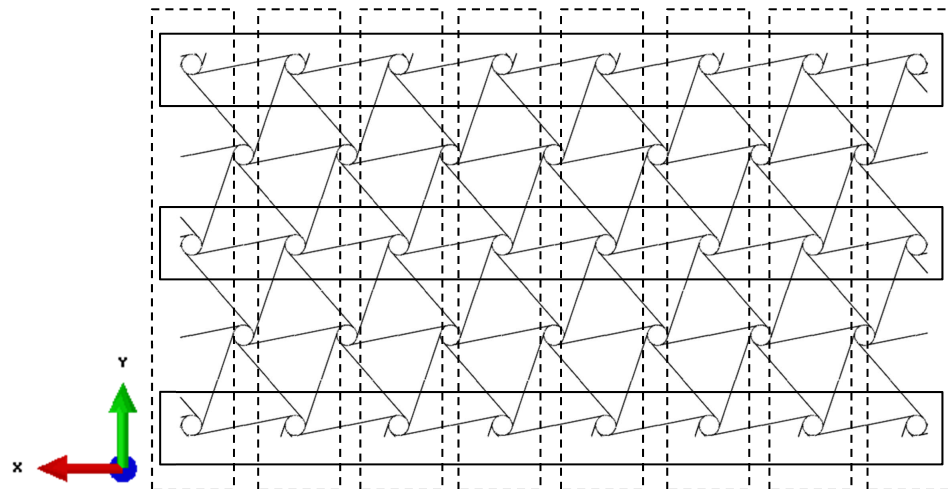


Figure 3.7: Division of the lattice structure in cell units. The sketch shows a lattice with $N = 8$ and $M = 3$. The set of horizontal rectangles represent each of the transversal M divisions while the set of vertical rectangles correspond to each of the N longitudinal divisions.

Furthermore, the internal geometry in the chiral lattices is determined by a number of parameters: the thickness t_{chiral} , the ligament eccentricity e_{chiral} , the ligament half length L_{chiral} , the lattice node depth B_{chiral} and the lattice node radius r_{chiral} . The geometrical meaning of these variables can be seen in Figure 3.8. The thickness t_{chiral} applies for both the ligaments and the lattice nodes geometries. The eccentricity e_{chiral} is expressed as the dimensionless parameter $\varepsilon_{\text{chiral}}$ which is obtained from $\varepsilon_{\text{chiral}} = e_{\text{chiral}}/B_{\text{chiral}}$.

In the sketch shown in Figure 3.8 an additional dimension variable appears, the ligament eccentricity radius R_{chiral} which is dependent on the ligament eccentricity e_{chiral} and the lattice node depth B_{chiral} as shown in Equation 3.13.

A summary of all the parameters introduced to characterize the chiral lattice structure together with their units and nominal values is shown in Table 3.1.

$$R = \frac{e_{\text{chiral}}^2 + \frac{B_{\text{chiral}}^2}{4}}{2e_{\text{chiral}}} \quad (3.13)$$

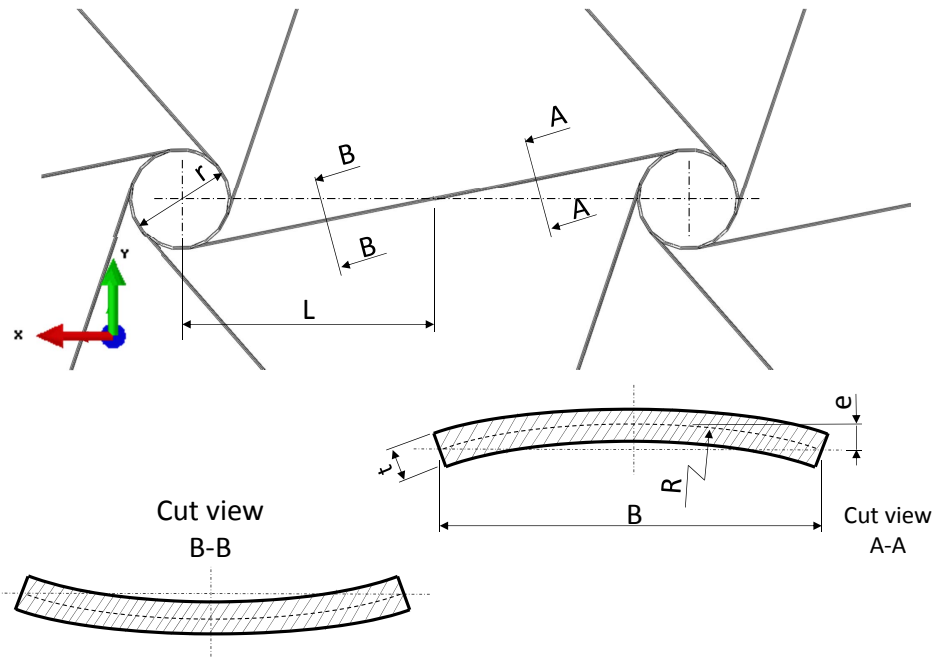


Figure 3.8: Internal parameters of the chiral lattice structure. The geometry is characterized by the the ligament eccentricity e_{chiral} , the ligament half length L_{chiral} , the lattice node depth B_{chiral} , the lattice node radius r_{chiral} and the thickness t_{chiral} . The ligament eccentricity radius R_{chiral} which is dependent on the ligament eccentricity e_{chiral} and the lattice node depth B_{chiral} , as shown in Equation 3.13

Parameter	Symbol	Units	Nominal value
Dimensions			
Number of unit cells in spanwise direction	N		8
Number of unit cells in transversal direction	M		3
Dimensionless ligament eccentricity (e/B)	$\varepsilon_{\text{chiral}}$		0.01
Node radius	r_{chiral}	mm	10
Node depth	B_{chiral}	mm	20
Ligament eccentricity radius	R_{chiral}	mm	250.1
Ligament half length	L_{chiral}	mm	50
Thickness	t_{chiral}	mm	0.5
Material (ABS)			
Young's modulus	E_{chiral}	N/mm ²	3100
Poisson's ratio	ν_{chiral}		0.3

Table 3.1: Parameters used for the lattice model. The mechanical properties of the material used correspond to ABS, which is a common thermoplastic polymer.

Lattice nodes rigid body modeling

The lattice nodes is one of the essential parts of the lattice of chiral elements. These are only constrained in rotation around its own axis by the ligaments connected to them. For the modeling, they are assumed to behave like a rigid body. In Figure 3.9, a closer look to the chiral nodes can be seen, showing two different approaches to manufacture a node that would behave like a rigid body compared with the rest of the structure.

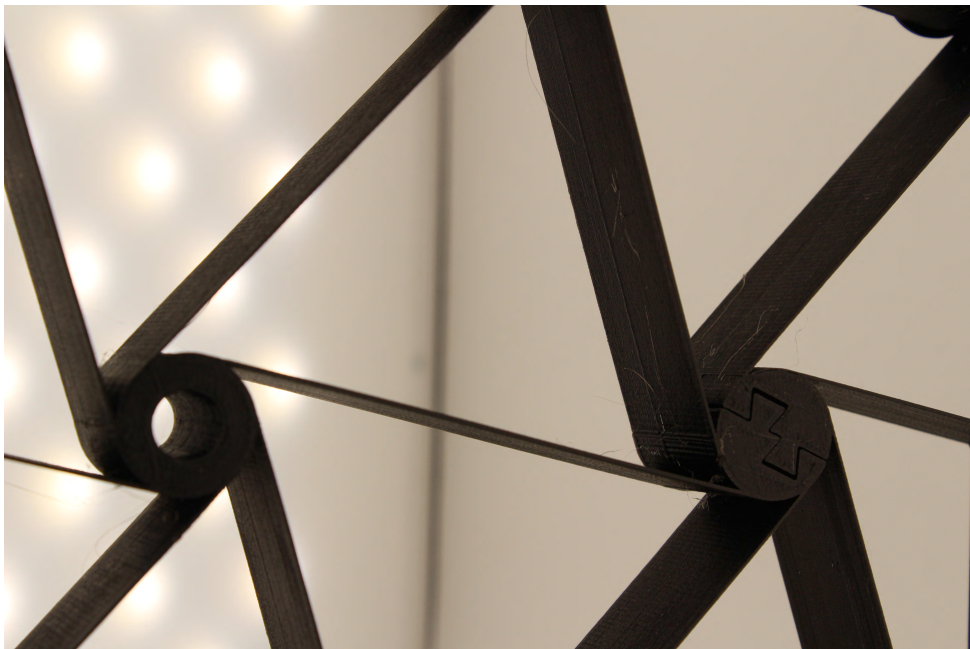


Figure 3.9: Picture of the manufactured chiral lattice nodes. The figure shows two different approaches followed to manufacture the nodes. The one on the right was the standard one showing a cylinder with a thickness bigger than the thickness of the chiral ligaments $t_{\text{node}} \gg t_{\text{ligaments}}$. On the left, an alternative approach is followed in order to allow the assembly of the chiral lattice that is not manufactured as a unique piece. The photography was taken from the demonstrator built by [38].

In the Abaqus model, different approaches were followed to model the chiral nodes together its rigid body feature. The first one was to create a coupling condition using Abaqus corresponding module. In particular, a kinematic coupling was enabled. A kinematic coupling constrains the motion of one or more coupling nodes, also called slave node or nodes, to the rigid body motion of a reference node, also called master node. They are imposed by eliminating degrees of freedom at the coupling nodes. In Figure 3.10, an example of a kinematic coupling can be seen.

For the considered case, the coupling nodes are those mesh nodes located faces of the lattice node and the master node is the reference point located in the center of the lattice node. In order to achieve the rigid solid behavior, all the degrees of freedom were coupled except from the translation displacements in the plane where the chiral lattice is contained, i.e. the translational displacement U_1 and U_2 of the

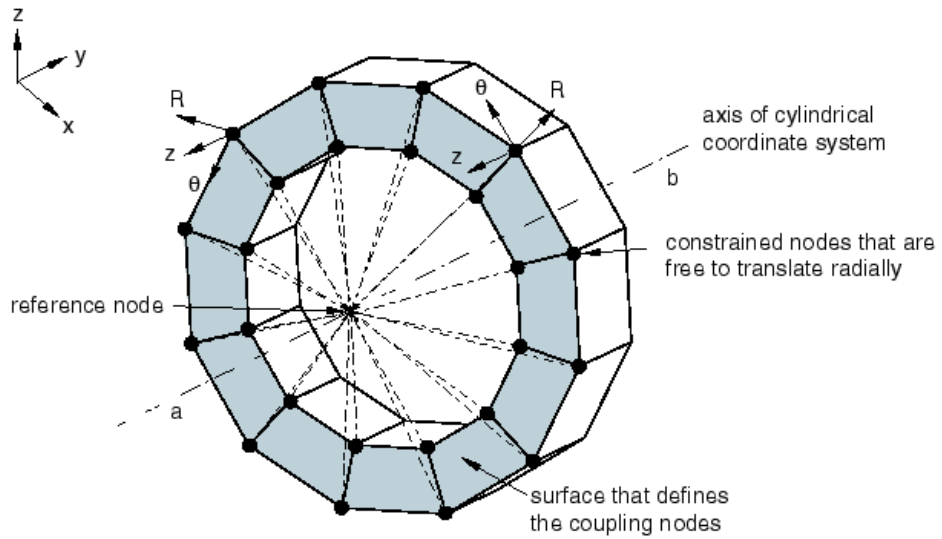


Figure 3.10: Kinematic coupling constraint. The sketch illustrates the use of a kinematic coupling constraint to prescribe a twisting motion to a model without constraining the radial motion. In this case, a local cylindrical reference system is used and the constrained nodes have two degrees of freedom coupled to those of the reference node, the angular position θ and the position along the z axis. The coupling nodes are therefore free to translate radially, varying R . [39]

plane $X - Y$. In Figure 3.11 an overview of this coupling condition can be viewed.

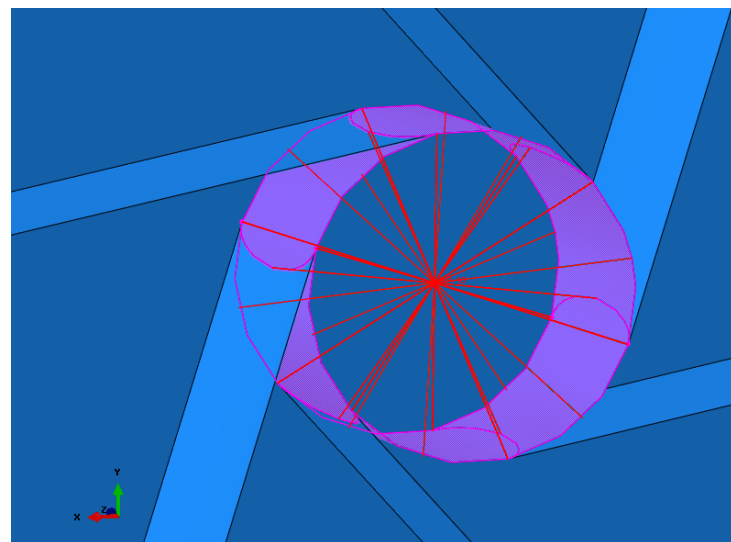


Figure 3.11: Overview of the elements that are involved in the coupling condition at the lattice nodes. The coupling condition was defined in between the mesh nodes located in the faces of the lattice node and a reference point located in the middle. All the degrees of freedom translational and rotational were linked.

Another approach consisted in embedding an additional part inside the lattice nodes to add rigidity to the element. The proposed design of such a part, which is referred as tyre from now on, can be seen in Figure 3.12. The internal dimensions of this element are shown in Figure 3.13. This dimensions were dependent on parameters of the chiral lattice, that is, the thickness of the tyre was equal to that of the chiral lattice $r_{\text{tyre}} = r_{\text{chiral}}$ and the same occurred for the height B_{tyre} and the radius r_{tyre} which were $r_{\text{tyre}} = r_{\text{chiral}}$ and $B_{\text{tyre}} = B_{\text{chiral}}$. The added rigidity was obtained as a result of considering a different material for the tyre such that the Young's modulus of the two parts verify the condition $E_{\text{tyre}} \gg E_{\text{chiral}}$. Once, the connection was completed, the resulting merged part looked as shown in Figure 3.14.

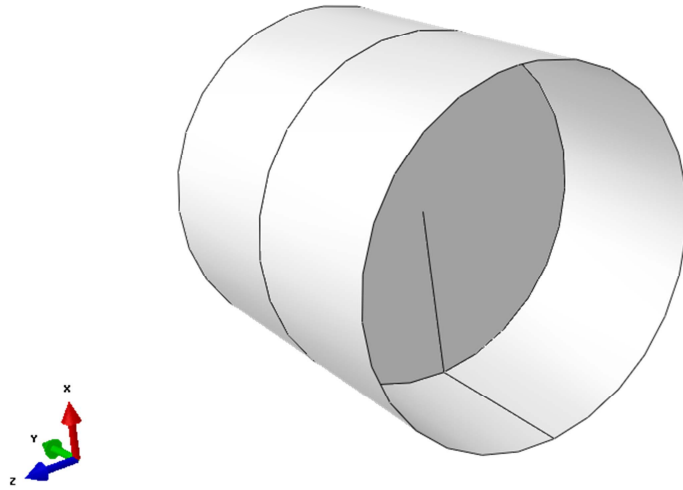


Figure 3.12: Overview of the tyre part.

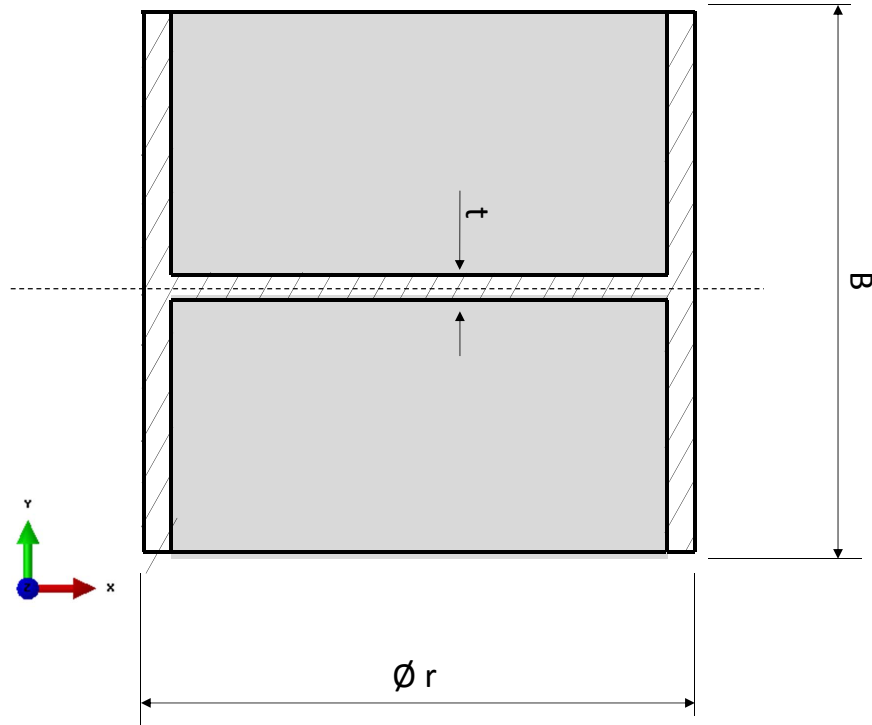


Figure 3.13: Internal parameters of the tyre part. The sketch shows a transversal cut to the part. The tyre is characterized by the radius r_{tyre} , the height B_{tyre} and the thickness t_{tyre} . All this parameters were equal to the corresponding ones in the lattice nodes, therefore: $r_{\text{tyre}} = r_{\text{chiral}}$, $B_{\text{tyre}} = B_{\text{chiral}}$ and $t_{\text{tyre}} = t_{\text{chiral}}$.

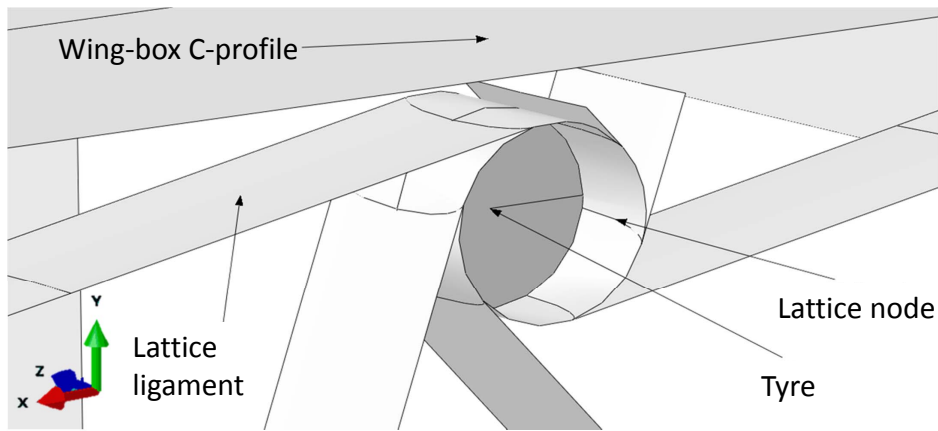


Figure 3.14: Overview of the connection between tyre and lattice node. The tyre will be embed inside the lattice node.

Wing-box in C-profile

The model of the wing-box consisted on a beam with open C profile. The length L_{box} and height H_{box} of the part were determined from those of the lattice of chiral elements. Therefore, the tailorable parameters for this part are the width W_{box} , the thickness t_{box} and the mechanical properties E_{box} and ν_{box} of the material used.

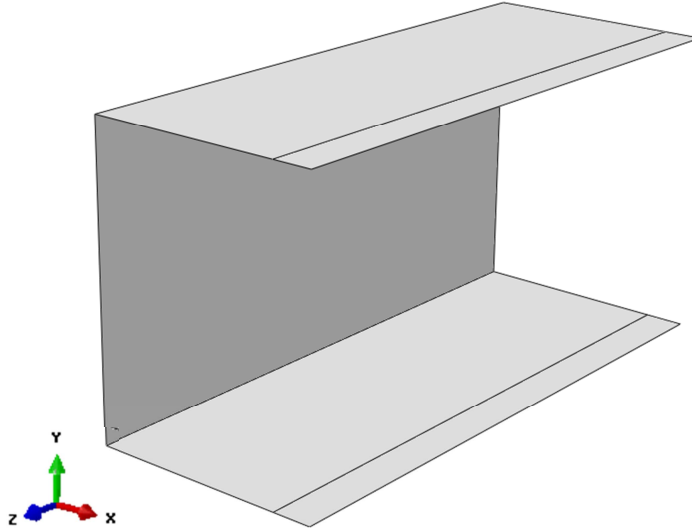


Figure 3.15: Overview of the wing-box in C-profile part

In the sketch shown in Figure 3.16 it is possible see the geometrical meaning of the parameters introduced in the previous paragraph. Additionally, the Table 3.2 shows its units and nominal values.

Parameter	Symbol	Units	Nominal value
Dimensions			
Wing-box height	H_{box}	mm	383.27
Wing-box length	L_{box}	mm	743.86
Wing-box width	W_{box}	mm	300
Wing-box thickness	t_{box}	mm	0.8
Material (Aluminum)			
Young's modulus	E_{box}	N/mm ²	69000
Poisson's ratio	ν_{box}		0.3269

Table 3.2: Parameters used for the wing-box in C-profile model. The mechanical properties of the material used correspond to standard aluminum. The value of the wing-box height H_{box} and the wing-box length L_{box} are not independent but are calculated based on the transversal and longitudinal dimensions of the chiral lattice structure, respectively.

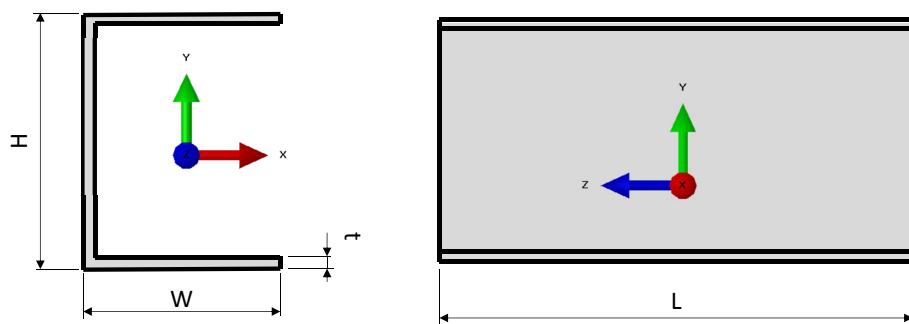


Figure 3.16: Internal parameters of the wing-box C-profile part. The geometry of the part is determined by the length L_{box} , height H_{box} and the width W_{box} . Additionally, the thickness t_{box} is measured in the z direction.

Ribs

In order to provide the wing-box with additional stiffness in the transversal direction, the addition of ribs is considered. For its design, two different approaches are studied. One considers an rib with open profile while the other considers a close profile, as shown in Figure 3.17. These could be installed at the tip and/or root of the wing box; and also, in the interior of the wing-box. For those ribs located in this last position, the open section design is preferred to avoid interferences with the lattice of chiral structures. For the ribs located in an outer position, considerations regarding the optimal design choice will be done in Subsection 4.2.3.

The ribs design is characterized by the widths $W_{\text{rib},\text{close}}$ and $W_{\text{rib},\text{open}}$, and the height H_{rib} . The height H_{rib} and the width of the closed section design $W_{\text{rib},\text{close}}$ are set to be equal to those of the wing-box $H_{\text{rib}} = H_{\text{box}}$. The value of $W_{\text{rib},\text{open}}$ is calculated as follows:

$$W_{\text{rib},\text{open}} = B_{\text{chiral}} + W_{\text{rib},\text{close}} + d_{\text{chiral-rib}}$$

where $d_{\text{chiral-rib}}$ represents the gap between the right edges of the inner rib and the lattice chiral structure. This gap ensures that there are not any interferences in between the rib and the lattice chiral structure. The value of this parameter was set to a fix value of $d_{\text{chiral-rib}} = 20\text{mm}$. Additionally, the frame with A_{rib} and the thickness t_{rib} allowed design modifications.

The nominal values of all the parameters involved in the ribs design can be read in Table 3.3. The material choice aimed for a configuration stiffer than the wing-box to ensure no out-of-plane deformation of the rib. For this reason, the material chosen is steel.

Parameter	Symbol	Units	Nominal value
Dimensions			
Rib height	H_{rib}	mm	383.27
Closed rib width	$W_{\text{rib},\text{close}}$	mm	300
Frame width	A_{rib}	mm	30
Rib thickness	t_{rib}	mm	2
Material (Steel)			
Young's modulus	E_{rib}	N/mm ²	200000
Poisson's ratio	ν_{rib}		0.25

Table 3.3: Parameters used for the ribs model. The material of choice is steel. The value of the rib width $W_{\text{rib},\text{close}}$ and the height H_{rib} will be equal to the wing-box width W_{box} and to the chiral lattice structure height, respectively.

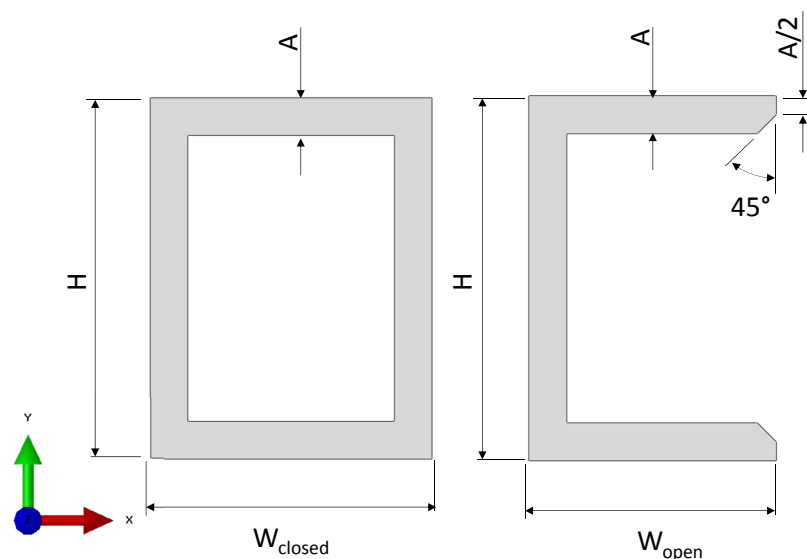


Figure 3.17: Internal parameters of the two different ribs parts. The angle edge for the open section configuration is set to a fix value of 45° to simplify the design and assuming this area of the rib is not critical for the rib duty.

3.3.2 Computational model mesh characteristics

In the present section, the characteristics of the model spatial discretization are presented. The mesh is unstructured and it is auto-generated by Abaqus CAE for the whole assembly. The elements were a combination of quadratic and tetrahedral with 4 and 3 nodes, respectively. Different mesh elements size were assigned to different parts of the model depending of the geometrical complexity of the area.

In Figure 3.18, it is possible to distinguish two regions that assigned with different mesh element size: the lattice of chiral structures and the close region of the wing-box skin are assigned with a fine mesh size while the remaining model is assigned with a course mesh, typically one order of magnitude greater. This introduces two new parameters that are used to modify the mesh size of the different regions:

- S_f : Fine mesh size, typically equal to 3 mm.
- S_c : Course mesh size, typically equal to 30 mm

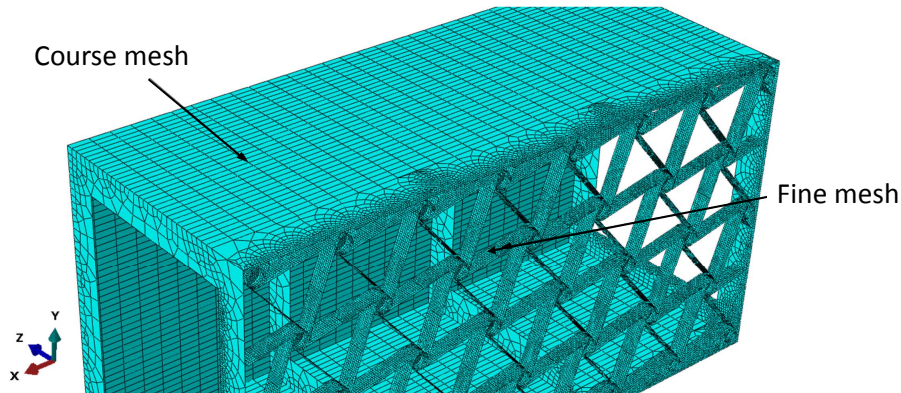


Figure 3.18: Internal parameters of the two different ribs parts. Different mesh element size are assigned to different parts of the model. The lattice structure is assigned with a fine mesh element size while the wing-box is assigned with a course mesh element size.

3.3.3 Load definition

3.3.4 Boundary condition

The boundary condition was the one shown in Figure 3.19. It consisted in a kinematic coupling similar to the one introduced in Section 3.3.1 to model the rigid body behavior of the lattice nodes. In this case, the kinematic coupling is established between a reference point located approximately at the centre of the root rib and the faces of this mentioned rib. The reference point acts as a master node while the mesh nodes located at the faces of the rib are the slave nodes. The reference point is next fixed in all its degrees of freedom using the corresponding boundary condition Abaqus module.

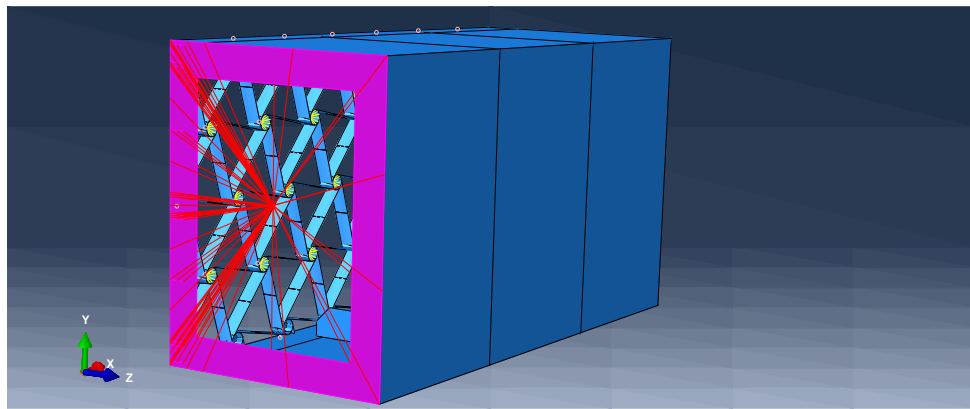


Figure 3.19: Boundary condition for the model. The condition is established through a coupling interaction between a reference point and the faces of the rib at the root. The reference point is fixed in all its degrees of freedom using the corresponding boundary condition Abaqus module.

3.3.5 Post-processing operations

The results obtained from the Abaqus simulations were analyzed in two different ways. Firstly, qualitatively by means of the deformation plots that shown by the Abaqus. And, secondly, extracting values of different magnitudes directly from the mesh nodes or elements located at certain positions of interest.

Through the definition of paths in Abaqus, it is possible to obtain the value of a determined magnitude for all the mesh elements located along the path. In Figure 3.20, an example of a path located on the upper skin of the wing-box is shown.

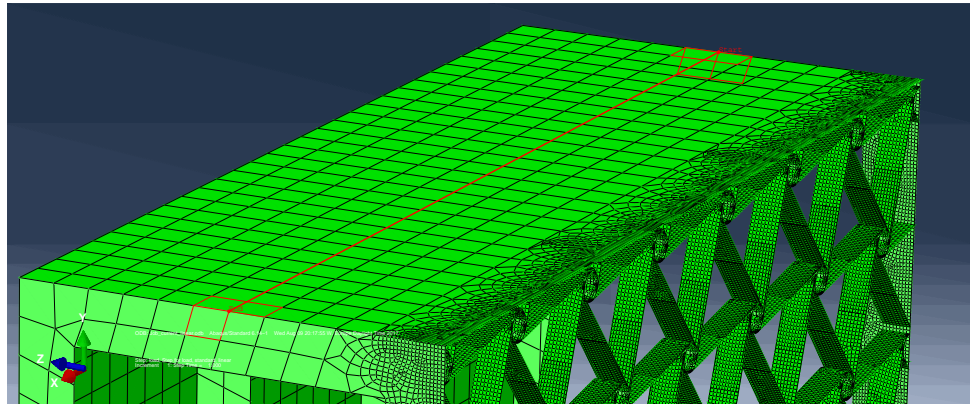


Figure 3.20: Path of mesh elements on the solution model.

3.3.6 Connection between the wing-box skin and the chiral lattice

In the present subsection, the computational modeling of the connection between the lattice nodes and the wing-box skin is presented. This is an unavoidable transition from the lattice of chiral structures comprised of nodes and ligaments to the skin of the wing-box. Loads are transmitted to the lattice through this attachment points that is why its design results crucial. Three different configurations are studied:

Blocked translation and rotation The lattice nodes have all its degrees of freedom restrained

Blocked translation and free rotation The lattice nodes are only restraint in the rotation around its own axis by the ligaments. The translation displacement parallel to the skin is restrained. An sketch showing this connection can be viewed in Figure 3.22. This configuration was the one chosen for the demonstrator built in the Figure 3.21.

Free translation and rotation Now the lattice nodes are also allowed to translate parallel to the skin. This configuration is schematically represented in Figure 3.23.



Figure 3.21: Detail of the connection between the lattice nodes and the skin. The picture shows the type of connection chosen for the manufactured demonstrator of the lattice. The lattice nodes is allowed to rotate around its own axis but cannot translate parallel to the skin. This photography was taken from the demonstrator built by [38].

In the computational model the lattice of chiral elements and the skin of the wing-box are not physical connected by any element. It becomes necessary to use the interaction module provided by Abaqus CAE to model the connections. Two different approaches are studied to achieve this modeling task. These are presented below.

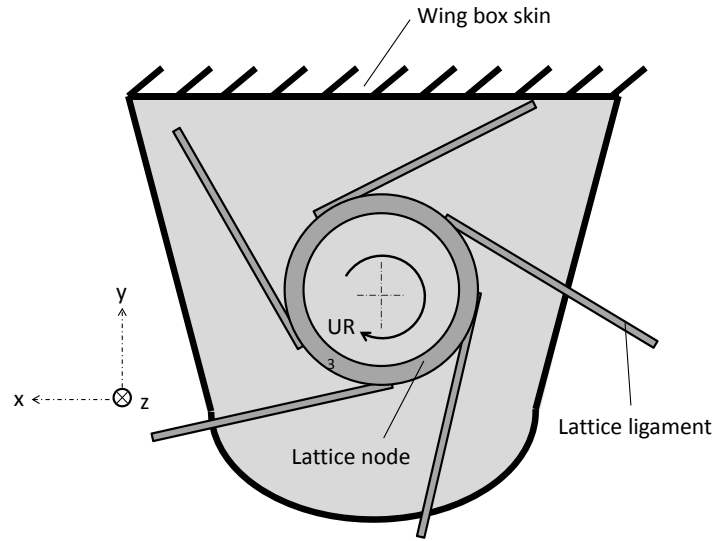


Figure 3.22: Blocked translation and free rotation connection between the lattice nodes and the skin. In this case, the only degree of freedom of the lattice node that it is not restrained the rotation around its own axis, that is the rotation UR_3 around the direction z .

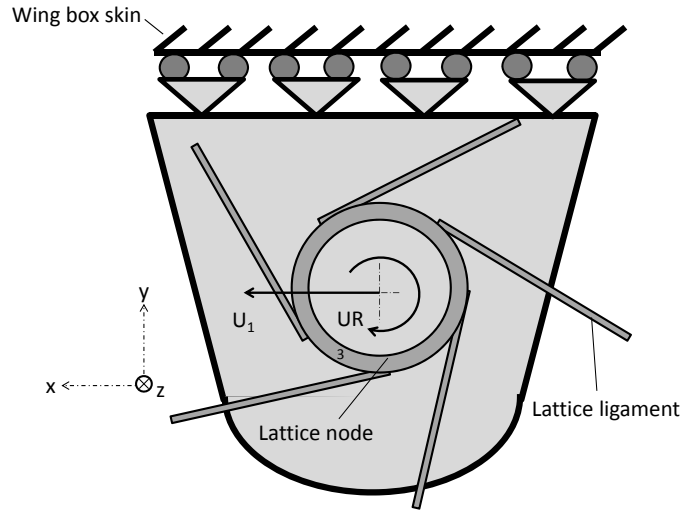


Figure 3.23: Free translation and rotation connection between the lattice nodes and the skin. For this case, the unrestrained degrees of freedom of the lattice nodes are the rotation the rotation UR_3 around its own axis, i.e.: the direction z ; and the displacement U_1 parallel to the wing-box wall, i.e.: along the direction x .

Coupling through tyre part

This approach consists in using the tyre part that was described in Subsection 3.3.1. At each of the lattice nodes located at the border of the lattice structure, a tyre part is created and embed into the lattice node, as it is shown in Figure 3.14. Then, a coupling constraint is establish between a mesh node in the middle of the tyre and a mesh node located on the wing-box skin just above the tyre, as shown in Figure 3.24.

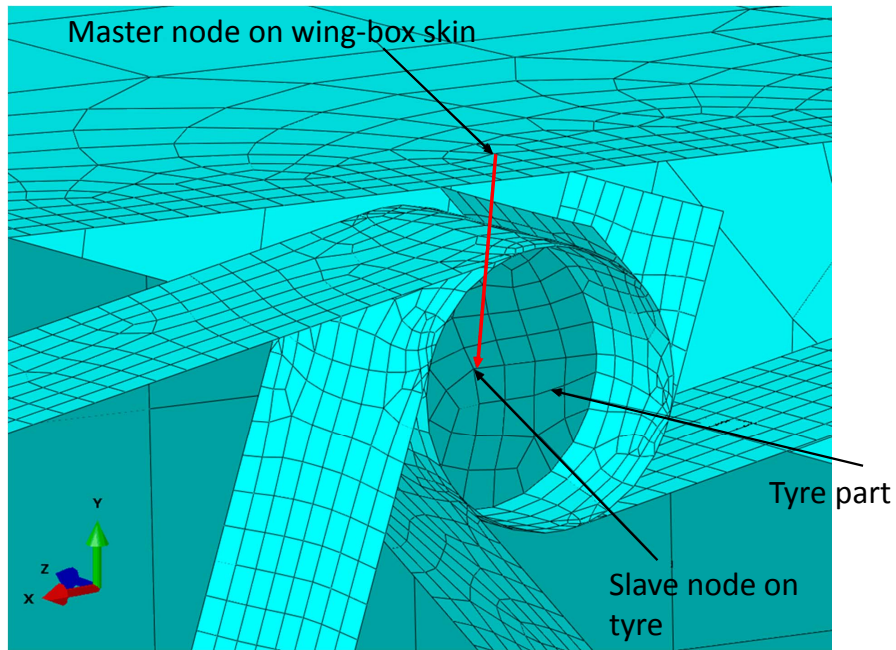


Figure 3.24: Coupling condition between the lattice node and the wing-box skin through tyre. The coupling condition is establish between a mesh node located in the wing-box skin that acts as a master node and a mesh node in the middle of the tyre that becomes the coupling node.

Depending on the type of connection considered, different degrees of freedom are coupled. For the most restrictive case, in which the connection between the lattice structure and the wing-box is rigid, not allowing any translational or rotational displacement, the six degrees of freedom are coupled between the mesh nodes mentioned on the previous paragraph.

For the other connection types, rotation of the lattice node is allowed around its own axis. This allowance is implemented by not constraining the rotational displacement w around the z direction in the coupling constraint definition. Finally, the last connection type introduced at the beginning of the present subsection allowed the displacement of the lattice node parallel to the wing-box skin. For this case, the translational displacement u along the x direction is be left uncoupled.

The rigid body motion imposed to the mesh node located at the center of the tyre is translated to the mesh nodes located in the faces of the lattice node because they are physically connected.

Coupling through local cylindrical reference system

In this case, the rigid body feature provided by the tyre installation is replaced by an additional coupling condition created in a local cylindrical reference system located at each of the lattice nodes. This new reference system substitutes the global Cartesian coordinates system and its origin is a reference point located in the centre of the lattice node, at $z = B/2\text{mm}$. The position of a point in the lattice node face will be determined by the radial distance r to the origin, the angular position θ and the position z along the lattice node rotation axis. A sketch of this reference system is shown in Figure 3.25.

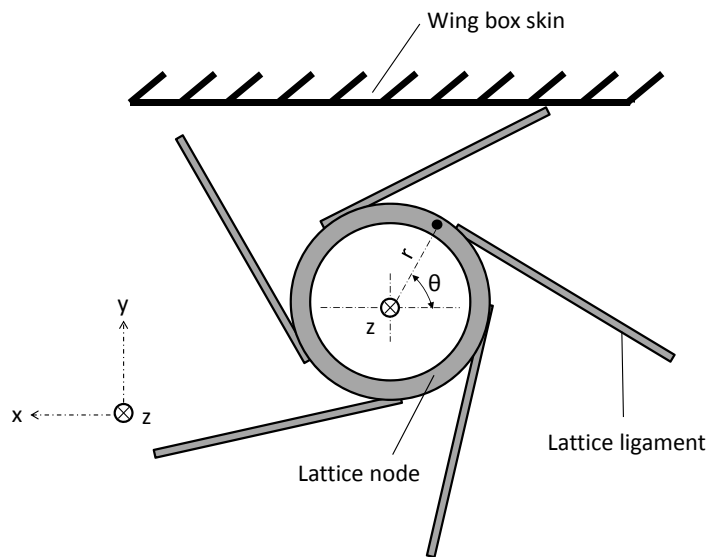


Figure 3.25: Local reference system at the lattice nodes. The position of point in the lattice node faces will be determined by the radial distance r to the origin, the angular position θ and the position z along the node rotation axis.

In the mentioned local reference system, a kinematic coupling constrain links the rigid body motion in r and z of a reference point located in the centre of the lattice node to those of a set of mesh nodes located on the lattice node faces. In the coupling definition, the reference point is the master node and the mesh nodes found in the faces of the lattice node are the slave nodes. This condition is visualized in Abaqus as shown in Figure 3.26.

Then, an additional coupling constrain is necessary to be establish in between the reference node that acts as the origin of the local cylindrical reference system and the wing-box skin. This is the same one that was previously establish when using a tyre part and shown in Figure 3.24. The only difference is that for this case the slave node is the reference point instead of a mesh node located in the center of the tyre.

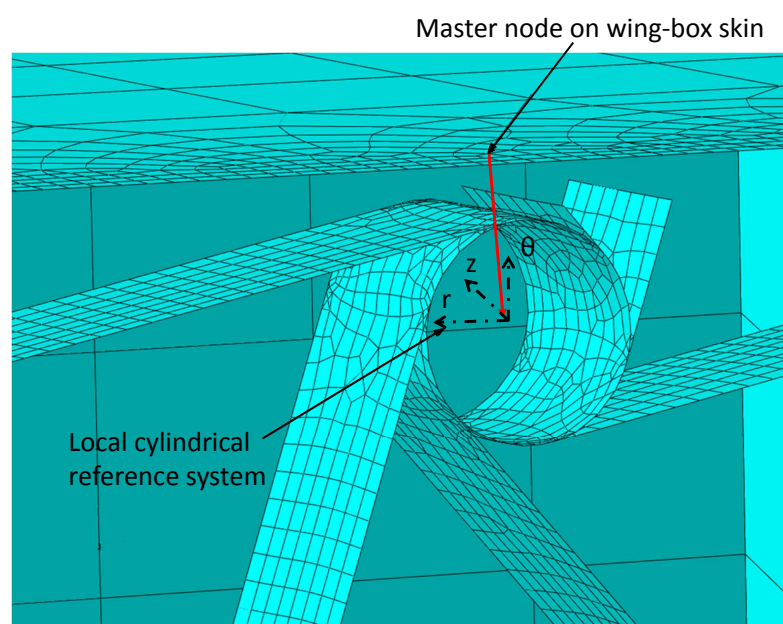


Figure 3.26: Coupling condition between the lattice node and the wing-box skin through a local reference system.

3.3.7 Parametric study method

The model described in the previous subsections is implemented in a Python program that is read by the FEM software, Abaqus CAE. The program is fully parametrized and this enables the possibility of executing simulations for different values of the parameters introduced previously. The parametric study program is executed when calling the python file `mainAbaqusParametricStudy.py`. As part of the execution of this file, a computational model is built, submitted for analysis and post-processed by the complementary program `mainBuildAndExecuteWingBox.py`, for all the different values of the parameters that form part of the parametric study defined in the file `setUpParametricStudy.py`. The convergence of the simulation is controlled within the program `mainAbaqusParametricStudy.py` and it is able to re-run a simulation with slight variations in the mesh size and/or in artificial dissipation definition if convergence was not achieved.

An schematic characterization of the program execution is shown the flow chart represented in Figure 3.27. The code written for this program can be found in Appendix A.

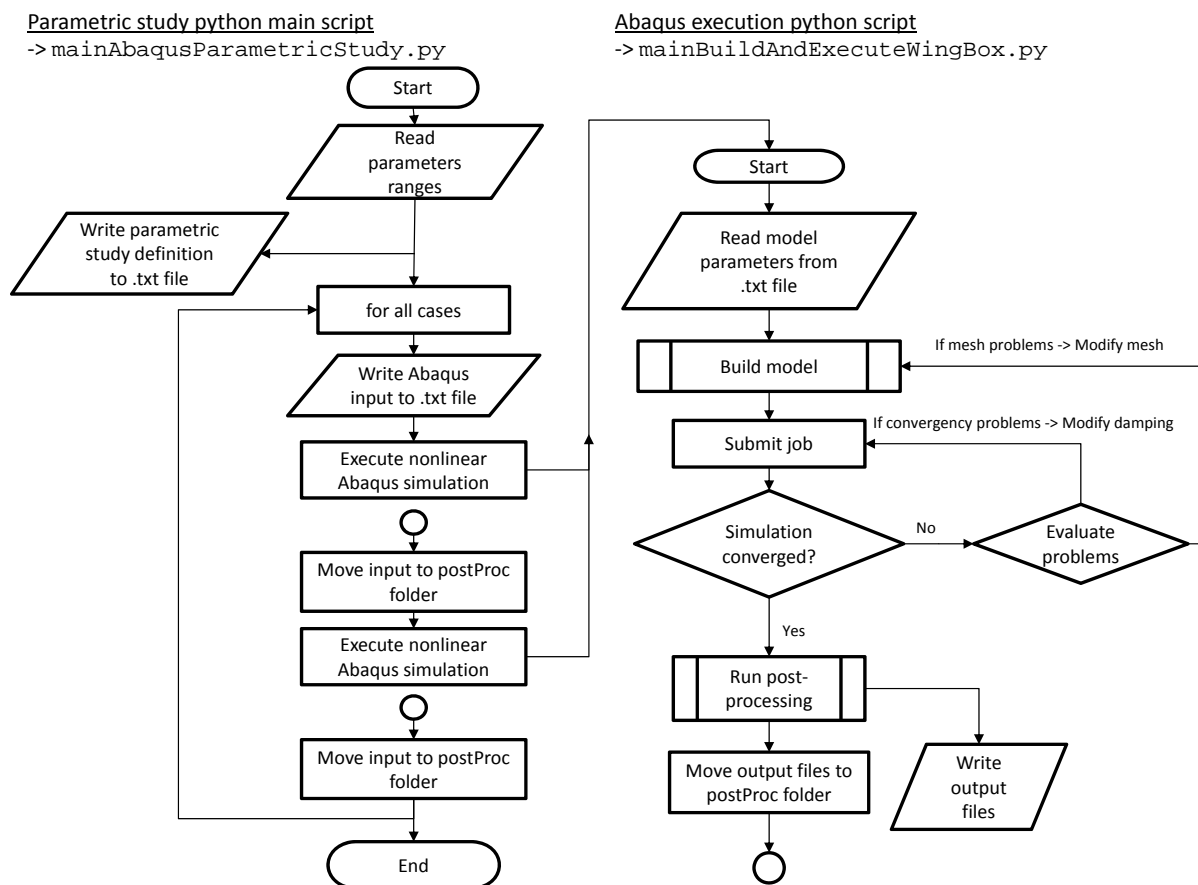


Figure 3.27: Flow chart showing the execution of the parametric study python code.

Chapter 4

Model analysis

In the present chapter the general characterization of the model is presented. The first section include an analysis of the analytical model. For this, a variation of the beam geometric parameters and the stiffness ratio E_1/E_2 between the adaptive web and the rest of the model is performed. Firstly, the predicted evolution of the bending-twist coupling as a function of the stiffness ratio E_1/E_2 is presented. Secondly, the results obtained from the parametric study performed are introduced. This will provide insight of how the different design parameters affect the final mechanical properties of the beam.

In the second section, the computational model is analyzed in order to obtain the most suitable configuration to show the response expected from the concept proposed. In particular, a discussions over the methods to model the connection between the chiral lattice and the wing-box, the load introduction method, the mesh particularities, the ribs inclusion and the nonlinearities the response are presented.

4.1 Analytical model analysis

The analytical model of the wing-box was already presented in the Section 3.2. For the results that are presented in the subsections below, the parameters already defined in the mentioned section are assigned to the nominal values presented in Table 4.1. These are taken from a similar analytical approach to the problem of a wing-box with a variable-stiffness web, presented in [17]. By doing this, verification of the results becomes possible.

Parameter	Symbol	Units	Nominal value
Dimensions			
Height of the cross section	H	mm	200
Wing-box length	L	mm	800
Width of the cross section	B	mm	80
Wing-box wall thickness	t_1, t_2	mm	1
Material (Aluminum)			
Young's modulus	E_1, E_2	N/mm ²	69000
Shear modulus	G_1, G_2	N/mm ²	26000

Table 4.1: Nominal value of the parameters used for the analytical model. The mechanical properties of the material used correspond to standard aluminum.

4.1.1 Bending and twisting coupling results and discussion

Here, the influence of the stiffness ratio E_1/E_2 on the coupling between the bending and the twist deformations of the beam is presented. This is graphically shown in Figure 4.1 for a number of simulations performed for a load Q_z equal to 2000 N. In the plot, the twist variation is shown with the solid line and it is represented using the variable ϕ_{tip}/Q while the bend is shown with the dashed line and it is also represented as w_{tip}/Q .

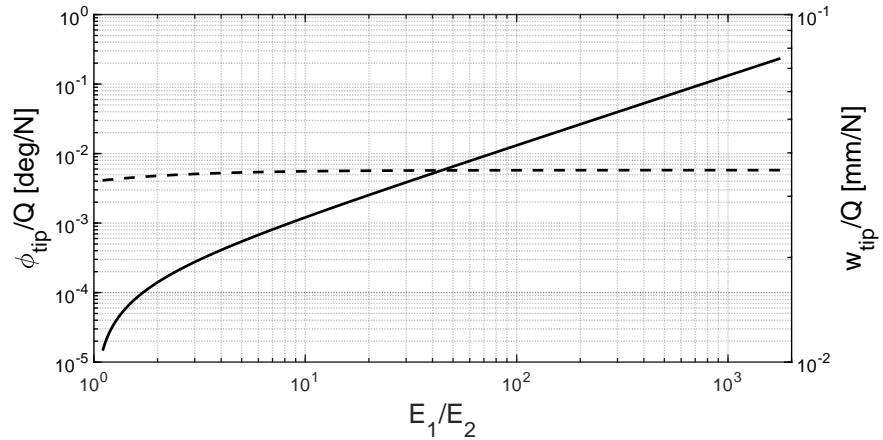


Figure 4.1: Influence of the stiffness ratio E_1/E_2 on the wing-box tip twist ϕ_{tip} and bend w_{tip} . The solid line is used to represent the twist ϕ_{tip} while the dashed line represents the bend w_{tip} . The two displacements are divided by the magnitude of the applied force Q_z .

Results shown in Figure 4.1 describe how the coupling between the twist at the tip of the wing-box ϕ_{tip} and the bend of the wing-box w_{tip} would vary for different values of the stiffness ratio E_1/E_2 . This last parameter is modified over a wide range such that $E_1/E_2 \in [10^0, 10^3]$. The point load Q_z is considered to have a magnitude equal to 2000 N. It can be seen that the variable ϕ_{tip}/Q_z is consequently increased by various orders of magnitude from $\phi_{\text{tip}}/Q_z = 10^{-4}$ deg/N to $\phi_{\text{tip}}/Q_z = 10^{-1}$ deg/N. However the variation in bend represented with the variable w_{tip}/Q_z is negligible in comparison. It can be seen that the bend displacement quickly increases for values of $E_1/E_2 > 1$ and it gets to an asymptote for values $E_1/E_2 \gg 1$. These results therefore show how twist displacement, which gives information regarding the torsional stiffness of the structure, is much more affected by variations of the stiffness ratio E_1/E_2 than the bending stiffness is. Consequently, it is not expected to see large increments in bend displacement in comparison with the twist when the variable-stiffness mechanism is activated. This results are in compliance with those presented in [17].

For the proposed mechanism, it is expected that the ratio E_1/E_2 , which is linked to the effective shear modulus G_{eff} of the real wing-box, is reduced in various orders of magnitude once the buckling is triggered. After this event, the results above show that the bending stiffness of the wing-box reduction will be negligible in comparison with the reduction in torsional stiffness.

4.1.2 Parametric study results and discussion

In the present subsection, the variation of the beam mechanical properties for different geometric parameter values is shown. The beam geometry is characterized through the cross-sectional aspect ratio B/H , the thickness ratio t_2/t_1 and the slenderness ratio L/B . The effect of these parameters on the sectional properties, twist and bending stiffness, and flexural and twisting compliance are shown. Additionally, the variance of the stiffness ratio E_1/E_2 is also included in the analysis.

The influence of the cross-sectional aspect ratio B/H on the torsional stiffness GI_t , the shear centre position y_{SC} and the flexural stiffness EI_y is shown in Figures 4.2, 4.3 and 4.4, respectively. On its side, the effect of thickness ratio t_2/t_1 on the same three beam parameters is shown in Figures 4.5, 4.6 and 4.7.

Additionally, the effect of the cross-sectional aspect ratio B/H on the deflection and torsional compliance is shown on Figures 4.8 and 4.9, respectively. The corresponding plots when analyzing the effect of the thickness ratio t_2/t_1 on the deflection and torsional compliance are shown on Figures 4.10 and 4.11, respectively. The beam's torsional compliance will be expressed as fraction of the twist at the tip divided by the vertical force applied, that is $|\phi_{tip}|/Q$, while the beam deflection compliance will be expressed as fraction of the maximum vertical displacement at the tip divided by the vertical force applied, that is $w_{0,tip}/Q$.

In Figure 4.2, it can be seen that a maximum torsional stiffness appears for $B/H = 1$ when $E_1/E_2 = 1$. This can be explained because, as it is also shown in [17], the closer the torsional stiffness to the doubly symmetric case, the higher its torsional stiffness. However, when $E_1/E_2 > 10$, the maximum torsional stiffness is shown to appear for $B/H > 1$. A similar conclusion can be extract when analyzing the Figure 4.5, that shows the influence of the thickness ratio t_2/t_1 on the torsional stiffness GI_t .

In Figure 4.3 shows that for values $E_2 \ll E_1$, the shear centre position y_{SC} is approximately constant for B/H variations. In this context, the beam approximates its behavior as if it has an open profile section. However, as the value of E_1/E_2 decreases, the influence of the ratio B/H increases showing a bigger influence of the web where the Young's modulus E_2 applies. On the other hand, Figure 4.6 shows that the bigger the thickness ratio t_2/t_1 is, the closer that the shear centre y_{SC} will be to the vertical axis of symmetry. However, for $E_2 \ll E_1$ the influence of the thickness ratio t_2/t_1 is reduced.

The effect of the slenderness ratio L/B on the deflection and torsional compliances is shown in Figures 4.12 and 4.13, respectively.

4.2 Computational model analysis

In the present section, results from the analysis of the computational model are presented. Different aspects of the model are evaluated and design decisions are justified. The analysis is going to consider the mesh influence in the results, the ribs addition and the nonlinearities that appear in the problem.

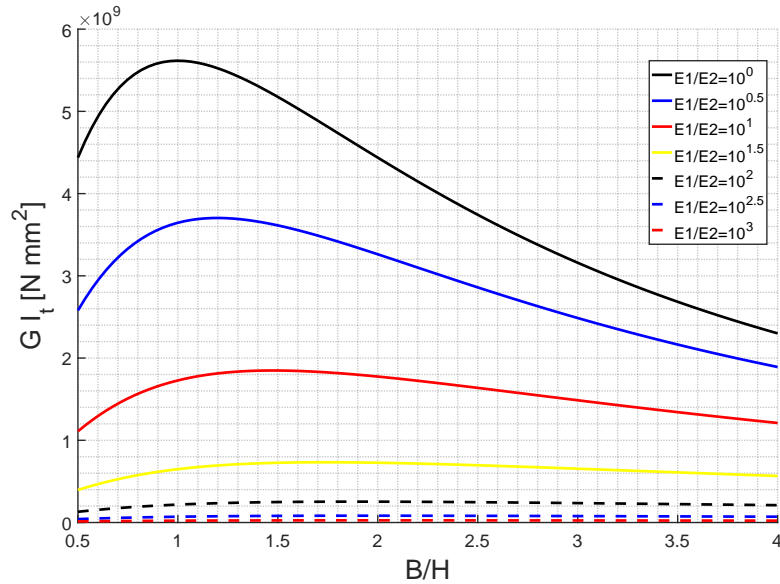


Figure 4.2: Influence of the cross-sectional aspect ratio B/H on the torsional stiffness GI_t , shown for various values of the stiffness ratio E_1/E_2 ranging from 10^0 to 10^3 .

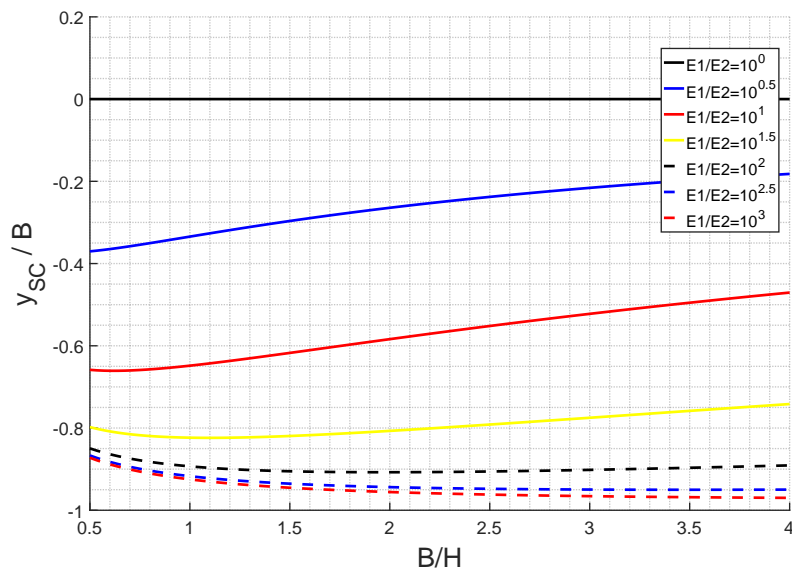


Figure 4.3: Influence of the cross-sectional aspect ratio B/H on the dimensionless shear centre position y_{SC}/B , shown for various values of the stiffness ratio E_1/E_2 ranging from 10^0 to 10^3 .

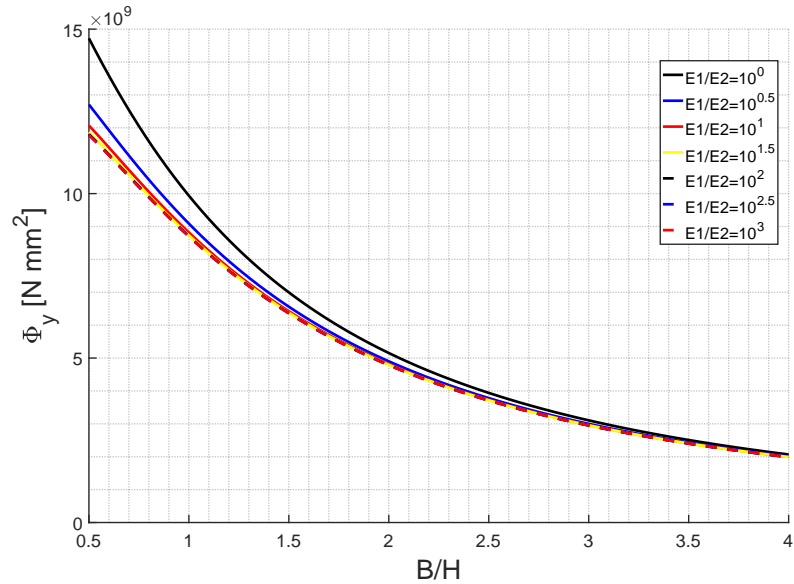


Figure 4.4: Influence of the cross-sectional aspect ratio B/H on the flexural stiffness $EI_y = \Phi_y$, shown for various values of the stiffness ratio E_1/E_2 ranging from 10^0 to 10^3 .

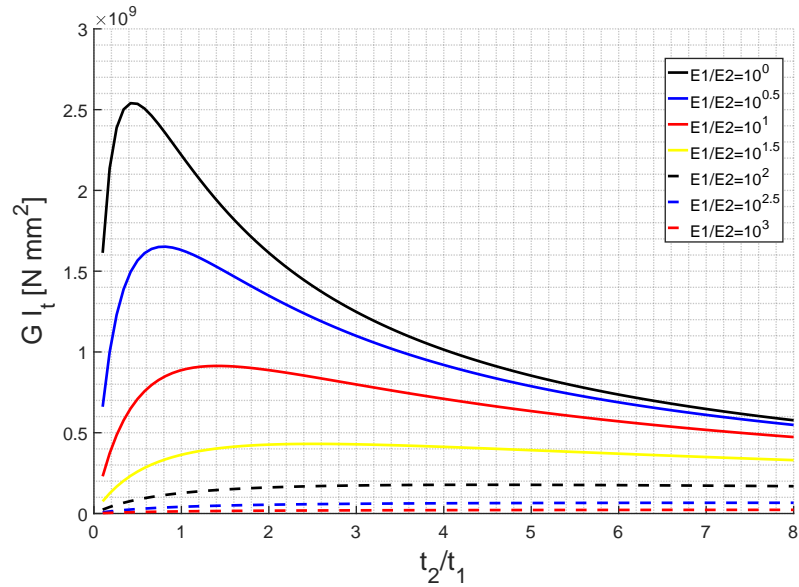


Figure 4.5: Influence of the wall thickness ratio t_2/t_1 on the torsional stiffness GI_t , shown for various values of the stiffness ratio E_1/E_2 ranging from 10^0 to 10^3 .

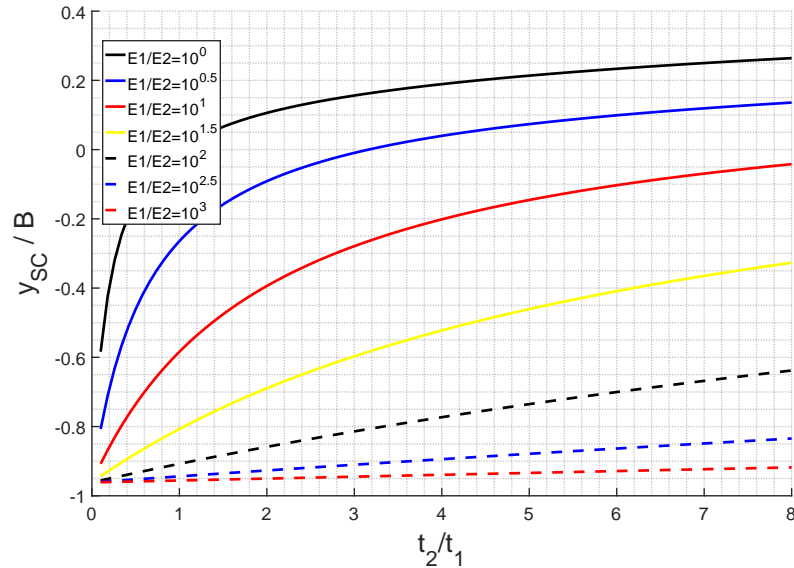


Figure 4.6: Influence of the wall thickness ratio t_2/t_1 on the dimensionless shear centre position y_{SC}/B , shown for various values of the stiffness ratio E_1/E_2 ranging from 10^0 to 10^3 .

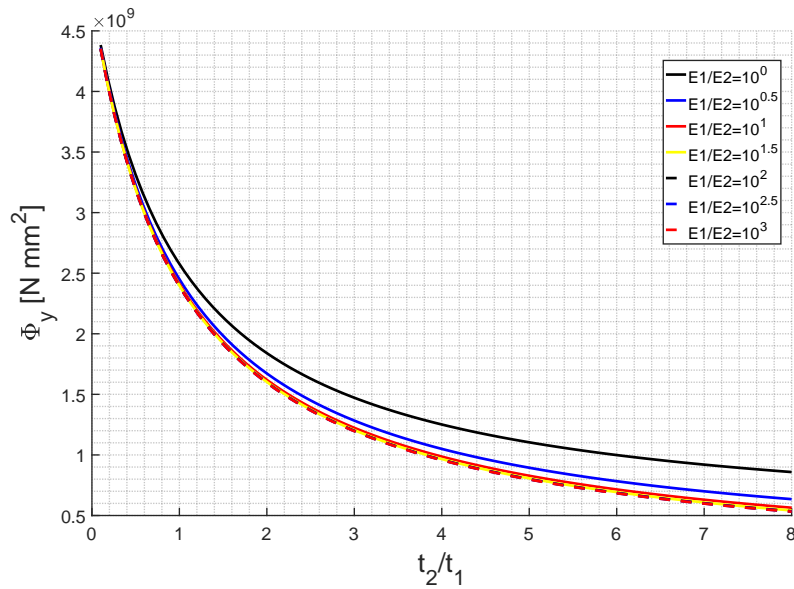


Figure 4.7: Influence of the wall thickness ratio t_2/t_1 on the flexural stiffness $EI_y = \Phi_y$, shown for various values of the stiffness ratio E_1/E_2 ranging from 10^0 to 10^3 .

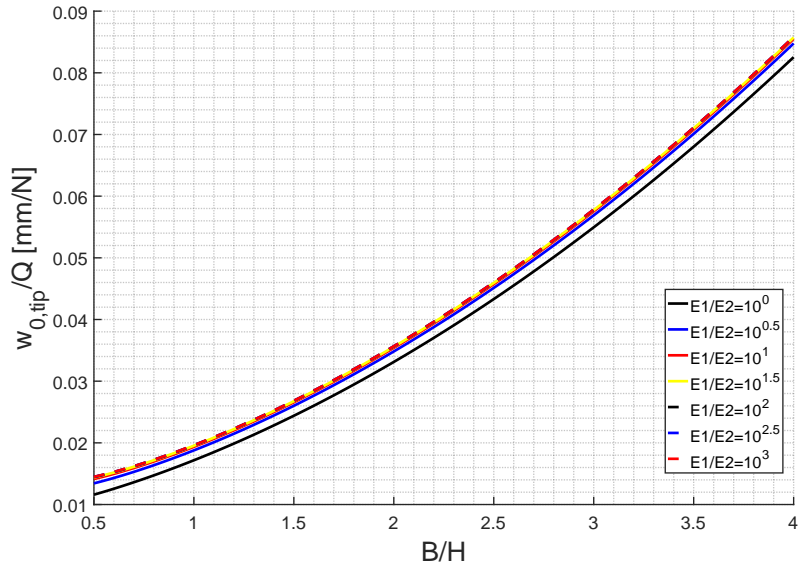


Figure 4.8: Influence of the cross-sectional aspect ratio B/H on the deflection compliance $w_{0,\text{tip}}/Q$, shown for various values of the stiffness ratio E_1/E_2 ranging from 10^0 to 10^3 .

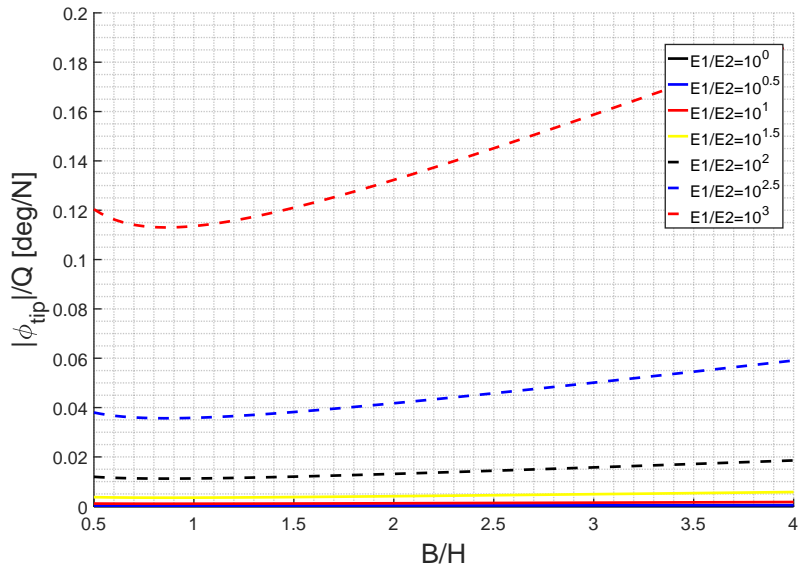


Figure 4.9: Influence of the cross-sectional aspect ratio B/H on the torsional compliance $|\phi_{\text{tip}}|/Q$, shown for various values of the stiffness ratio E_1/E_2 ranging from 10^0 to 10^3 .

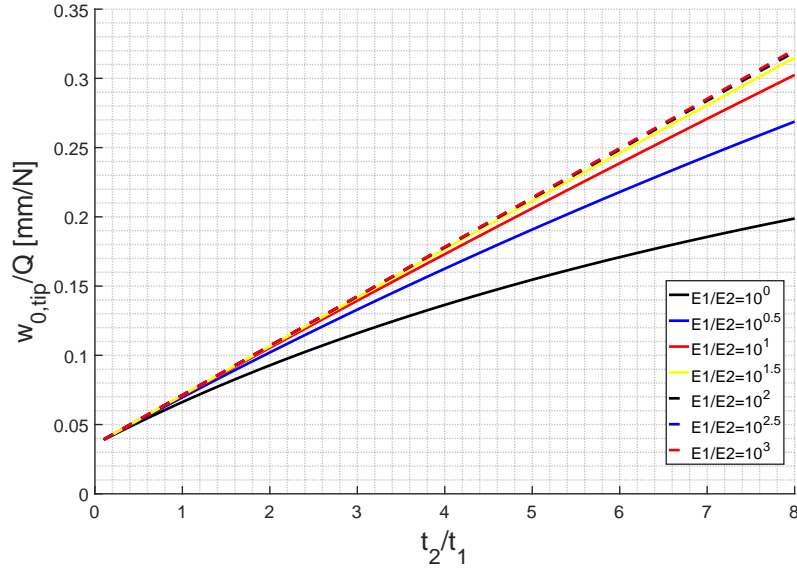


Figure 4.10: Influence of the thickness ratio t_2/t_1 on the deflection compliance $w_{0,\text{tip}}/Q$, shown for various values of the stiffness ratio E_1/E_2 ranging from 10^0 to 10^3 .

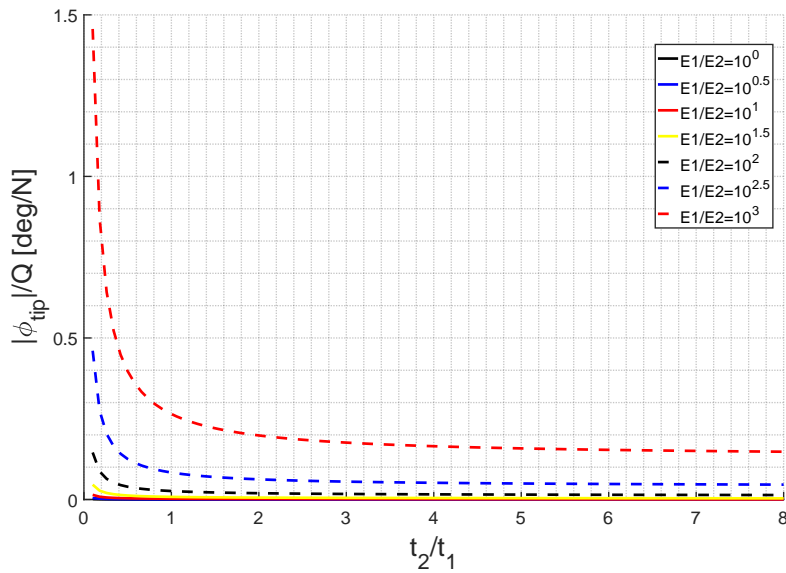


Figure 4.11: Influence of the thickness ratio t_2/t_1 on the torsional compliance $|\phi_{\text{tip}}|/Q$, shown for various values of the stiffness ratio E_1/E_2 ranging from 10^0 to 10^3 .

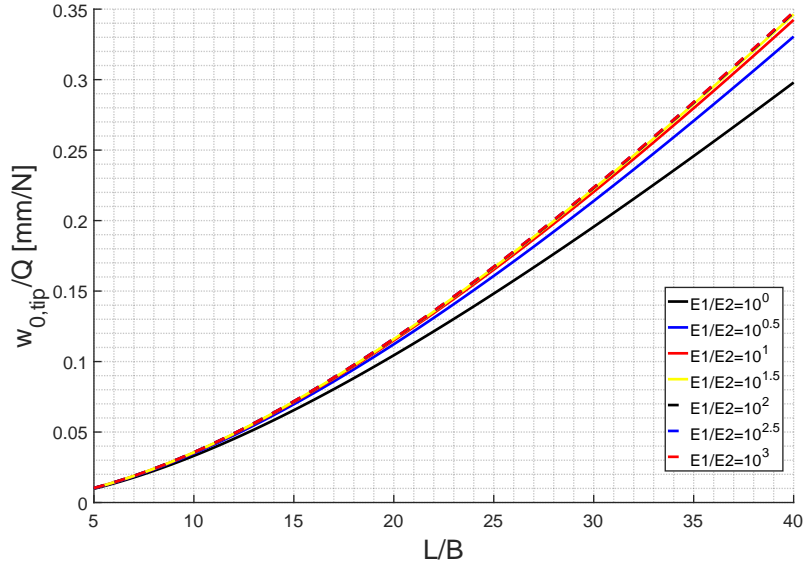


Figure 4.12: Influence of the slenderness ratio L/B on the deflection compliance $w_{0,tip}/Q$, shown for various values of the stiffness ratio E_1/E_2 ranging from 10^0 to 10^3 .

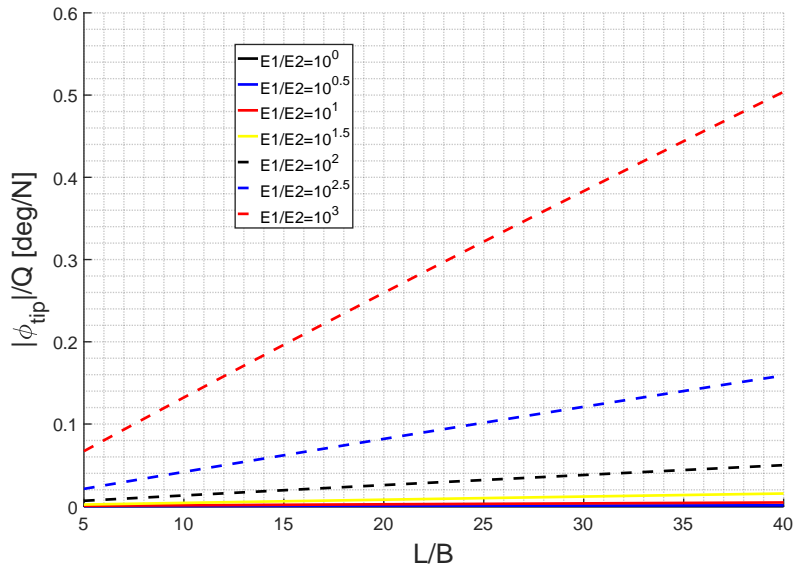


Figure 4.13: Influence of the slenderness ratio L/B on the torsional compliance $|\phi_{tip}|/Q$, shown for various values of the stiffness ratio E_1/E_2 ranging from 10^0 to 10^3 .

4.2.1 Mesh

The model was build using cell shell elements as the fundamental constituting part. The thickness is assigned in the perpendicular direction, as it was shown in Figure 3.5.

This type of element is a 2D element that it was used to build 3D structures. This kind of procedure may incur some distortion in the mesh elements due to shell elements intersecting in the same line at different angles.

For the designed model, this situation occurred at the chiral lattice at certain points. It can be seen in Figure 4.14 that the distorted elements appear at mainly at two different positions. Firstly, at the plane where the two ligaments with different curvature join. At this point, the sharp angles that appear in between the part geometrical lines induce the appearance of tetrahedral distorted mesh elements. The second typical location for appearance of distorted elements is along the curve where the lattice nodes and the curved ligaments join.

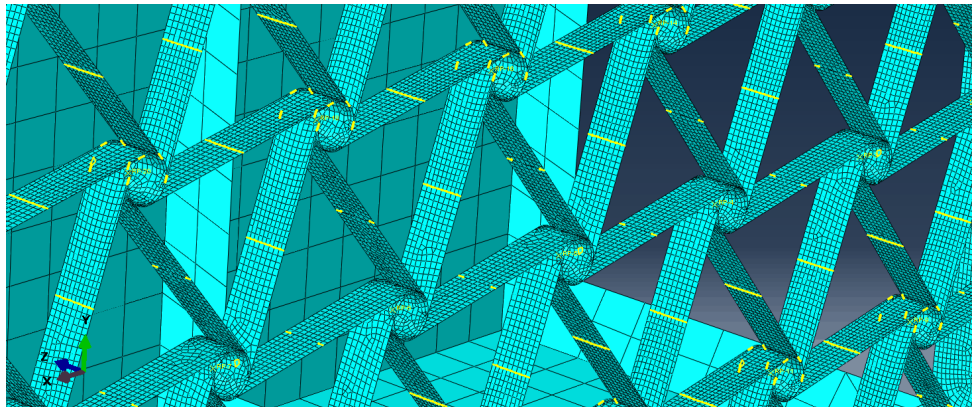


Figure 4.14: Distorted mesh elements in the model. The number of distorted elements was found to be crucial for the simulation convergence.

It was seen that the number of distorted elements had a significant effect in the simulation convergence evolution. For a high number of distorted elements, the simulation could not go further from the first step. No attempts to locally modify the mesh at the mentioned locations were made, instead, it was found that modifying the global mesh size gave enough control over the number of distorted elements to be able to overcome this limitation. The bigger the mesh size in the area, the less distorted elements appear after completing the meshing operations.

4.2.2 Nonlinear problem and automatic stabilization

For the case under study, nonlinear simulations will be carried out as is expected to find a nonlinear load-displacement curve as a result of the analysis. In Abaqus, to execute nonlinear simulation involves the following, as shown in [39]:

- a combination of incremental and iterative procedures;
- using the Newton method to solve the nonlinear equations;
- determining convergence;
- defining loads as a function of time; and
- choosing suitable time increments automatically.

Therefore, Abaqus breaks the step where the load is applied into increments. The software will automatically choose the size of each of the increments based on the convergence evolution of previous increments.

Also, nonlinear static problems may become unstable. One of the possible sources of such instabilities is buckling. A model where buckling appears locally may not be resolvable using general solution methods. For this kind of cases, it becomes necessary to either solve the problem dynamically or with the aid of artificial damping.

Since the above situation represents what it is expected to be found in the model response, a constant artificial damping factor will be used throughout the whole step to account for the appearance of local instabilities.

Automatic stabilization with a constant damping factor implies that viscous forces of the form:

$$F_v = c\mathbf{M}\mathbf{v} \quad (4.1)$$

are added to the global equilibrium equations:

$$P - I - F_v = 0, \quad (4.2)$$

where I represents the internal forces, P the external forces, \mathbf{M} is the artificial mass matrix calculated with unity density, c is the defined damping factor, $\mathbf{v} = \Delta\mathbf{u}/\Delta t$ is the vector of nodal velocities, and Δt is the increment of simulation time.

The final value that is going to be used during the simulations was chosen after performing a small parametric study of the different possibilities. As a result, the plot shown in Figure 4.15 was produced. This plot represents the evolution of the twist at the tip as the load is increased step by step during the nonlinear simulation. As it will be explained in Section 5.1, the use of automatic stabilization becomes

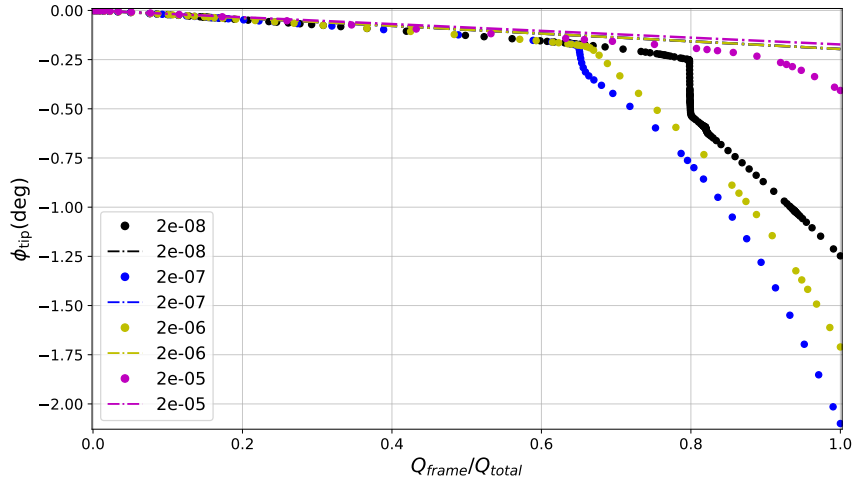


Figure 4.15: Force-displacement curve for various values of constant artificial damping factor.

necessary to capture the dynamics that involve buckling on the chiral ligaments and the ultimate collapse of the structure.

As it can be seen in the mentioned figure, all the different values of the damping factors success to capture the rapidly change in tip twist that occurs for fractions of load applied $> 60\%$. However, special care needs to be taken in order not ensure that the inclusion of artificial damping factor is not leading to inaccurate results due to over-damping of the structure. This can be done why comparing the fraction of the static energy that it is dissipated compared to the external work that its put into the system. This is done for a values of $c = 2 \times 10^{-5}$, $c = 2 \times 10^{-8}$ and $c = 2 \times 10^{-9}$ in Figures 4.16, 4.17 and 4.18, respectively. In this plots, the moment where the structure collapses due to the buckling phenomena occurring on the chiral ligaments can be seen as a sudden change in the slope of both curves. Here it can be seen that the case of $c = 2 \times 10^{-5}$, the slope of the curve showing the energy dissipated through artificial stabilization is positive, which is a sign of over-damping in this region. On the other hand, for the case of $c = 2 \times 10^{-8}$, the slope remains of the curve remains zero. Finally, for the case of $c = 2 \times 10^{-9}$, the slope also remains zero and the final value for the energy dissipated is smaller than for $c = 2 \times 10^{-8}$.

Finally and based on what has been previously explained, it was decided to use damping factor $c = 2 \times 10^{-9}$ for the simulations perform ahead.

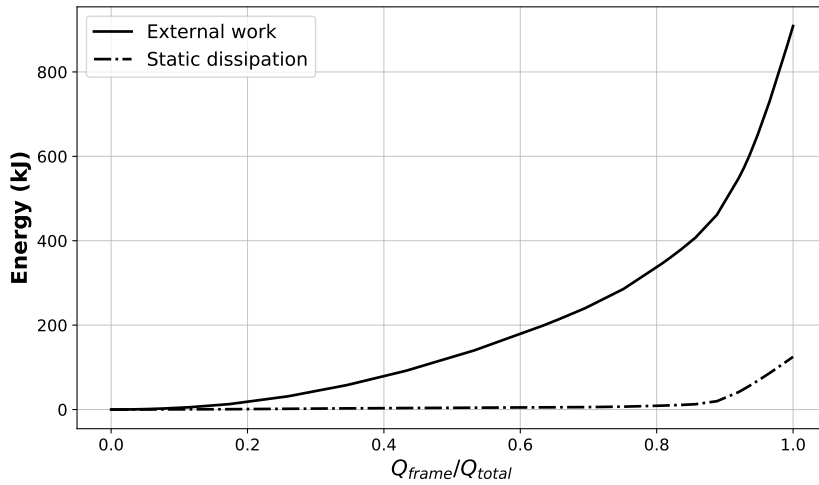


Figure 4.16: External work and static dissipation for a damping factor equal to 2×10^{-5} . The positive slope of the curve showing the energy used in the static dissipation is a sign of over-damping.

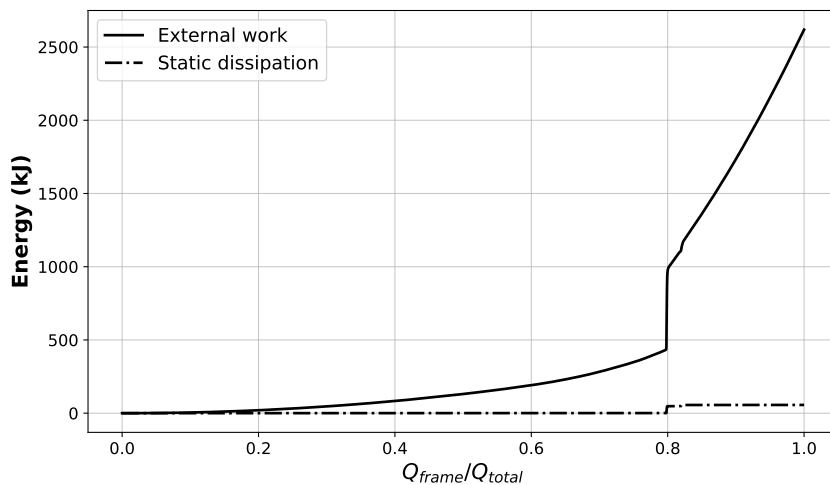


Figure 4.17: External work and static dissipation for a damping factor equal to 2×10^{-8} . After the structure collapse the static dissipation energy remains constant and small compared with the external work introduced into the system.

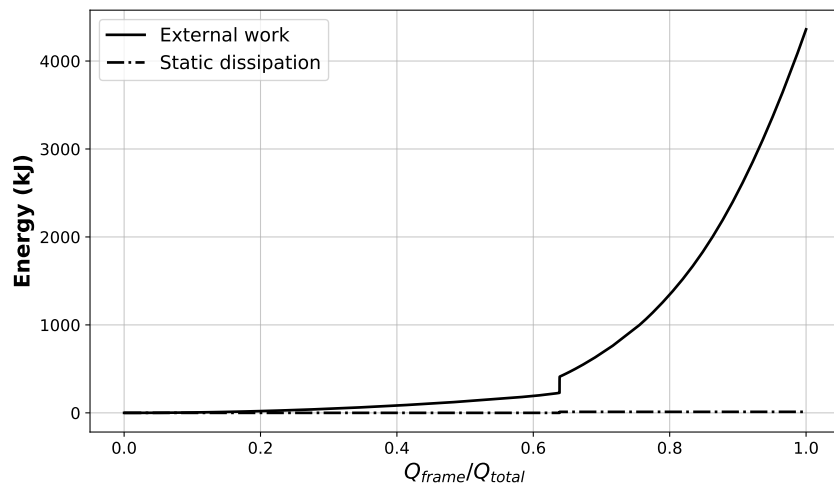


Figure 4.18: External work and static dissipation for a damping factor equal to 2×10^{-9} . After the structure collapse the static dissipation energy remains constant and negligible compared with the external work introduced into the system.

4.2.3 Ribs

Initially, the model did not incorporate inner ribs and the ribs located at the tip and the root had an open profile. In Figure 4.19, it can be seen an example of the response seen for this type of configuration.

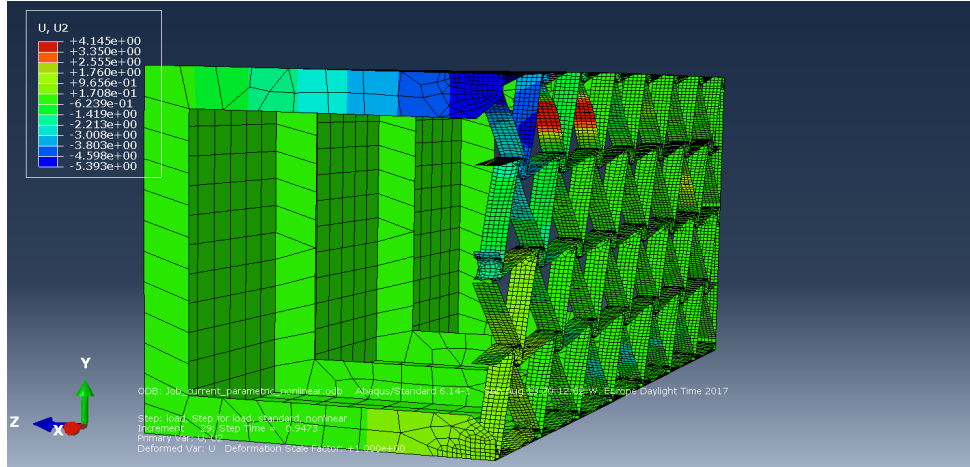


Figure 4.19: Vertical displacement v at the tip rib. The color contour shows those mesh nodes located on the upper flange of the rib have a higher v , therefore showing how the rib is closing under the prescribed load (800 N)

For this reason, it was decided to use ribs with a close profile. The simulations then provided a solution like the one shown in Figure 4.20. For this case, the initial buckling occurs in ligaments located far from the root. The twist of the beam, measured as the angular rotation UR_1 around the x axis is of 0.3 deg. The prescribed load was -800 N and the simulation converged to the 0.95% of the prescribed load.

In order to investigate further deformations of the ligaments, it was decided to carry out simulations that incorporate automation stabilization through artificial damping artificial damping factor, as it was explained in Subsection 4.2.2. After this, the results showed a deformation like the one shown in Figure 4.21. This figure shows how big local deformations appear on the wing-box upper skin for this case. Also, it can be seen that the buckling phenomena has moved backwards to the ligaments close to the root.

In order to reduce the local deformations occurring on the wing-box, a pair of inner ribs as described in Subsection 3.3.1 were added to the model. This element added stiffness to the structure in bending. Now, the response of the model was shown to be like the one represented in Figure 4.22. Here it can be seen that the ligaments that start to buckle are located at the same position as they were in the response of the model that did not incorporate inner ribs seen in Figure 4.20. However, now the degree of deformation has decreased due to the stiffness added to the structure as a result of the inner ribs addition.

However, for this last case, the simulation was only able to converge up to 13% of the prescribed

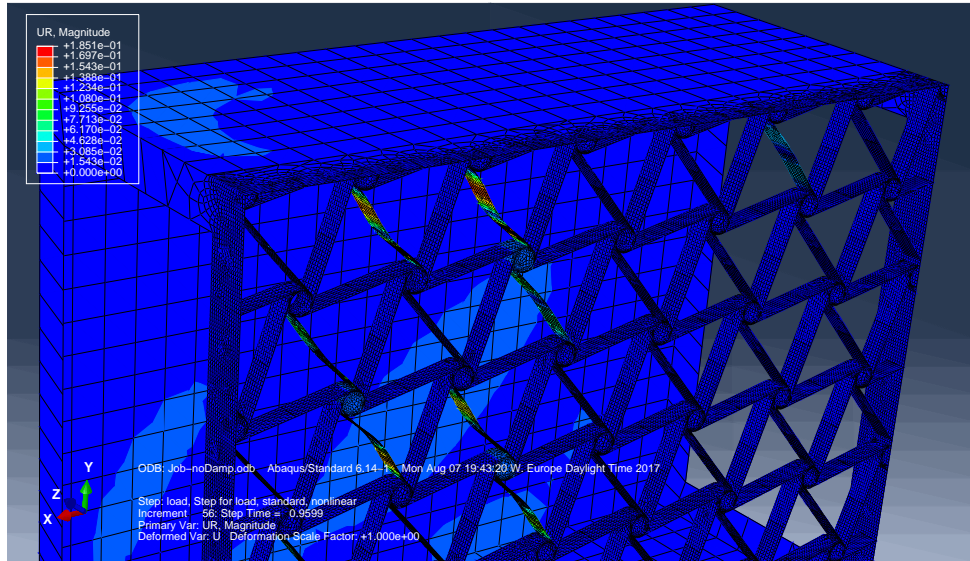


Figure 4.20: Model response without the use of inner ribs nor automatic stabilization.

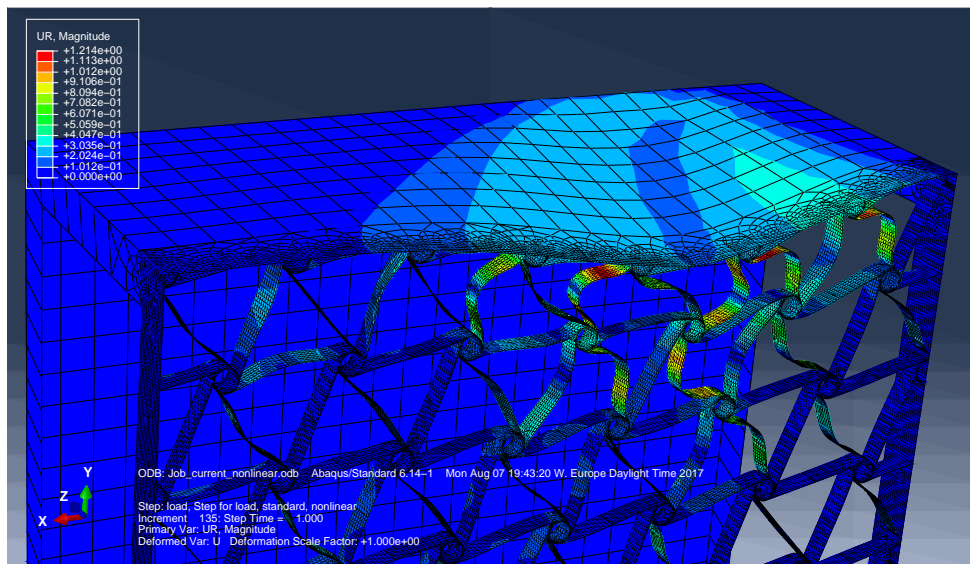


Figure 4.21: Model response without the use of inner ribs with automatic stabilization.

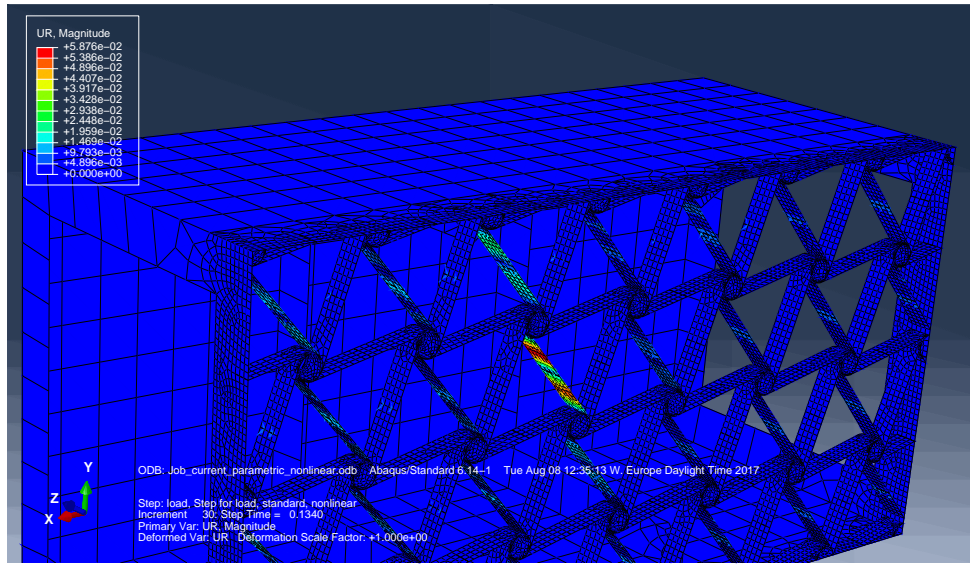


Figure 4.22: Model response incorporating inner ribs and without automatic stabilization

load. In order to progress further in the analysis, the use of automatic stabilization becomes necessary again. For this reason, in the final configuration, automatic stabilization through constant damping factor will be used together with the inner ribs. A description of the response of the structure for this last case is presented on next chapter.

Chapter 5

Simulations results

In the present chapter, the results obtained from the simulations completed in Abaqus CAE are presented. Firstly, the general response of the structure is characterized for the baseline configuration. A description of the elastic instability that the chiral ligaments undergo is included. Also, the nonlinear response in twist angle of the structure is shown.

Secondly, the results obtained from the parametric study performed are presented. Here, the influence of each of the parameters on the nonlinear response in twist of the structure and the buckling phenomena are shown.

5.1 General response characterization

In this section, the general response of the model is characterized. For the wing-box, the nominal value of its characteristic parameters are those shown in Table 3.2, while Tables 3.1 and 3.3 contain the nominal values of the main parameters for the chiral lattice and the ribs, respectively. Also, the baseline configuration will incorporate a pair of inner ribs and the load will be applied on a single mesh node on the upper flange of the tip rib, as described in Subsection 3.3.3.

In the simulations, automatic stabilization artificial through constant damping factor is included. For this case, the response of the structure when 65% of the prescribed load has been applied is the one shown in Figure 5.1. It can be seen that buckling starts and it is more severe in the ligament located just after the inner rib located closer to the root. In a further load increment, buckling phenomena moves backwards and those ligaments located close to the root and at a higher y coordinate, start to deform even more severely. At this point, the structure collapses and the twist increases for smaller increments in the applied load. This can be seen in Figure 5.2.

This is the point at which the local instabilities are such that there is need of adding artificial damping factor in order to capture the structure dynamics. After this point, the artificial damping allows the simu-

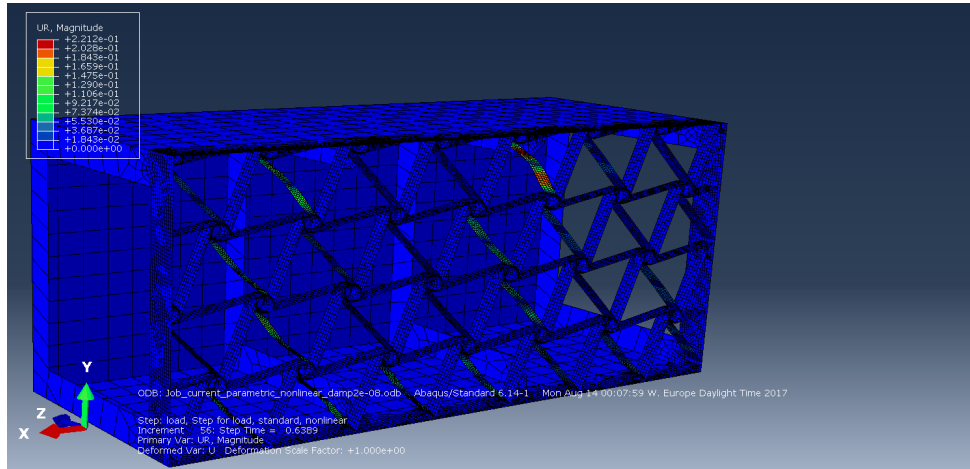


Figure 5.1: Baseline model response when the fraction of load applied equals to 63% of the prescribed load (700 N). Buckling has appeared and it is more severe on the ligament which is next to the inner rib located closer to the root.

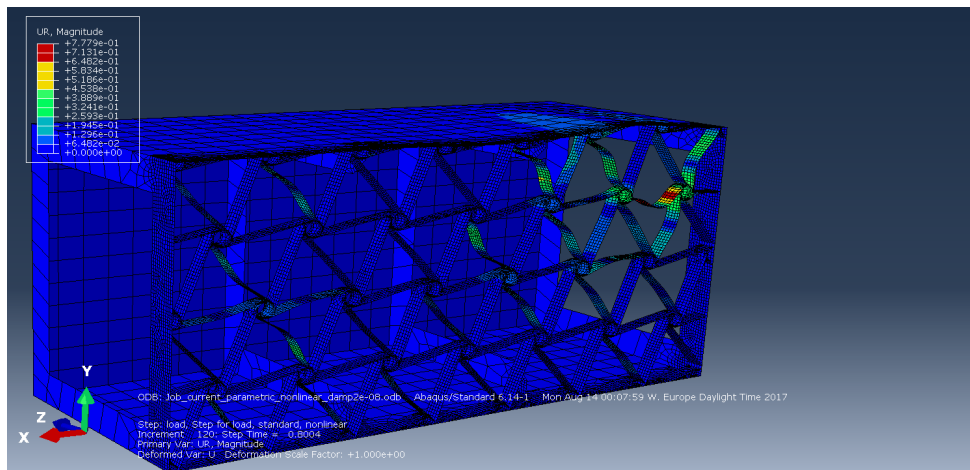


Figure 5.2: Baseline model response when the fraction of load applied equals to 80% of the prescribed load (700 N). Severe buckling appears in those chiral ligaments located at the root and with a higher y coordinate. This is the point when the structure collapses and the twist increases for smaller increments in the applied load.

lation to continue. As it was explained in Subsection 4.2.2, special care needs to be taken to ensure that the inclusion of artificial damping factor is not leading to inaccurate results due to over-damping of the structure. This can be done why comparing the fraction of the static energy that it is dissipated compared to the external work that its put into the system. The Figure 5.3 makes this comparison possible. It can be seen that effectively, the static dissipation through automatic stabilization is negligible in comparison with the external work. This figure also shows the abrupt increment in external work at the point where the structure collapses due to sudden buckling of the chiral ligaments.

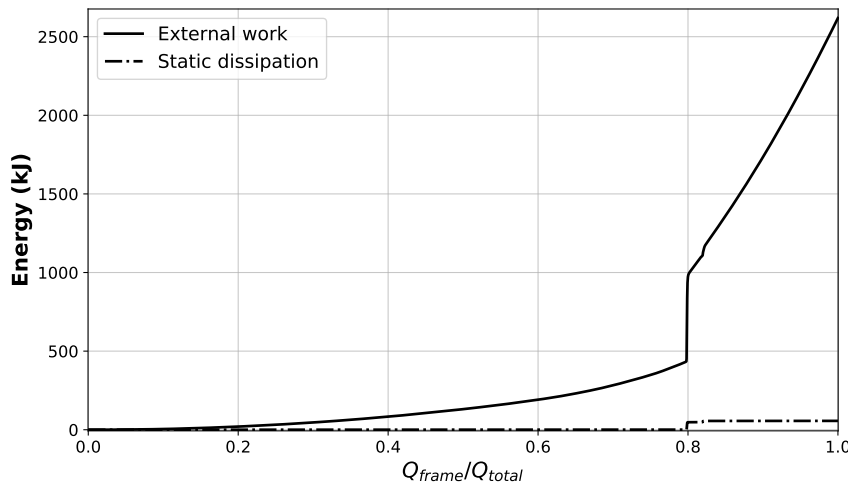


Figure 5.3: External work and static dissipation for a simulation of the baseline configuration. It can be seen that the static dissipation through automatic stabilization is negligible in comparison with the external work showing that the inclusion of artificial damping factor is unluckily to be leading to inaccurate results. The abrupt change in the external work shows the point where structure collapses due to sudden buckling of the chiral ligaments.

In order to see the overall system response as load increases, a load-displacement curve can be plotted. The Figure 5.4 shows the typical twist variation as the load is increased. On this plot, the results from the nonlinear simulations are shown as the set of scatter points while the dotted line represents the forecast final twist from the linear simulation. In the case shown, the linear simulation arises a twist at the tip ϕ_{tip} equal to -0.196 degrees while the nonlinear simulation predicts a final twist of -1.248 degrees. This shows how the problem under study is highly nonlinear.

The nonlinear response also shows the point where the structure collapses that its located at the point where approximately 80% of the load has been applied. The deformation state of the structure at this point was the one shown in Figure 5.2. The plot also, shows another point where the deformation rapidly changes. This point is approximately located at the point where the load fraction is 82%. This shows the structure entering in the second stage of its deformation. Here, the buckling is more generalized and buckling appears in more ligaments apart from those at the root. This can be seen in Figure 5.5. The location of this second deformation breakdown varies widely with the choose of parameters.

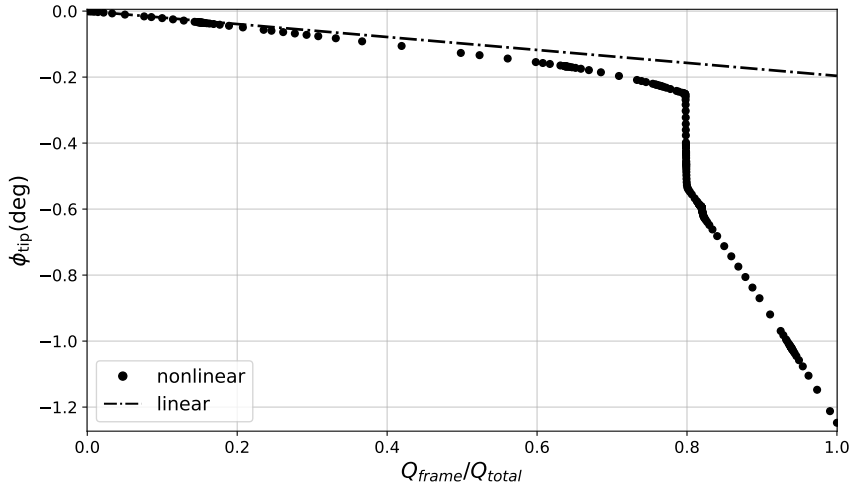


Figure 5.4: Force-displacement curve for the baseline configuration. Two breakdowns for the buckling deformation are shown in the plot. The first one is located at the point where the fraction of applied load equals to 80% and the second one at the point where the fraction is 82%.

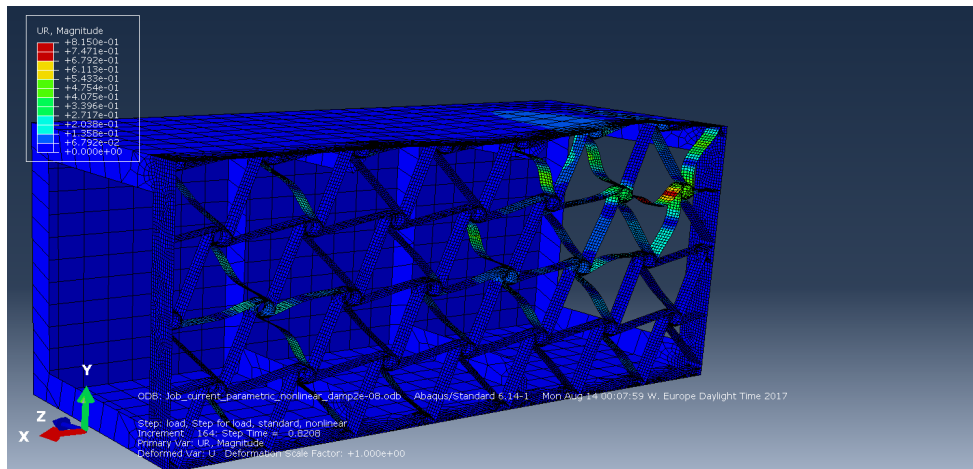


Figure 5.5: Baseline model response when the fraction of load applied equals to 82% of the prescribed load (700 N). In this case, not only the ligaments located at the root show severe buckling but also, other located at different points of the chiral lattice has started to buckle at the same time, inducing rapidly growing deformation for small increments in load.

5.2 Parametric study on the computational model

The aim of this section is to show the effect of each parameter on the nonlinear response of the structure. The parameters that will be included in the analysis are the following:

- Wing-box thickness t_{box}
- Number of unit cells in the transversal direction M
- Number of unit cells in the spanwise direction N
- Chiral node depth B_{chiral}
- Chiral node radius r_{chiral}
- Chiral lattice thickness t_{chiral}
- Chiral ligament half length L_{chiral}
- Dimensionless ligament eccentricity ϵ_{chiral}

5.2.1 Wing-box thickness

In the present subsection the effect of different values for the wing-box thickness t_{box} on the structure response is investigated.

The results from the simulations carried out can be seen in Table 5.1. In the table, the twist at the tip of the wing-box for the Abaqus nonlinear simulation ϕ_{tip} and for the linear simulation $\tilde{\phi}_{\text{tip}}$ are shown. This result is obtained by evaluating the value of the angular deformation u at a number of nodes located in different parts of the beam, as explained in the Subsection 3.3.5. Therefore, the maximum deviation from the calculated mean twist has also been included. Finally, the Table 5.1 also shows the maximum vertical displacement found in the nodes located on the upper wing-box skin.

The evolution of the twist as a function of the load applied can be seen in Figure 5.6 for each of the values of t_{box} studied. It can be seen how the structure only collapses for $t_{\text{box}} = 0.8$ mm and the final value of the twist is much higher than for the remaining cases. For this case, the curve shows the post-buckling evolution of the twist response for increasing values of load applied. The slope of the curve has decreased drastically and the twist achieved after all the prescribed load has been applied is equal to $\phi_{\text{tip}} = -2.15$ deg.

The collapse of the structure for $t_{\text{box}} = 0.8$ mm appears when 60% of the load has been applied, as shown in Figure 5.7. This last plot represents a detailed view of the force-displacement curve that also shows how the nonlinear response differs from the linear one for all the considered cases.

$t_{\text{box}}(\text{mm})$	ϕ_{tip} (deg)	$e(\phi_{\text{tip}})(\%)$	$\tilde{\phi}_{\text{tip}}$ (deg)	$e(\tilde{\phi}_{\text{tip}})(\%)$	v_{\max}	$\hat{z}_{v_{\max}}$	$\hat{x}_{v_{\max}}$
0.8	-2.15	13.575	-0.196	-10.067	-16.908	1	0.334
1	-0.206	9.954	-0.164	-11.316	-1.292	1	0.971
1.2	-0.174	10.288	-0.143	-12.16	-1.081	1	0.971
1.4	-0.158	12.909	-0.13	-14.06	-0.95	1	0.971

Table 5.1: Results from parametric study on the wing-box thickness t_{box} . The results show the twist at the tip of the wing-box for the Abaqus nonlinear simulation ϕ_{tip} and for the linear simulation $\tilde{\phi}_{\text{tip}}$. The maximum relative error of the mean calculation, expressed as percentage, for these two magnitudes is $e(\phi_{\text{tip}})$ and $e(\tilde{\phi}_{\text{tip}})$, respectively. The table also shows the maximum vertical displacement v_{\max} among all the mesh nodes located on the upper skin of the wing-box and the dimensionless position in the spanwise direction $\hat{x}_{v_{\max}}$ and in the chordwise direction $\hat{z}_{v_{\max}}$ of the node that shows $v = v_{\max}$.

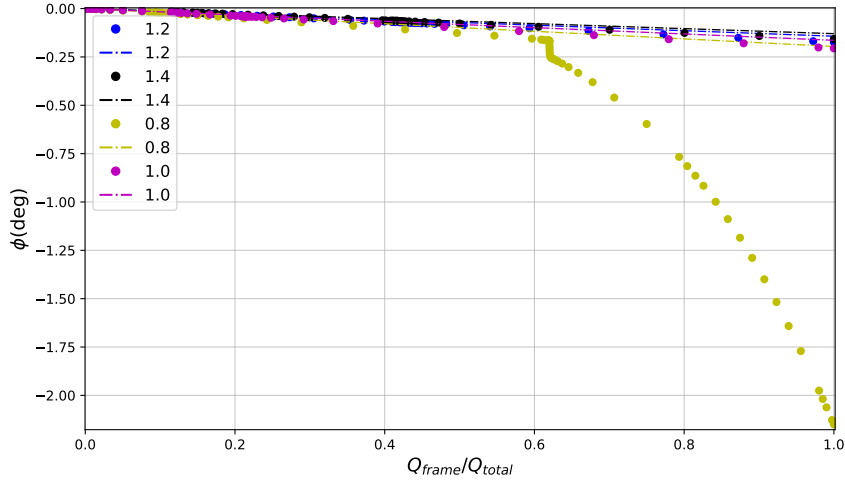


Figure 5.6: Force-displacement curve for various values of the wing-box thickness t_{box} . For all the cases shown, the force applied was located on the upper flange of the tip rib and its magnitude was equal to -800 N.

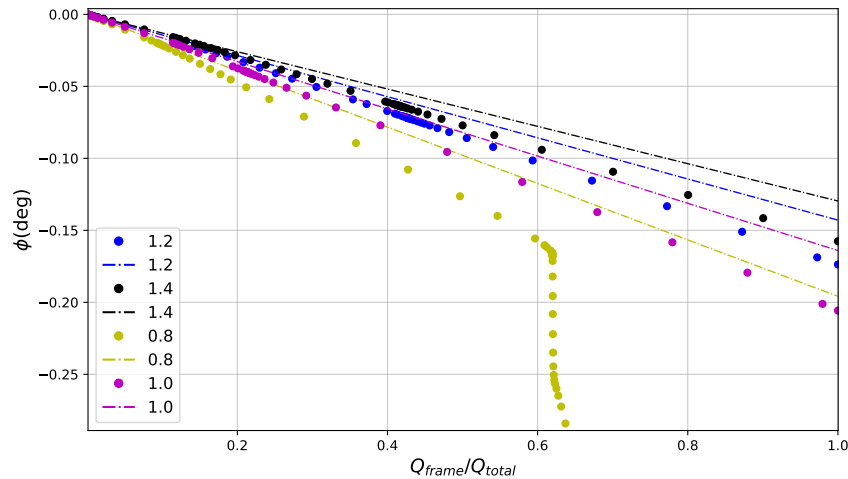


Figure 5.7: Detail of the force-displacement curve for various values of the wing-box thickness t_{box} . For all the cases shown, the force applied was located on the upper flange of the tip rib and its magnitude was equal to -800 N.

The differences in response for the different cases are also shown the color contour plots provided by Abaqus visualization module. The deformation in the ligaments for $t_{\text{box}} = 1.2$ mm when buckling occurs is shown in Figure 5.8 that shows the total rotational displacement of the mesh elements on the color contour. It can be seen that buckling does not propagate to other parts of the lattice and it stays where it had appeared on first place, at the first ligaments after the inner rib located further from the root.

On the other hand, in Figure 5.9 the same plot is shown for a value of wing-box thickness of $t_{\text{box}} = 0.8$ mm. This figure shows the post-buckling state of the structure. In this region, each of the ligaments that had buckled increase its deformation. There are not any new ligaments starting to buckle. It is possible to see that some local deformation has been induced into the upper skin of the wing-box in between the root and the first inner rib. As shown in Table 5.1, for the case $t_{\text{box}} = 0.8$ mm, the point with the maximum vertical is shown to appear close to the root, where $\hat{x}_{v_{\max}} = 0.334$.

A further study was performed in order to see the relationship between the wing-box thickness and the value of the force applied that induces the structure to collapse. As a result, the plot shown in Figure 5.10 was produced.

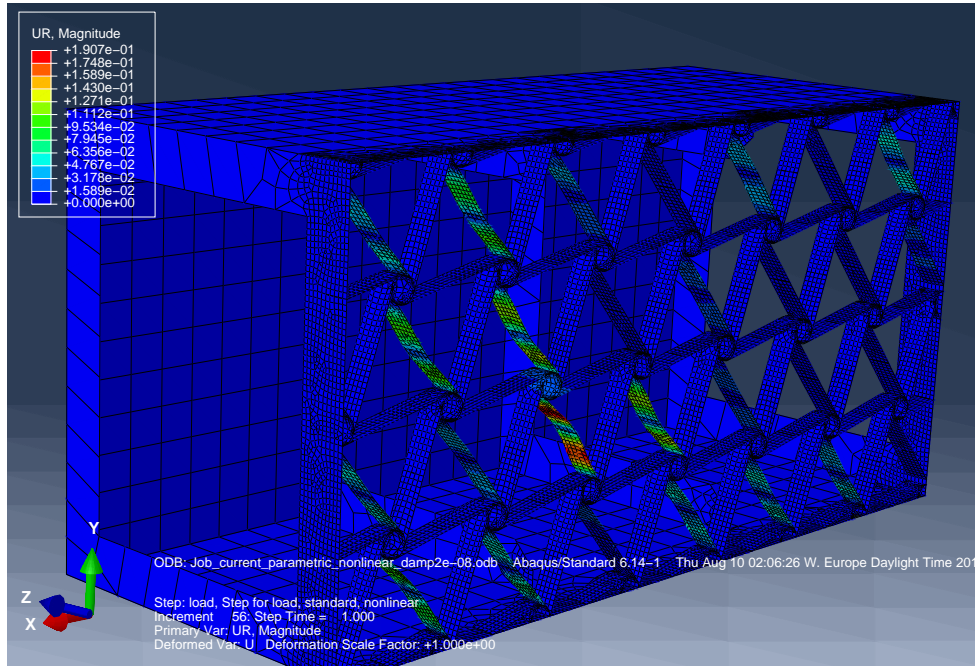


Figure 5.8: Color contour representation of the total angular displacement of the mesh elements on the deformed structure for $t_{\text{box}} = 1.2 \text{ mm}$. This case is shown after all the prescribed load (800 N) has been applied.

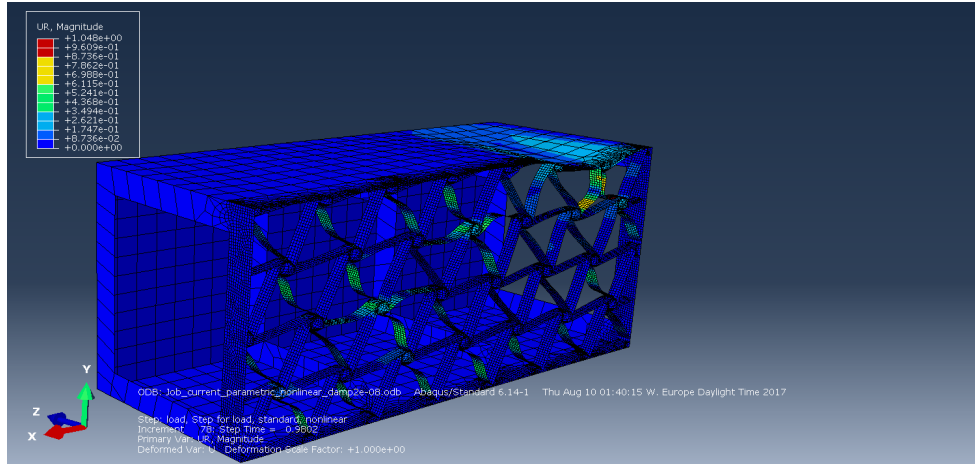


Figure 5.9: Color contour representation of the total angular displacement of the mesh elements on the deformed structure for $t_{\text{box}} = 0.8 \text{ mm}$.

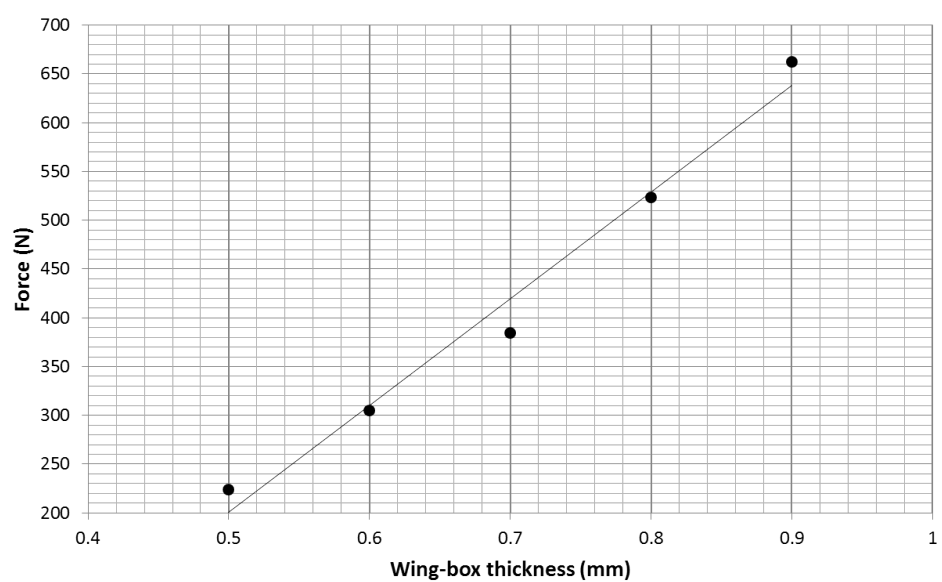


Figure 5.10: Force that induces the structure to collapse as a function of the wing-box thickness t_{box} .

5.2.2 Number of unit cells in the chiral lattice

Now the effect of the number of units cells in the transversal direction M and in the spanwise direction N on the structural response is investigated.

Firstly, the number of unit cells in the transversal direction M is varied. This parameter modifies the height of the model. Similarly as it was done for the study of the wing-box thickness t_{box} influence in the structure response, the results from the different simulations are shown in Table 5.2. Also, the force-displacement curve is shown in Figure 5.11. It can be seen from results that increments a higher M resulted on a decrement of the structure sensitivity to buckling. For the case of $M = 5$, the structure did not collapse under the prescribed load of 1000 N.

M	ϕ_{tip} (deg)	$e(\phi_{\text{tip}})$ (%)	$\tilde{\phi}_{\text{tip}}$ (deg)	$e(\tilde{\phi}_{\text{tip}})$ (%)	v_{\max}	$\hat{z}_{v_{\max}}$	$\hat{x}_{v_{\max}}$
3	-5.179	13.559	-0.245	-10.074	-29.166	1	0.971
4	-0.392	22.16	-0.148	-10.447	-6.093	1	0.334
5	-0.214	14.893	-0.164	-17.526	-1.018	0.6	0.971

Table 5.2: Results from parametric study on the number of unit cells in the transversal direction M . The results show the twist at the tip of the wing-box for the Abaqus nonlinear simulation ϕ_{tip} and for the linear simulation $\tilde{\phi}_{\text{tip}}$. The maximum relative error of the mean calculation, expressed as percentage, for these two magnitudes is $e(\phi_{\text{tip}})$ and $e(\tilde{\phi}_{\text{tip}})$, respectively. The table also shows the maximum vertical displacement v_{\max} among all the mesh nodes located on the upper skin of the wing-box and the dimensionless position in the spanwise direction $\hat{x}_{v_{\max}}$ and in the chordwise direction $\hat{z}_{v_{\max}}$ of the node that shows $v = v_{\max}$.

From the results shown in Table 5.5 it can be seen how for the case of $M = 3$, the point that shows $v = v_{\max}$ is located at the wing-box tip where $\hat{x}_{v_{\max}} = 0.971$, due to the high twist of the structure. However, for $M = 4$, the structure has gained stiffness in shear and, even the prescribed load makes the structure to collapse when buckling phenomena appears, the achieved twist ϕ_{tip} is $\approx 7\%$ inferior than what it was obtained for $M = 3$. For $M = 5$, the structure is so stiff that v_{\max} appears approximately at the point where the load is applied. This shows that deformation is only achieved in the vicinity of the load introduction point due to the high stiffness in shear of the structure.

The effects of the variation of the number of unit cells in the spanwise direction N , parameter responsible of the wing-box length is investigated next. The results from the parametric study carried out are shown in Table 5.3. The force-displacement curve for the simulations carried out is shown in Figure 5.12. It can be seen that the bigger the wing-box length, the earlier that the buckling of the lattices cause the collapse of the structure.

In the last plot introduced it can be seen a second change in the slope of the curve for the cases of $N = 10$ and $N = 11$. This happens when, as explained in Section 5.1, the buckling phenomena progresses from the ligaments at the root to be more generalized in other parts of the structure. This characteristic can be seen in Figure 5.13, where the response of the structure for the case of $N = 10$ and load fraction of 96% is shown.

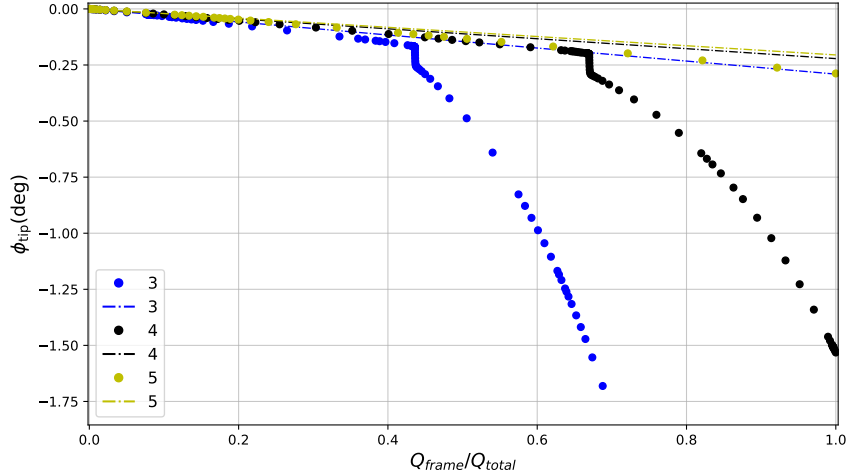


Figure 5.11: Force-displacement curve for various values of the number of unit cells in the transversal direction M . For all the cases shown, the load introduction point was located in the middle of the upper flange of the tip rib and its magnitude was equal to -1200 N.

N	ϕ_{tip} (deg)	$e(\phi_{\text{tip}})$ (%)	$\tilde{\phi}_{\text{tip}}$ (deg)	$e(\tilde{\phi}_{\text{tip}})$ (%)	v_{\max}	$\hat{z}_{v_{\max}}$	$\hat{x}_{v_{\max}}$
7	-0.185	16.474	-0.14	-12.506	-1.061	1	0.971
8	-0.878	9.517	-0.17	-10.196	-9.844	1	0.334
9	-4.582	11.091	-0.209	-7.848	-25.781	1	0.971
10	-8.116	6.192	-0.248	-6.398	-46.636	1	0.971
11	-17.659	4.954	-0.299	-5.098	-107.229	1	0.971
12	-22.007	6.527	-0.337	-3.08	-137.131	1	0.971

Table 5.3: Results from parametric study on the number of unit cells in the spanwise direction M . The results show the twist at the tip of the wing-box for the Abaqus nonlinear simulation ϕ_{tip} and for the linear simulation $\tilde{\phi}_{\text{tip}}$. The maximum relative error of the mean calculation, expressed as percentage, for these two magnitudes is $e(\phi_{\text{tip}})$ and $e(\tilde{\phi}_{\text{tip}})$, respectively. The table also shows the maximum vertical displacement v_{\max} among all the mesh nodes located on the upper skin of the wing-box and the dimensionless position in the spanwise direction $\hat{x}_{v_{\max}}$ and in the chordwise direction $\hat{z}_{v_{\max}}$ of the node that shows $v = v_{\max}$.

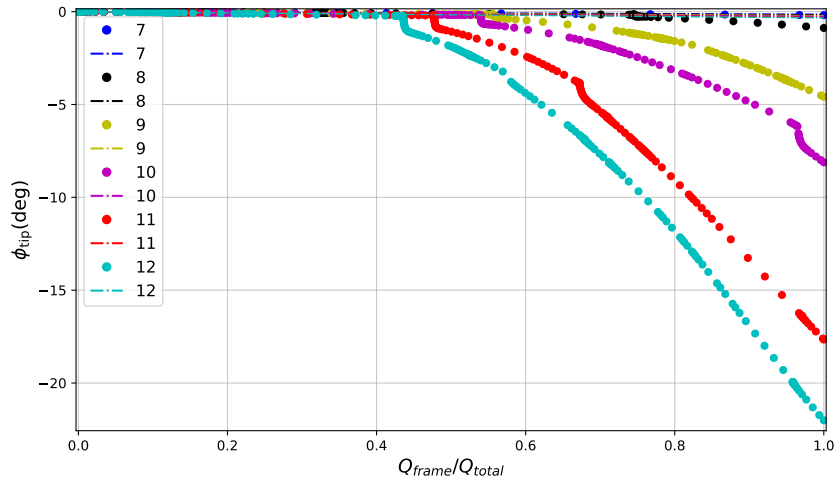


Figure 5.12: Force-displacement curve for various values of the number of unit cells in the spanwise direction N . For all the cases shown, the load introduction point was located in the middle of the upper flange of the tip rib and its magnitude was equal to -700 N.

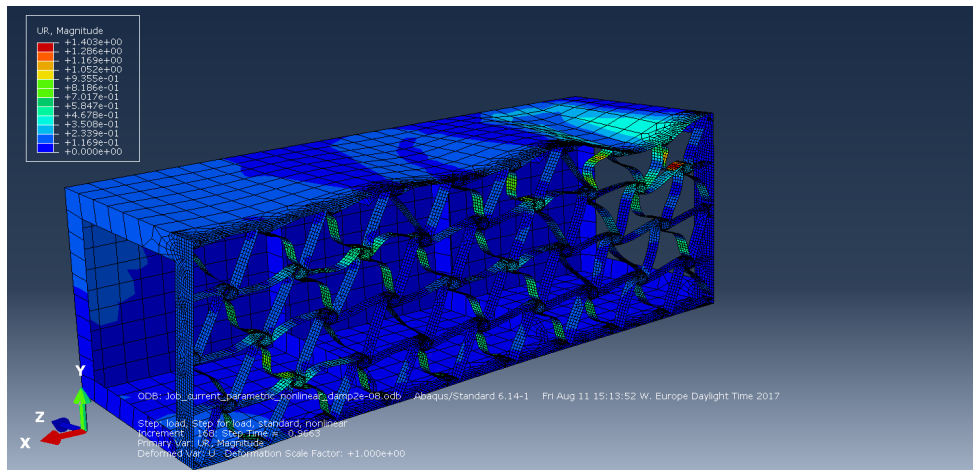


Figure 5.13: Model response when the fraction of load applied equals to 96% of the prescribed load (700 N) and $N = 10$. The plot shows how the buckling phenomena is generalized for the whole chiral structure.

5.2.3 Chiral lattice parameters

In the present subsection, different parameters of the chiral lattice structure are varied and its effect of the system response are shown.

Dimensionless chiral ligament eccentricity $\varepsilon_{\text{chiral}}$

The first of the chiral parameter that is going to be studied is the ligament eccentricity e_{chiral} , in its dimensionless form $\varepsilon_{\text{chiral}}$. The numeric results from the simulations carried out can be seen in Table 5.4.

The force-deformation curve for the range of simulations carried out can be seen in Figure 5.14. Here it can be seen that the collapse of the structure occurs for all the cases except for $\varepsilon_{\text{chiral}} = 0.1$. The deformation state of the structure for this case can be seen in Figure 5.15 that shows how the excessive eccentricity of the ligaments keep them from buckling and causing the structure collapse.

$\varepsilon_{\text{chiral}}$	ϕ_{tip} (deg)	$e(\phi_{\text{tip}})$ (%)	$\tilde{\phi}_{\text{tip}}$ (deg)	$e(\tilde{\phi}_{\text{tip}})$ (%)	v_{\max}	$\hat{z}_{v_{\max}}$	$\hat{x}_{v_{\max}}$
0.0	-0.903	9.547	-0.166	-10.14	-9.806	1	0.334
0.001	-1.314	13.715	-0.168	-9.931	-12.441	1	0.334
0.01	-0.877	9.525	-0.17	-10.196	-9.831	1	0.334
0.05	-0.724	9.511	-0.188	-10.598	-8.483	1	0.334
0.1	-0.222	9.444	-0.194	-10.601	-1.416	1	0.971

Table 5.4: Results from parametric study on chiral ligament eccentricity $\varepsilon_{\text{chiral}}$. The results show the twist at the tip of the wing-box for the Abaqus nonlinear simulation ϕ_{tip} and for the linear simulation $\tilde{\phi}_{\text{tip}}$. The maximum relative error of the mean calculation, expressed as percentage, for these two magnitudes is $e(\phi_{\text{tip}})$ and $e(\tilde{\phi}_{\text{tip}})$, respectively. The table also shows the maximum vertical displacement v_{\max} among all the mesh nodes located on the upper skin of the wing-box and the dimensionless position in the spanwise direction $\hat{x}_{v_{\max}}$ and in the chordwise direction $\hat{z}_{v_{\max}}$ of the node that shows $v = v_{\max}$.

The Figure 5.14 also shows that the case of $\varepsilon_{\text{chiral}} = 0.0$, that is when the ligaments are flat, is not the case that shows the structure as more sensitive to buckling. Instead, for $\varepsilon_{\text{chiral}} = 0.001$ the structure collapses at a smaller load. In order to investigate the load required to make the structure collapse for each particular value of $\varepsilon_{\text{chiral}}$, the plot shown in Figure 5.16 was produced. This shows a minimum for $\varepsilon_{\text{chiral}} = 0.001$ showing that different buckling mechanism occurs when the eccentricity is null and when it is not. To investigate this characteristic, the deformed state of the structure is shown for $\varepsilon_{\text{chiral}} = 0.0$ and $\varepsilon_{\text{chiral}} = 0.001$ in Figures 5.17 and 5.18, respectively. This shows effectively, that the buckling mechanism change from case to case. When the eccentricity is null, the structure collapses when buckling appears in two ligaments at the upper part of the root making them to deform and displace the one against the other. However, when the eccentricity is not null, these two ligaments where buckling occurs displace in the same direction towards decreasing values of x .

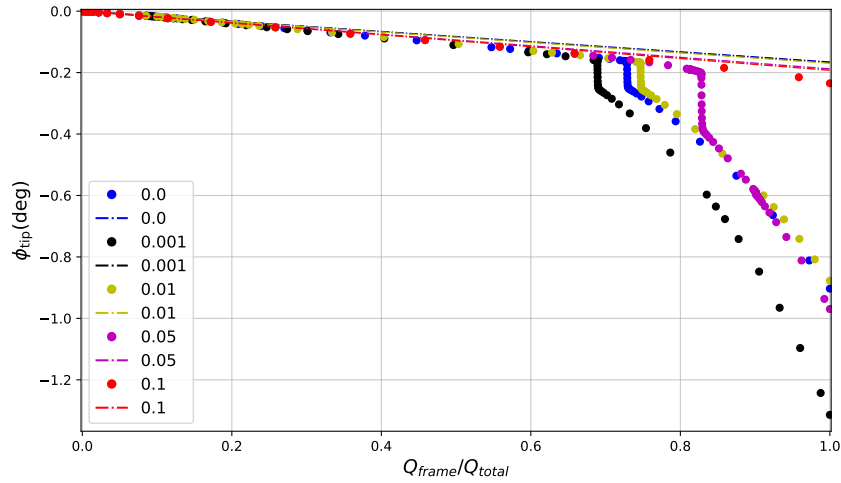


Figure 5.14: Force-displacement curve for various values of the dimensionless chiral ligament eccentricity ϵ_{chiral} . The plot shows how the collapse of the structure occurs for all the cases except for $\epsilon_{chiral}=0.1..$

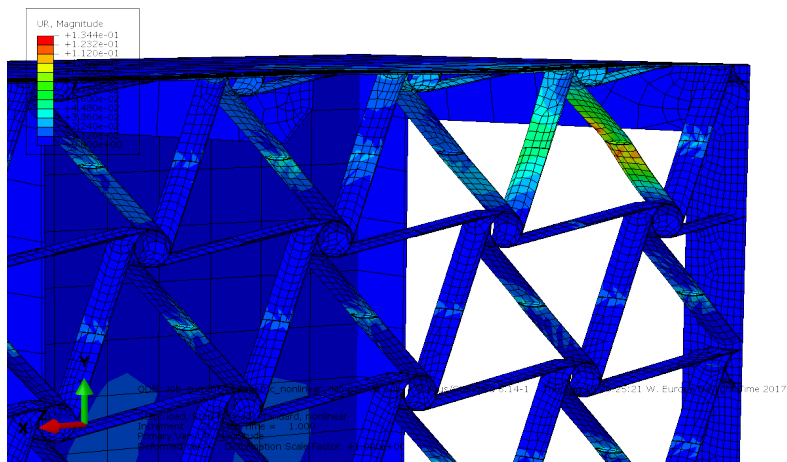


Figure 5.15: Model response when the fraction of load applied equals to 100% of the prescribed load (700 N) and $\epsilon_{chiral}=0.1$. For this case, the excessive ligament eccentricity at the end of the simulation keeps it from buckling and causing the structure collapse.

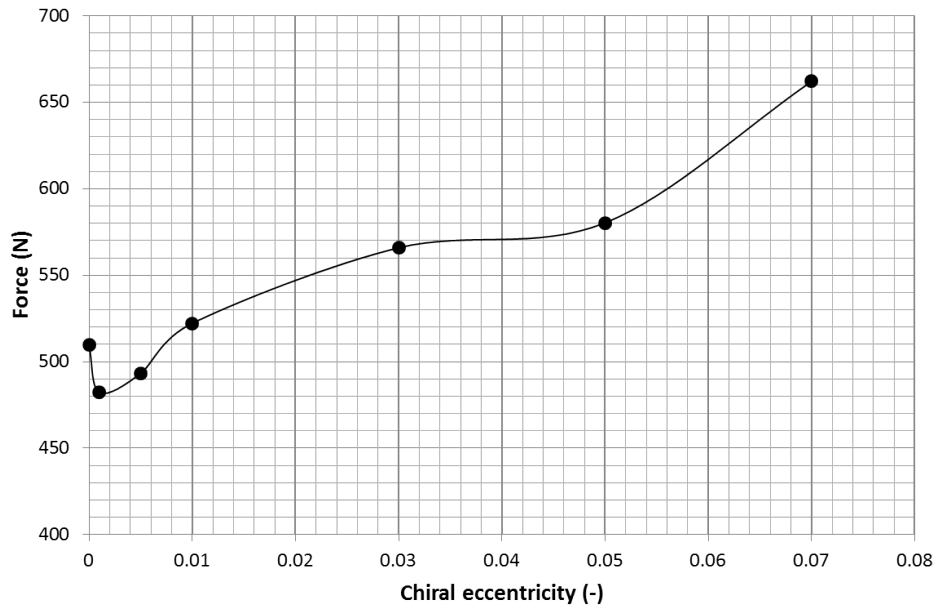


Figure 5.16: Force that induces the structure to collapse as a function of the chiral ligament eccentricity $\varepsilon_{\text{chiral}}$. It can be seen that the .

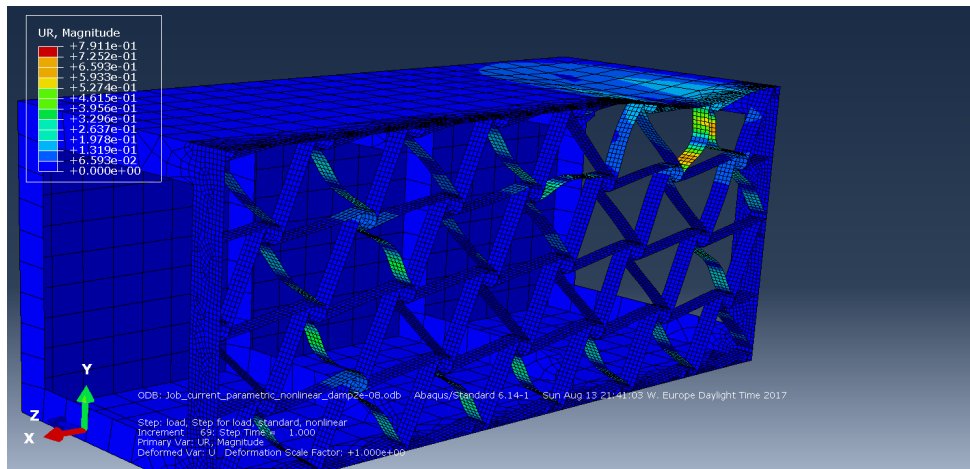


Figure 5.17: Model response when the fraction of load applied equals to 72% of the prescribed load (700 N) and $\varepsilon_{\text{chiral}} = 0.0$. For this case, the structure collapse occurs when buckling appears on the ligaments located at the upper part of the root. The deformation makes ligaments to displace the one against each other.

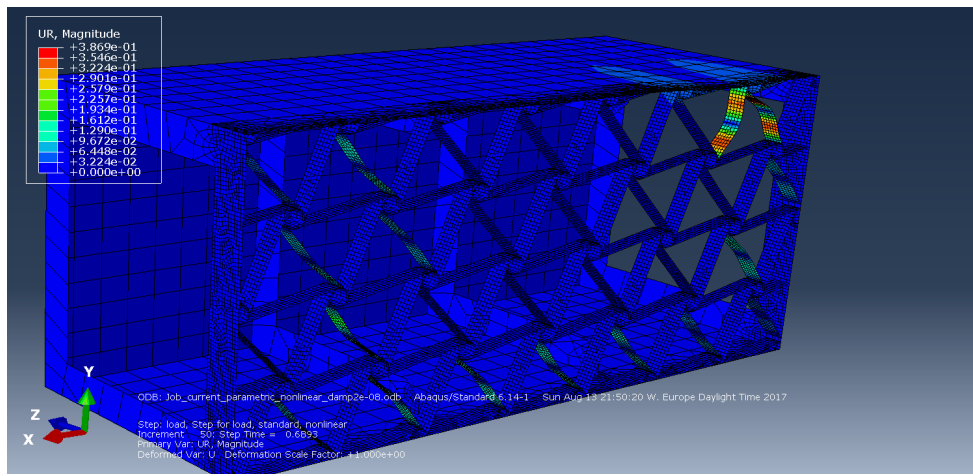


Figure 5.18: Model response when the fraction of load applied equals to 68% of the prescribed load (700 N) and $\varepsilon_{\text{chiral}} = 0.001$. For this case, the structure collapse occurs when buckling appears on the ligaments located at the upper part of the root. The deformation makes ligaments to displace in the same direction towards decreasing values of x .

Chiral node depth B_{chiral}

The numeric results from the parametric analysis on the chiral node depth B_{chiral} can be seen in Table 5.5. The force-displacement curve can be seen in Figure 5.19 for various values of B . This plot shows how the bigger B_{chiral} is, the more abrupt the collapse is, showing a bigger sudden increment on the measured twist at the tip ϕ_{tip} .

The Figure 5.20 shows the rotation u around the x direction of the mesh elements located on the upper skin of the wing-box and close to the root. This is represented for the case of $B_{\text{chiral}} = 30$ mm, at the moment when collapse of the structure occurs which is at 86% of the prescribed load and in the area where local deformation of the skin takes place. Examination of the plot arises that the value of u in this area is approximately double to that corresponding to $B_{\text{chiral}} = 10$ mm which can be seen in Figure 5.21. This shows that the bigger B_{chiral} is, the more area is affected by the ligaments deformation when buckling occurs and the greater the local deformation will be.

When plotting the force that makes the structure to collapse against the corresponding value of chiral node depth depth B_{chiral} , the Figure 5.22 was produced.

B_{chiral}	ϕ_{tip} (deg)	$e(\phi_{\text{tip}})$ (%)	$\tilde{\phi}_{\text{tip}}$ (deg)	$e(\tilde{\phi}_{\text{tip}})$ (%)	v_{\max}	$\hat{z}_{v_{\max}}$	$\hat{x}_{v_{\max}}$
10	-1.082	9.61	-0.187	-10.614	-10.941	1	0.334
20	-0.877	9.525	-0.17	-10.196	-9.831	1	0.334
30	-0.71	9.528	-0.16	-9.838	-8.75	1	0.334

Table 5.5: Results from parametric study on chiral node depth B_{chiral} . The results show the twist at the tip of the wing-box for the Abaqus nonlinear simulation ϕ_{tip} and for the linear simulation $\tilde{\phi}_{\text{tip}}$. The maximum relative error of the mean calculation, expressed as percentage, for these two magnitudes is $e(\phi_{\text{tip}})$ and $e(\tilde{\phi}_{\text{tip}})$, respectively. The table also shows the maximum vertical displacement v_{\max} among all the mesh nodes located on the upper skin of the wing-box and the dimensionless position in the spanwise direction $\hat{x}_{v_{\max}}$ and in the chordwise direction $\hat{z}_{v_{\max}}$ of the node that shows $v = v_{\max}$.

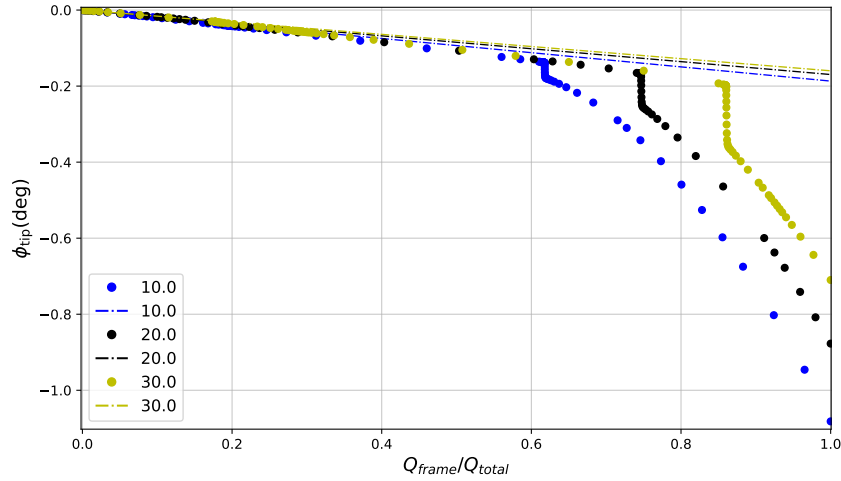


Figure 5.19: Force-displacement curve for various values of the dimensionless chiral node depth B_{chiral} . Results show how the bigger the node depth B_{chiral} is, the later the collapse of the structure occurs but the more abrupt is its.

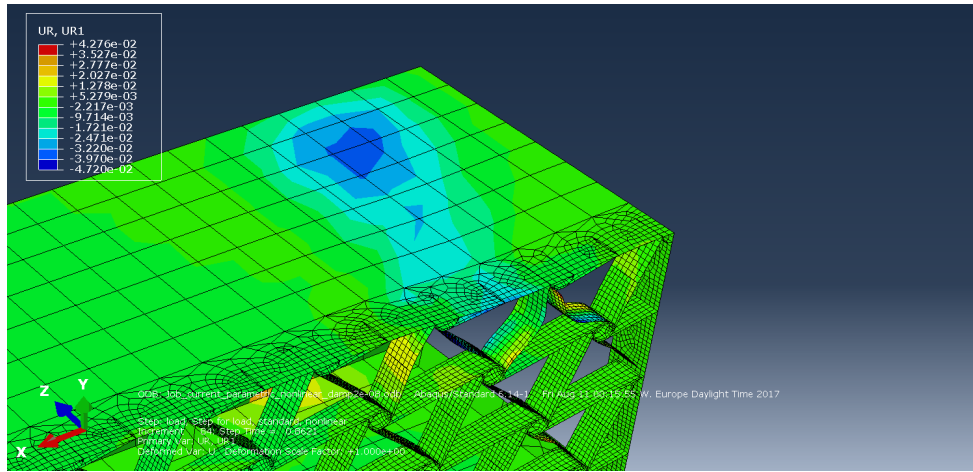


Figure 5.20: Model response when the fraction of load applied equals to 86% of the prescribed load (700 N) and $B_{chiral}=30$ mm. The plot shows a color contour with the value of the rotational displacement u around the x direction at the moment in which the structure collapses. In the area where the local deformation occurs, the value of u is approximately equal to -0.033 rad.

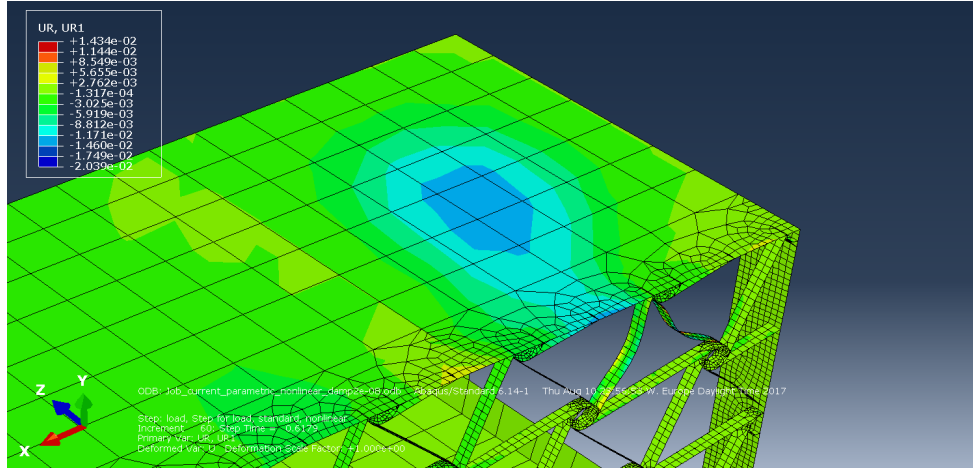


Figure 5.21: Model response when the fraction of load applied equals to 62% of the prescribed load (700 N) and $B_{\text{chiral}} = 10 \text{ mm}$. The plot shows a color contour with the value of the rotational displacement u around the x direction at the moment in which the structure collapses. In the area where the local deformation occurs, the value of u is approximately equal to -0.015 rad .

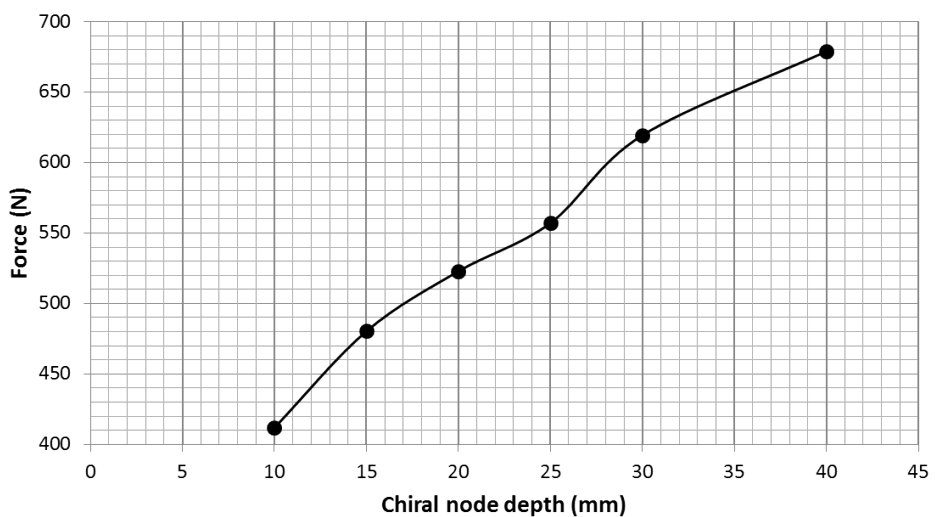


Figure 5.22: Force that induces the structure to collapse as a function of the chiral node depth B_{chiral} .

Chiral node radius r_{chiral}

In the case of the chiral node radius r_{chiral} , the possible values were limited by the geometry of the chiral lattice. For values $r_{\text{chiral}} \leq 5$ mm, it was not possible to build the mode due to interferences between the different ligaments that joined at each of the nodes. The numeric results from the simulations are presented in Table 5.6.

The force-displacement curve obtained from the simulations is shown in Figure 5.23. This curve shows how the structure collapses for analyzed cases except for $r_{\text{chiral}} = 17.5$ mm and $r_{\text{chiral}} = 20$ mm. For $r_{\text{chiral}} = 12.5$ mm, the buckling ligaments are located at the root, as it can be seen in Figure 5.24. However, for the case of $r_{\text{chiral}} = 17.5$ mm, buckling do not occur on the ligaments located at the root but in those located just after the inner rib located closer to the root, with smaller x . This explains the characteristic seen in Figure 5.23 for the case of $r_{\text{chiral}} = 17.5$ mm which breaks the trend followed by values $r_{\text{chiral}} < 17.5$ mm. Then, the chiral node radius r_{chiral} value shifts the position of the buckling ligaments that origin the collapse of the structure.

The variation of the force that makes the structure to collapse as a function of the chiral node radius r_{chiral} can be seen in Figure 5.26.

r_{chiral}	ϕ_{tip} (deg)	$e(\phi_{\text{tip}})(\%)$	$\tilde{\phi}_{\text{tip}}$ (deg)	$e(\tilde{\phi}_{\text{tip}})(\%)$	v_{\max}	$\hat{z}_{v_{\max}}$	$\hat{x}_{v_{\max}}$
7.5	-1.184	13.64	-0.171	-10.046	-11.586	1	0.331
10	-0.877	9.525	-0.17	-10.196	-9.831	1	0.334
12.5	-0.886	9.596	-0.17	-10.247	-10.051	1	0.337
15	-1.121	13.638	-0.173	-10.134	-11.677	1	0.342
17.5	-0.273	9.481	-0.171	-10.215	-4.169	1	0.568
20	-0.229	12.686	-0.171	-8.848	-1.433	1	1.026

Table 5.6: Results from parametric study on chiral node radius r_{chiral} . The results show the twist at the tip of the wing-box for the Abaqus nonlinear simulation ϕ_{tip} and for the linear simulation $\tilde{\phi}_{\text{tip}}$. The maximum relative error of the mean calculation, expressed as percentage, for these two magnitudes is $e(\phi_{\text{tip}})$ and $e(\tilde{\phi}_{\text{tip}})$, respectively. The table also shows the maximum vertical displacement v_{\max} among all the mesh nodes located on the upper skin of the wing-box and the dimensionless position in the spanwise direction $\hat{x}_{v_{\max}}$ and in the chordwise direction $\hat{z}_{v_{\max}}$ of the node that shows $v = v_{\max}$.

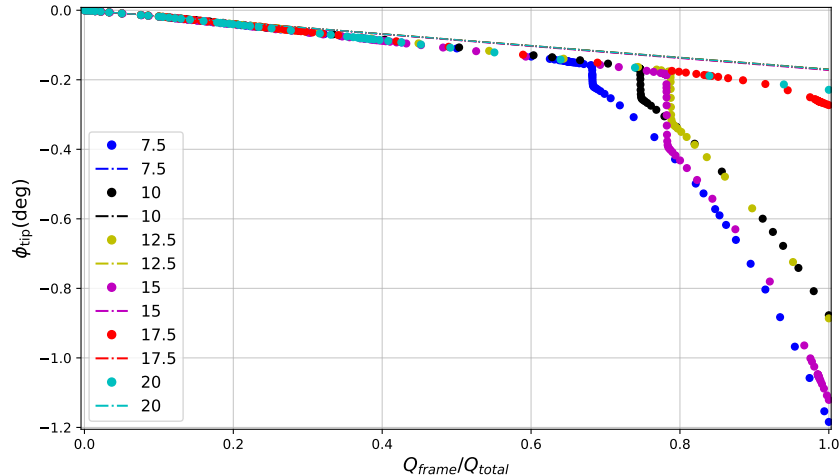


Figure 5.23: Force-displacement curve for various values of the chiral node radius r_{chiral} .

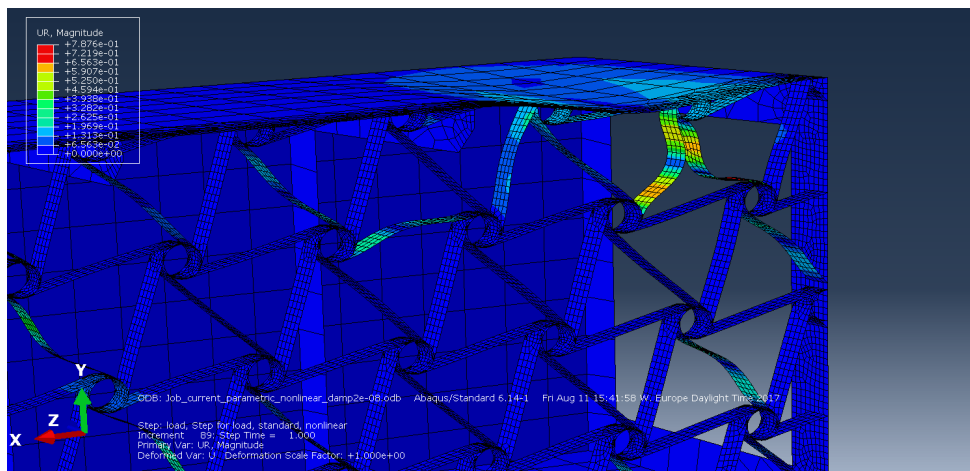


Figure 5.24: Model response when the fraction of load applied equals to 100% of the prescribed load (700 N) and $r_{\text{chiral}} = 12.5$ mm. Results show that buckling occurs here for ligaments located at the root, as shown in for the baseline configuration.

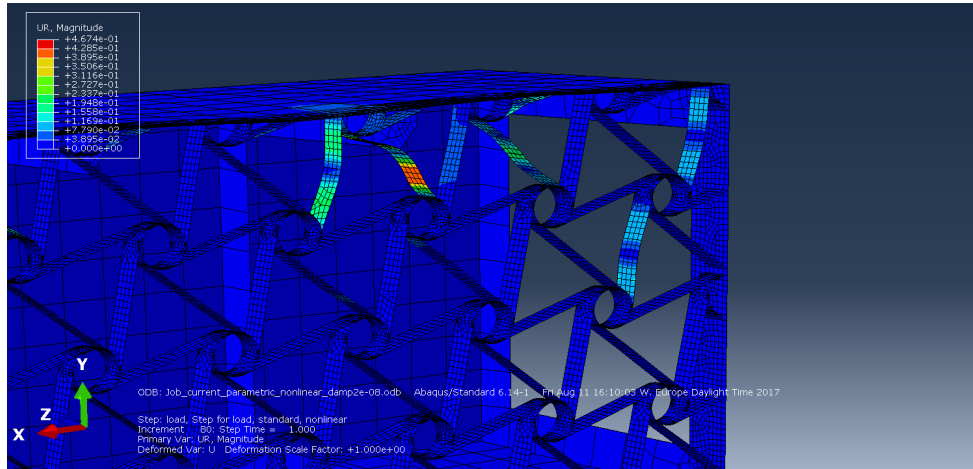


Figure 5.25: Model response when the fraction of load applied equals to 100% of the prescribed load (700 N) and $r_{\text{chiral}} = 17.5$ mm. Here, the excessive value of

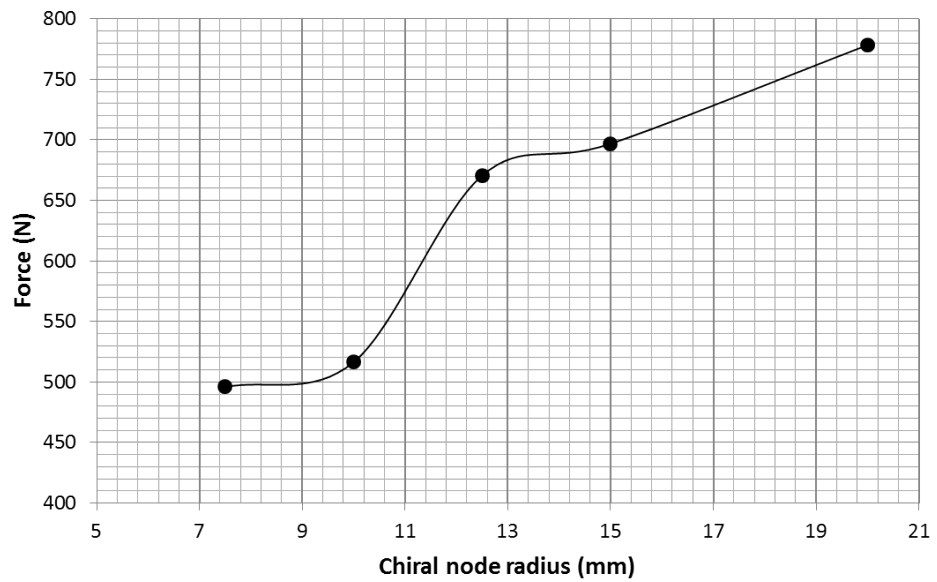


Figure 5.26: Force that induces the structure to collapse as a function of the chiral node radius r_{chiral} .

Chiral ligament half length L_{chiral}

The numeric results obtained for the parametric study on the chiral ligament half length L_{chiral} are shown in Table 5.7. The force-displacement curve for the set of values analyzed is shown in Figure 5.27. This plot shows that the bigger the ligament half length is, the earlier that the structure will collapse after severe buckling of the ligaments at the root. For the case of $L_{\text{chiral}} = 30$, the structure does not collapse as the structure has become very stiff.

Again, in a further step, the force that causes the structure to collapse for a given value of the half length L_{chiral} parameter was investigated. The resulting plot is shown in Figure 5.28.

L_{chiral}	ϕ_{tip} (deg)	$e(\phi_{\text{tip}})$ (%)	$\tilde{\phi}_{\text{tip}}$ (deg)	$e(\tilde{\phi}_{\text{tip}})$ (%)	v_{\max}	$\hat{z}_{v_{\max}}$	$\hat{x}_{v_{\max}}$
30	-0.162	11.739	-0.124	-9.441	-1.032	1	0.602
50	-0.877	9.525	-0.170	-10.196	-9.831	1	0.334
70	-4.374	8.563	-0.205	-9.915	-27.936	1	0.463

Table 5.7: Results from parametric study on chiral ligament half length r_{chiral} . The results show the twist at the tip of the wing-box for the Abaqus nonlinear simulation ϕ_{tip} and for the linear simulation $\tilde{\phi}_{\text{tip}}$. The maximum relative error of the mean calculation, expressed as percentage, for these two magnitudes is $e(\phi_{\text{tip}})$ and $e(\tilde{\phi}_{\text{tip}})$, respectively. The table also shows the maximum vertical displacement v_{\max} among all the mesh nodes located on the upper skin of the wing-box and the dimensionless position in the spanwise direction $\hat{x}_{v_{\max}}$ and in the chordwise direction $\hat{z}_{v_{\max}}$ of the node that shows $v = v_{\max}$.

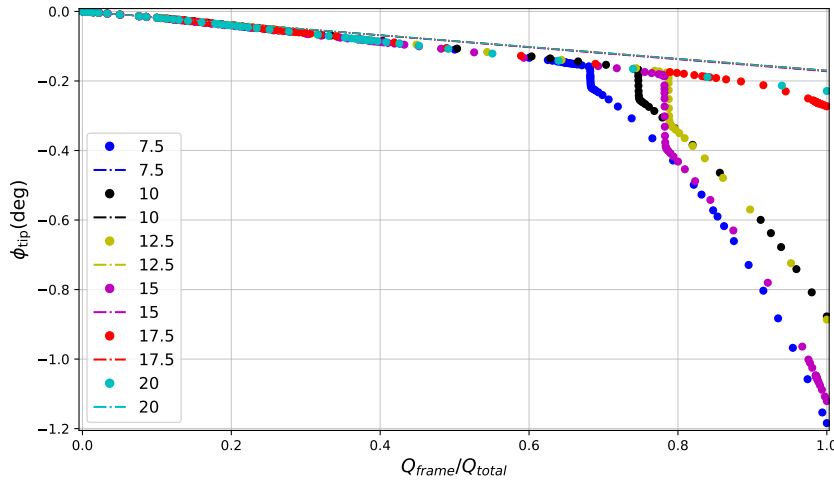


Figure 5.27: Force-displacement curve for various values of the chiral ligament half length L_{chiral} . The bigger the ligament half length is, the earlier that the structure will collapse after severe buckling of the ligaments at the root.

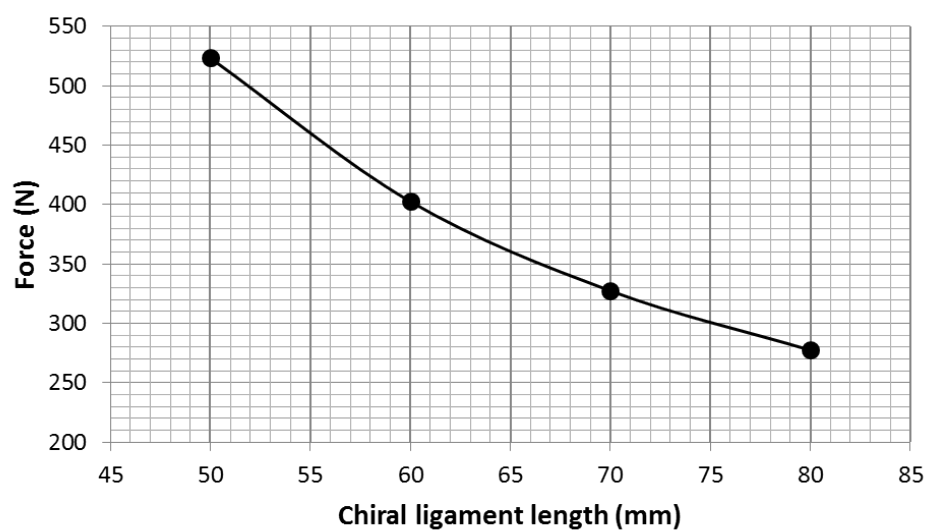


Figure 5.28: Force that induces the structure to collapse as a function of the chiral ligament half length L_{chiral} .

Chiral structure thickness t_{chiral}

The results for the parametric study performed on the chiral structure thickness t_{chiral} are shown in Table 5.8. The force-displacement curve is shown in Figure 5.29. Here it can be seen that a thicker chiral structure delays the structure collapse. Similarly as it occurred for the chiral node depth B_{chiral} , the more bigger the thickness t_{chiral} is, the more abrupt is the decrement in tip twist is.

Finally, the required force to induce the structure to collapse was plot against the corresponding value of the chiral structure thickness t_{chiral} , resulting on the curve shown in Figure 5.30.

t_{chiral}	ϕ_{tip} (deg)	$e(\phi_{\text{tip}})$ (%)	$\tilde{\phi}_{\text{tip}}$ (deg)	$e(\tilde{\phi}_{\text{tip}})$ (%)	v_{\max}	$\hat{z}_{v_{\max}}$	$\hat{x}_{v_{\max}}$
0.2	-1.201	9.464	-0.199	-10.637	-11.878	1	0.334
0.4	-1.026	9.503	-0.179	-10.334	-10.896	1	0.334
0.6	-0.922	13.874	-0.164	-9.816	-10.036	1	0.334
0.8	-0.232	14.445	-0.15	-9.323	-1.449	1	0.971

Table 5.8: Results from parametric study on chiral structure thickness t_{chiral} . The results show the twist at the tip of the wing-box for the Abaqus nonlinear simulation ϕ_{tip} and for the linear simulation $\tilde{\phi}_{\text{tip}}$. The maximum relative error of the mean calculation, expressed as percentage, for these two magnitudes is $e(\phi_{\text{tip}})$ and $e(\tilde{\phi}_{\text{tip}})$, respectively. The table also shows the maximum vertical displacement v_{\max} among all the mesh nodes located on the upper skin of the wing-box and the dimensionless position in the spanwise direction $\hat{x}_{v_{\max}}$ and in the chordwise direction $\hat{z}_{v_{\max}}$ of the node that shows $v = v_{\max}$.

Figure 5.29: Force-displacement curve for various values of the chiral structure thickness t_{chiral} . The bigger the ligament half length is, the earlier that the structure will collapse after severe buckling of the ligaments at the root.

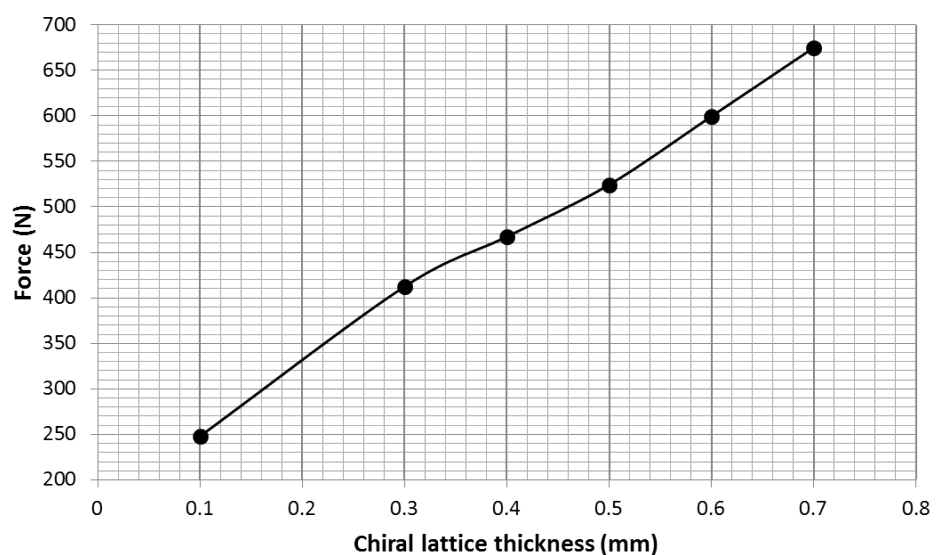


Figure 5.30: Force that induces the structure to collapse as a function of the chiral structure thickness t_{chiral} .

Chapter 6

Conclusion and Outlook

This thesis presents a novel mechanism to achieve wing twist morphing through variations in the wing-box torsional stiffness. The method comprises a wing-box with a variable-stiffness spar which is designed as a lattice of chiral structures formed by interconnected ligaments and nodes. The onset of elastic instabilities in the chiral ligaments provokes that the effective shear modulus for the whole chiral lattice is reduced. This enables the relocation of the wing-box section's shear centre and therefore the variation of the torsional moment acting on the wing-box. In this way, the onset of elastic instabilities in the adaptive spar triggers a twisting morphing deformation in the wing-box.

An analytical model of the wing-box is developed using a ideal beam configuration with variable shear modulus in one of the web. The effect of variations of this magnitude on the torsional stiffness, the flexural stiffness, the shear centre position and the bending and twisting deformations of the wing-box are studied. Also, the effect of variations of the geometry in these magnitudes is analyzed. Results anticipate that, once the buckling-induced reduction in shear modulus in the spar is activated, the reduction in flexural stiffness for the wing-box is negligible compared with the reduction in torsional stiffness.

A computational model of the whole assembly is built next. It is designed in a fully parameterized format using Python scripting. Different design options are considered. Nonlinear simulations are carried out using this model and incorporating artificial dissipation through constant damping factor. Special attention needs to be taken to not originate over-damping of the structure. The onset of the buckling phenomena and its evolution in the chiral lattice is characterized next. Results show that the collapse of the structure occurs when severe buckling appears on the ligaments of the chiral elements located at the root of the wing-box. This event produces a sudden reduction on the torsional stiffness of the structure and an increase in the twist deformation observed at the wing-box tip. A second and more generalized buckling in the chiral lattice is observed to origin a second modification of the torsional stiffness for certain cases. For the baseline configuration of the model, the twist morphing of the wing-box was obtained to be of XX.

Furthermore, a parametric study was performed on the computational model. Results show that considerable tailorability can be achieved through modifications of selected parameters. When considering

Chapter 6. Conclusion and Outlook

the wing-box thickness, it was found that variations of XX mm made that the required force to provoke the onset of the structure collapse was increase in XX N...

COMMENTS ON THE POSSIBLE APPLICATIONS OF THIS TECHNOLOGY

Bibliography

- [1] J.E Cooper, “Introduction to Aircraft Aeroelasticity and Loads,” in *Gust and Turbulence Encounters*, no. 1996, ch. 14, John Wiley & Sons, Ltd., 2007.
- [2] “Part of ”the dream of flight” online exhibit in the American Treasures section at the U.S. Library of Congress..” <http://www.loc.gov/exhibits/treasures/images/>. Accessed: 29 July 2017.
- [3] P. a. Lloyd, “Requirements for smart materials,” *Proceedings of the Institution of Mechanical Engineers, Part G: Journal of Aerospace Engineering*, vol. 221, no. 4, pp. 417–478, 2007.
- [4] S. Boye, “A passenger aircraft with a downwardly foldable wing tip device.” UK Patent: GB2524827. Available at: <https://www.gov.uk/browse/business/intellectual-property/>, 2015. Accessed: 27 July 2017.
- [5] S. Barbarino, O. Bilgen, R. M. Ajaj, M. I. Friswell, and D. J. Inman, “A Review of Morphing Aircraft,” *Journal of Intelligent Material Systems and Structures*, vol. 22, no. 9, pp. 823–877, 2011.
- [6] G. D. Miller, “ACTIVE FLEXIBLE WING (AFW) TECHNOLOGY,” tech. rep., 1988.
- [7] E. Pendleton, P. Flick, D. Paul, D. Voracek, E. Reichenbach, and K. Griffin, “The X-53 A Summary of the Active Aeroelastic Wing Flight Research Program,” *48th AIAA/ASME/ASCE/AHS/ASC Structures, Structural Dynamics, and Materials Conference*, no. April, 2007.
- [8] P. C. Chen, D. Sarhaddi, R. Jha, D. D. Liu, K. Griffin, R. Yurkovich, S. Antonio, R. Yurkovich, and T. B. Company, “Variable Stiffness Spar Approach for Aircraft Maneuver Enhancement Using ASTROS,” *Journal of Aircraft*, vol. 37, no. 5, pp. 865–871, 2000.
- [9] M. Amprikidis and J. E. Cooper, “Development of an Adaptive Stiffness Attachment for an All-Moving Vertical Tail,” *46th AIAA/ASME/ASCE/AHS/ASC Structures, Structural Dynamics and Materials Conference*, no. April, pp. 1–11, 2005.
- [10] B. Stanford, M. Abdulrahim, R. Lind, and P. Ifju, “Investigation of Membrane Actuation for Roll Control of a Micro Air Vehicle,” *Journal of Aircraft*, vol. 44, no. 3, pp. 741–749, 2007.
- [11] B. P. Sanders, C. Martin, and D. Cowan, “Aerodynamic and aeroelastic characteristics of the DARPA Smart Wing phase II wind tunnel model,” *Smart Structures and Materials 2001*, vol. 4332, pp. 390–398, 2001.

- [12] D. M. Elzey, A. Y. N. Sofla, H. N. G. Wadley, A. Y. N. Sofia, and H. N. G. Wadley, “A bio-inspired high-authority actuator for shape morphing structures,” *Proceedings of SPIE*, vol. 5053, no. 7, pp. 1943–1955, 2003.
- [13] A. F. Arrieta, I. K. Kuder, M. Rist, T. Waeber, and P. Ermanni, “Passive load alleviation aerofoil concept with variable stiffness multi-stable composites,” *Composite Structures*, vol. 116, no. 1, pp. 235–242, 2014.
- [14] D. Bornengo, F. Scarpa, and C. Remillat, “Evaluation of hexagonal chiral structure for morphing airfoil concept,” *Proceedings of the Institution of Mechanical Engineers, Part G: Journal of Aerospace Engineering*, vol. 219, no. 3, pp. 185–192, 2005.
- [15] A. Spadoni and M. Ruzzene, “Static Aeroelastic Response of Chiral-core Airfoils,” *Journal of Intelligent Material Systems and Structures*, vol. 18, no. October, pp. 1067–1075, 2007.
- [16] A. Spadoni and M. Ruzzene, “Numerical and experimental analysis of the static compliance of chiral truss-core airfoils,” *Journal of Mechanics of Materials and Structures*, vol. 2, no. 5, pp. 965–981, 2007.
- [17] W. Raither, A. Bergamini, and P. Ermanni, “Profile beams with adaptive bending-twist coupling by adjustable shear centre location,” *Journal of Intelligent Material Systems and Structures*, vol. 24, no. 3, pp. 334–346, 2013.
- [18] A. Bergamini, R. Christen, B. Maag, and M. Motavalli, “A sandwich beam with electrostatically tunable bending stiffness,” *Smart Materials and Structures*, vol. 15, no. 3, pp. 678–686, 2006.
- [19] W. Raither, A. Bergamini, F. Gandhi, and P. Ermanni, “Adaptive bending-twist coupling in laminated composite plates by controllable shear stress transfer,” in *Composites Part A: Applied Science and Manufacturing*, vol. 43, pp. 1709–1716, 2012.
- [20] W. Raither, M. Heymanns, A. Bergamini, and P. Ermanni, “Morphing wing structure with controllable twist based on adaptive bending-twist coupling,” *Smart Materials and Structures*, vol. 22, no. JUNE 2013, p. 065017, 2013.
- [21] F. Runkel, A. Reber, G. Molinari, A. F. Arrieta, and P. Ermanni, “Passive twisting of composite beam structures by elastic instabilities,” *Composite Structures*, vol. 147, pp. 274–285, 2016.
- [22] R. Andreas, *Experimental investigation of the structural response of a wing model with structurally tailored buckling elements for morphing*. Master thesis no. 15-007, ETH Zürich, 2015.
- [23] R. S. Lakes, “Deformation mechanisms in negative Poisson’s ratio materials: structural aspects,” *Journal of Materials Science*, vol. 26, no. 9, pp. 2287–2292, 1991.
- [24] D. Prall and R. Lakes, “Properties of a chiral honeycomb with a poisson’s ratio of 1,” *International Journal of Mechanical Sciences*, vol. 39, no. 3, pp. 305–314, 1997.
- [25] P. Bettini, A. Airolidi, G. Sala, L. D. Landro, M. Ruzzene, and A. Spadoni, “Composite chiral structures for morphing airfoils: Numerical analyses and development of a manufacturing process,” *Composites Part B: Engineering*, vol. 41, no. 2, pp. 133–147, 2010.

- [26] A. Spadoni, M. Ruzzene, and F. L. Scarpa, “Global and local linear buckling behavior of a chiral cellular structure,” *Physica Status Solidi (B)*, vol. 242, no. 3, pp. 695–709, 2005.
- [27] J. Zhang and M. F. Ashby, “Buckling of honeycombs under in-plane biaxial stresses,” *International Journal of Mechanical Sciences*, vol. 34, no. 6, pp. 491–509, 1992.
- [28] L. J. Gibson and M. F. Ashby, *Cellular Solids: Structure and Properties*, vol. 7. 1999.
- [29] F. Scarpa, S. Blain, T. Lew, D. Perrott, M. Ruzzene, and J. R. Yates, “Elastic buckling of hexagonal chiral cell honeycombs,” *Composites Part A: Applied Science and Manufacturing*, vol. 38, no. 2, pp. 280–289, 2007.
- [30] W. Miller, C. W. Smith, F. Scarpa, and K. E. Evans, “Flatwise buckling optimization of hexachiral and tetrachiral honeycombs,” *Composites Science and Technology*, vol. 70, no. 7, pp. 1049–1056, 2010.
- [31] B. Haghpanah, J. Papadopoulos, D. Mousanezhad, H. Nayeb-Hashemi, and A. Vaziri, “Buckling of Regular, Chiral and Hierarchical Honeycombs under a General Macroscopic Stress State,” *Proceedings of the Royal Society A: Mathematical, Physical and Engineering Sciences*, vol. 470, no. 2167, p. 20130856, 2014.
- [32] G. Ramstein, *Experimental Validation of Chiral Structures with Local Controlled Instabilities*. Semester project no. 16-015, ETH Zürich, 2016.
- [33] A. Spadoni, M. Ruzzene, and F. Scarpa, “Dynamic Response of Chiral Truss-core Assemblies,” *Journal of Intelligent Material Systems and Structures*, vol. 17, no. November, pp. 941–952, 2006.
- [34] A. Airolidi, M. Crespi, G. Quaranti, and G. Sala, “Design of a Morphing Airfoil with Composite Chiral Structure,” *Journal of Aircraft*, vol. 49, no. 4, pp. 1008–1019, 2012.
- [35] A. Airolidi, P. Bettini, P. Panichelli, M. F. Oktem, and G. Sala, “Chiral topologies for composite morphing structures - Part I: Development of a chiral rib for deformable airfoils,” *Physica Status Solidi (B) Basic Research*, vol. 252, no. 7, pp. 1435–1445, 2015.
- [36] N. Hu and R. Burgueño, “Buckling-induced smart applications: recent advances and trends,” *Smart Materials and Structures*, vol. 24, no. 6, p. 063001, 2015.
- [37] P. M. Reis, “A perspective on the revival of structural (in) stability with novel opportunities for function: From buckliphobia to buckliphilia,” *Journal of Applied Mechanics*, vol. 82, no. 11, p. 111001, 2015.
- [38] R. Vincenz, *Airfoil camber morphing exploiting chiral structures: Manufacturing and testing*. Semester project no. 17-041, ETH Zürich, 2017.
- [39] Dassault Systèmes, *Abaqus 6.14 Online Documentation*, 2014.

Appendix A

Python code generated

All the code generated for this project can be downloaded from the following Github repository:
<https://github.com/AlejandroValverde/abaqus.git>.